VORTEX RING PROPAGATION IN CONFINED SPHEROIDAL DOMAINS AND APPLICATIONS TO CARDIAC FLOWS

By

MILAD SAMAEE

Bachelor of Science in Mechanical Engineering
Khaje Nasir Toosi University of Technology
Tehran, Iran
2008

Master of Science in Biomedical Engineering
Amirkabir University of Technology
Tehran, Iran
2011

Submitted to the Faculty of the
Graduate College of the
Oklahoma State University
in partial fulfillment of
the requirements for
the Degree of

DOCTOR OF PHILOSOPHY
December, 2019

VORTEX RING PROPAGATION IN CONFINED SPHEROIDAL DOMAINS AND APPLICATIONS TO CARDIAC FLOWS

Dissertation Approved:

Dr. Arvind Santhanakrishnan

Dissertation Adviser

Dr. Jamey Jacob

Dr. Khaled Sallam

Dr. Sundar Madihally

Dr. Yu Feng

Name: MILAD SAMAEE

Date of Degree: DECEMBER, 2019

Title of Study: VORTEX RING PROPAGATION IN CONFINED SPHEROIDAL DOMAINS AND APPLICATIONS TO CARDIAC FLOWS

Major Field: MECHANICAL ENGINEERING

Abstract: Vortex ring formation is observed in the human cardiac left ventricle (LV) during diastole. Numerous studies to date have examined the intraventricular filling vortex for potential use in the diagnosis of cardiac dysfunction. However, a systematic understanding of the effects of LV size on vortex ring properties is currently unavailable. In diastolic dysfunction (LVDD), heart muscles can thicken and decrease the internal volume of the LV. On the other hand, by progressing diastolic dysfunction, the transmitral inflow changes and the impact of inflow altering on vortex ring properties is also unknown. In contrast to the considerable body of research on vortex ring propagation in semi-infinite domains and interaction with walls, only a limited number of studies have examined confined vortex ring dynamics. The latter studies only considered radially confined domains, which are a simplification to the combined radial and axial confinement observed in spheroidal domains such as the LV. We experimentally examined vortex ring propagation within three flexible-walled, semi-spheroidal physical models (semi-oblate, hemisphere, and semi-prolate) that presented both axial and radial confinement. 2D time-resolved particle image velocimetry (TR-PIV) measurements showed that while the formation process and peak circulation were nearly unaffected with changing geometry, increasing axial confinement increased the rate of normalized circulation decay. We next examined vortex propagation in an *in-vitro* model of the LV, under physiological hemodynamic. Two flexible-walled, anatomical physical models representative of a normal LV and an LV with asymmetric wall thickening characteristic of hypertrophic cardiomyopathy (HCM) were examined. We varied the end-diastolic volume (EDV) of the models to change the confinement level. Peak circulation was lowered in the HCM model and also in the normal LV model with lower EDV when compared to the normal LV model with normal EDV. In the end, we examined the role of transmitral inflow on vortex ring properties under different grades of diastolic dysfunction. The normal transmitral flow showed higher circulation strength, momentum flux, and stronger vortex ring compared to those of diastolic dysfunction. Our results suggest that peak circulation and normalized circulation decay rates have the potential link with LVDD from the fluid mechanics' point of view.

TABLE OF CONTENTS

LIST OF TABLES

Table Page

LIST OF FIGURES

Figure Page

Figure Page

Figure Page

CHAPTER I

1. INTRODUCTION

1.1. Motivation

These pages are where you type in the title of your chapter and add the body (text, images, etc.)

Heart failure (HF) causes one in nine mortality in the United States (1). The inability of the heart to deliver sufficient blood to the other organs is called heart failure. A cardiac cycle contains two stages of filling (diastole) and ejection (systole). This study is mainly focused on the diastole part in which blood flow enters into the left ventricle (LV). Most of the time, heart failure is associated with both systole and diastole malfunction; however, in one-third of heart failure patients the function of systole is preserved, and diastole dysfunction causes heart failure, which is called heart failure with diastolic dysfunction (DD) (2). Having a better understanding of fluid flow properties in the LV can help physicians to recognize and predict heart disease and dysfunction earlier, and consequently can help them to improve heart failure diagnosis. Previous in-vivo and in-vitro research on heart failure have enhanced the understanding of intraventricular filling effects in hemodynamic parameters (3-6), but they are still uncertain. The effects of LV compliance, shape, and volume of LV on intraventricular filling has not been investigated in detail. Therefore, diagnosis and treatments of patients with heart failure are very challenging due to the extremely complex physiology of the heart; moreover, the heart is the most vital organ in the human body. As a result, a better understanding of heart failure symptoms through non-

invasive ways from the fluid mechanics' point of view will assist physicians for heart disease diagnosis in the early stages. Several clinical studies have observed a vortex in LV filling (diastole phase) and many studies have shown that it can be useful for diagnosing diseases such as dilated cardiomyopathy (7, 8), and hypertrophic (9). Previous studies showed that vortex rings are different in diseased hearts compare to a healthy heart. We need to understand how the vortex ring changes in different types of diseases, which is still overlooked. Therefore, having a systematic study from mechanics' point of view to understand how this vortex effects and changes in properties under specific conditions in heart failure (i.e., hypertrophic cardiomyopathy or HCM, in which the LV cavity size become smaller) is essential.

From the fluid mechanics' standpoint, vortex rings have been studied in semi-infinite domains (10), confined domains (11, 12), and also vortex ring interaction with rigid walls (13-15). Vortex ring studies have been applied for cardiac problems in diseased hearts. However, there is no fundamental study of vortex ring interaction in a confined domain such as the left ventricle. Gharib et al. (16) introduced a universal time scale (formation number) for unconfined vortex formation, which is defined as L/D, where L and D are the piston stroke and diameter, respectively. They showed the vortex ring peak circulation (and correspondingly the vortex pinch-off) occurs at the time of formation number and the circulation cannot grow after the formation number, which is valuable information. Stewarts et al. (12) investigated vortex ring decay in rigid cylindrical domains under different confinement ratio and also different Reynolds numbers (11). To the best of our knowledge, there is no fundamental study on vortex ring interaction with spherical domains, which can be very helpful to understand the behavior of vortex ring interaction with the left ventricle. As a result, it is essential to investigate the mechanism of vortex ring decay in an idealized spherical model before studying intraventricular flow in the left ventricle, which has more complex geometries.

In this study, we developed a piston-cylinder arrangement to generate vortex rings. We first validated our setup with published studies (11, 12) for both semi-infinite and radially confined domains. After that, we examined the formed vortex rings inside an idealized silicone model of semi-ellipsoidal shape with three different aspect ratios and compared the decay and properties of vortex rings among the different lengths of confinements. In the end, we studied intraventricular filling properties and compared the vortex ring decays and formations in the LV under different conditions of HFNEF conditions by changing LV cavity size, stiffening the LV walls, and thickening the left ventricular myocardium (HCM).

1.2. Aims of the study

The objective of this study is examining the properties of vortex rings in interaction with flexible spheroidal walls under different experimental conditions, i.e., changing the geometry of the confined domain, changing the filling jet properties such as filling time, Reynolds number, and the ratio of acceleration/deceleration time (AT/DT). Following the vortex ring behavior within a flexible confined domain, we also investigated possible applications in the cardiovascular system by maintaining physiological hemodynamic parameters and applying different left ventricular diseases. All experiments in this study were in vivo analysis of vortex rings. Each aim in this study is written as a separate chapter, which is presented in a research article format and may have an overlap in methodology.

1.2.1. **Aim I: Vortex ring propagation in flexible-walled semi-spheroidal domains**

We hypothesized that vortex rings decay faster in higehr axial confined domains. This hypothesis was tested by utilizing a cylinder-piston arrangement and three different levels of confinement on flexible-walled silicone models. To validate our methodology, we compared the circulation of vortex rings within semi-infinite and rigid tubes with Stewart et al. (12). We experimentally investigated laminar vortex ring propagation in confined domains under a passive expansion of

flexible walls. PIV measurements were conducted on flexible-walled silicone models of three geometries imposing radial and axial confinement: hemisphere, semi-prolate spheroid, semi-oblate spheroid. Although the vortex formation process was nearly unaffected for a particular geometry, we observed a higher rate of decay of circulation with increasing confinement. The effects of varying filling duration, Reynolds number, and deceleration time on the decay of circulation are discussed. After investigated laminar vortex ring properties within a confined domain under passive wall motion, it is valuable to examine a similar study of vortex generation within a flexible-walled spheroidal domain under active wall movement instead of passive wall movement. The relevance of this part of the work is the majority of blood flow enters the left ventricle under active wall motion rather than passive wall movement. Three different AT/DT ratios, and also four different Reynolds numbers were considered to study the vortex ring properties within a flexible walled semi-prolate model. Results did not show a noticeable difference between active and passive filling.

1.2.2. Aim II: Effects of varying LV confinement severity on the intraventricular filling vortex

We concluded from Aim I that increasing the severity of confinement impairs the vortex ring functionality and results in faster circulation decay. Similarly, we set up an in-vitro study to examine the effects of LV size on vortex ring properties since the left ventricle size can be decreased under diastolic dysfunction because of heart muscle thickening. Aim I showed the difference between active and passive filling was not noticeable; however, for conducting a more systematic study, we designed a left heart simulator in which the left ventricle was filling under active flexible-walled motion. We tuned our experimental setup to achieve physiological hemodynamics for the normal LV model. We used two different geometries (normal LV and HCM geometry), and we examined intraventricular filling flow patterns. All experimental circuit variables were maintained unchanged, while we only varied the LV geometry or LV end-diastolic

volume (EDV) size. We compared diastolic filling flow characteristics between normal LV and HCM models under different EDVs. Results show that circulation peak values diminished in the HCM model and also normal LV model with lowering EDV compare to normal LV with normal EDV. The outcome of this study can be useful to assess the vortex ring properties in a specific LV geometry by evaluating the size and shape of the LV without doing echocardiograms.

1.2.3. Aim III: Effects of varying transmitral inflow profile on filling vortex properties

The results from Aim I showed us that changing AT/DT and also Reynolds number impacted the vortex dynamics in semi-spheroidal confined domains. Based on the conclusion in Aim I, we selected different types of transmitral flow in diastolic dysfunction from published clinical data, and we mainly focused on changing AT/DT ratios. We examined vortex ring dynamics in an anatomical LV by visualizing the central plane of the LV using 2D-TR-PIV. We used the same LV physical model throughout the test conditions, and we just changed the piston waveform to generate desirable flows based on different grades/stages of diastolic dysfunction. Intraventricular flows for all different transmitral flow conditions are characterized. The goal of this aim is whether we can use the vortex circulation strength as a metric to evaluate the functionality of the LV during the filling time. Also, this aim will help us to understand the fluid mechanics of the vortex ring inside the LV in the process of diastolic dysfunction.

1.3. References

1. Mozaffarian, D., Benjamin, E. J., Go, A. S., Arnett, D. K., Blaha, M. J., Cushman, M., ... & Howard, V. J. (2016). Executive summary: heart disease and stroke statistics—2016 update: a report from the American Heart Association. *Circulation*, *133*(4), 447-454.

2. Khouri, S. J., Maly, G. T., Suh, D. D., & Walsh, T. E. (2004). A practical approach to the echocardiographic evaluation of diastolic function. *Journal of the American Society of Echocardiography*, *17*(3), 290-297.

3. Kilner, P. J., Yang, G. Z., Wilkes, A. J., Mohiaddin, R. H., Firmin, D. N., & Yacoub, M. H. (2000). Asymmetric redirection of flow through the heart. *Nature*, *404*(6779), 759.

4. Kim, W. Y., Bisgaard, T., Nielsen, S. L., Poulsen, J. K., Pedersen, E. M., Hasenkam, J. M., & Yoganathan, A. P. (1994). Two-dimensional mitral flow velocity profiles in pig models using epicardial Doppler echocardiography. *Journal of the American College of Cardiology*, *24*(2), 532-545.

5. Kim, W. Y., Walker, P. G., Pedersen, E. M., Poulsen, J. K., Oyre, S., Houlind, K., & Yoganathan, A. P. (1995). Left ventricular blood flow patterns in normal subjects: a quantitative analysis by three-dimensional magnetic resonance velocity mapping. *Journal of the American College of Cardiology*, *26*(1), 224-238.

6. Pedrizzetti, G., Domenichini, F., & Tonti, G. (2010). On the left ventricular vortex reversal after mitral valve replacement. *Annals of biomedical engineering*, *38*(3), 769-773.

7. Gharib, M., Rambod, E., Kheradvar, A., Sahn, D. J., & Dabiri, J. O. (2006). Optimal vortex formation as an index of cardiac health. *Proceedings of the National Academy of Sciences*, *103*(16), 6305-6308.

8. Kheradvar, A., Milano, M., & Gharib, M. (2007). Correlation between vortex ring formation and mitral annulus dynamics during ventricular rapid filling. *Asaio Journal*, *53*(1), 8-16.

9. Prinz, C., Lehmann, R., Brandao da Silva, D., Jurczak, B., Bitter, T., Faber, L., & Horstkotte, D. (2014). Echocardiographic particle image velocimetry for the evaluation of diastolic function in hypertrophic nonobstructive cardiomyopathy. *Echocardiography*, *31*(7), 886-894.

10. Dabiri, J. O., Colin, S. P., Costello, J. H., & Gharib, M. (2005). Flow patterns generated by oblate medusan jellyfish: field measurements and laboratory analyses. *Journal of Experimental Biology*, *208*(7), 1257-1265.

11. Stewart, K. C., Niebel, C. L., Jung, S., & Vlachos, P. P. (2012). The decay of confined vortex rings. *Experiments in Fluids*, *53*(1), 163-171.

12. Stewart, K. C., & Vlachos, P. P. (2012). Vortex rings in radially confined domains. *Experiments in fluids*, *53*(4), 1033-1044.

13. Chang, T. Y., Hertzberg, J. R., & Kerr, R. M. (1997). Three-dimensional vortex/wall interaction: Entrainment in numerical simulation and experiment. *Physics of Fluids*, *9*(1), 57-66.

14. Lim, T. T. (1989). An experimental study of a vortex ring interacting with an inclined wall. *Experiments in Fluids*, *7*(7), 453-463.

15. Walker, J. D. A., Smith, C. R., Cerra, A. W., & Doligalski, T. L. (1987). The impact of a vortex ring on a wall. *Journal of Fluid Mechanics*, *181*, 99-140.

16. Gharib, M., Rambod, E., & Shariff, K. (1998). A universal time scale for vortex ring formation. *Journal of Fluid Mechanics*, *360*, 121-140.

CHAPTER II

2. BACKGROUND

An intraventricular flow pattern can be used as an indication of a possible malfunction in the cardiac system. A noticeable feature of cardiac blood flow is the existence of vortex rings, which can be useful in the evaluation of cardiac health (1-5). As a result, understanding the fluid mechanics of the vortex ring is essential primarily when it interacts with solid boundaries, such as left ventricle myocardium. To investigate the relation between heart diseases and the associated fluid mechanics of the cardiac system, having a basic knowledge of the physiology and anatomy of the cardiac system and also cardiac disorders is necessary.

2.1. Cardiac Anatomy and Physiology

The human heart is a conical shape rests in between the lungs and consists of four chambers: two collecting chambers (left and right atrium) and two pumping chambers (left and right ventricle), which is shown in **Figure 2-1**a. A muscle wall, which is called septum, separates the left ventricle and atrium from the right ventricle and atrium. The heart wall tissue consists of three layers: 1) the outer layer, which is made from connective tissues and is called epicardium, 2) heart muscles or myocardium, and 3) endocardium, which is the inner layer, and it is in contact with blood inside the chambers and protects heart valves.

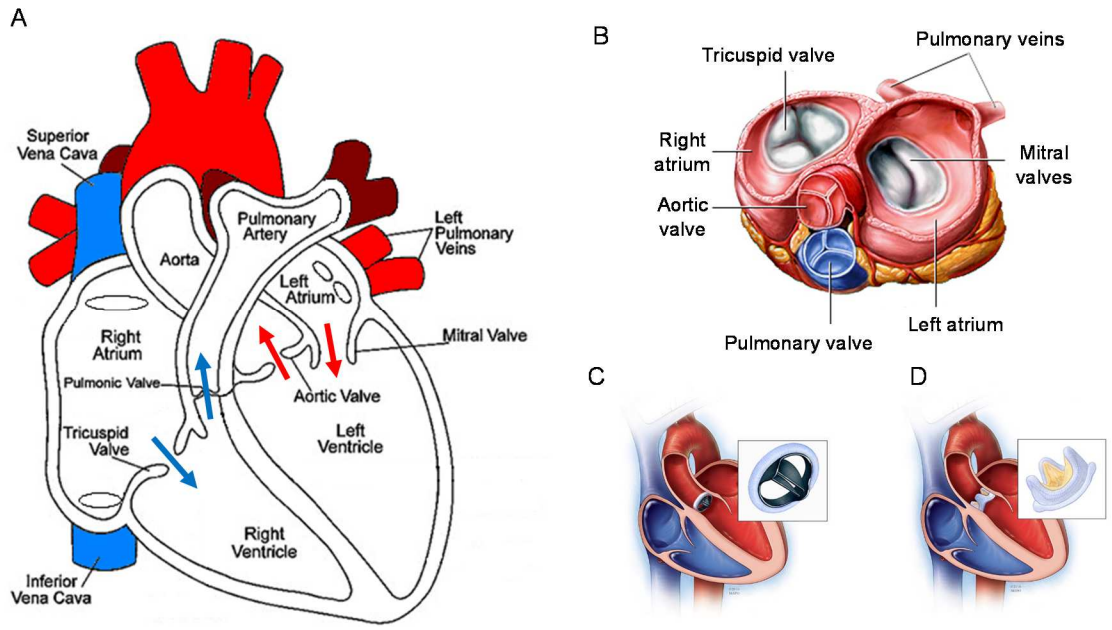

Figure 2-1. Human heart anatomy. A) frontal section view of the human heart (retrieved from www.cardiaccathpro.com). The direction of blood flow is shown in the image; B) superior view of heart valves. The mitral valve has two leaflets, unlike the three other valves (pulmonary, aortic, and tricuspid valves have three leaflets). replacement mitral valve with a biological valve; and C) mitral valve replacement with a mechanical heart valve, and D) (top) mitral valve replacement with a biological heart valve (retrieved from www.mayoclinic.org)

Each ventricle has two valves to assure a unidirectional flow through the cardiac system and prevent backflow. **Figure 2-1**A shows the superior view of all four valves of the human heart. Heart valves can be faced with problems mainly because of congenital abnormalities or infection, and if it is not repairable, it has to be replaced. There are two types of heart valves: mechanical heart valves and biological heart valves (which are usually removed from pig hearts).

Figure 2-1C and **Figure 2-1**D show the replacement of the mitral valve with mechanical and biological heart valves, respectively. In a few words, deoxygenated blood enters the right side of the heart (right ventricle and atrium) and goes to the lungs. And then the left side of the heart (left ventricle and atrium) receives the oxygenated blood from the lungs and sends it to the body (**Figure 2-2**A).

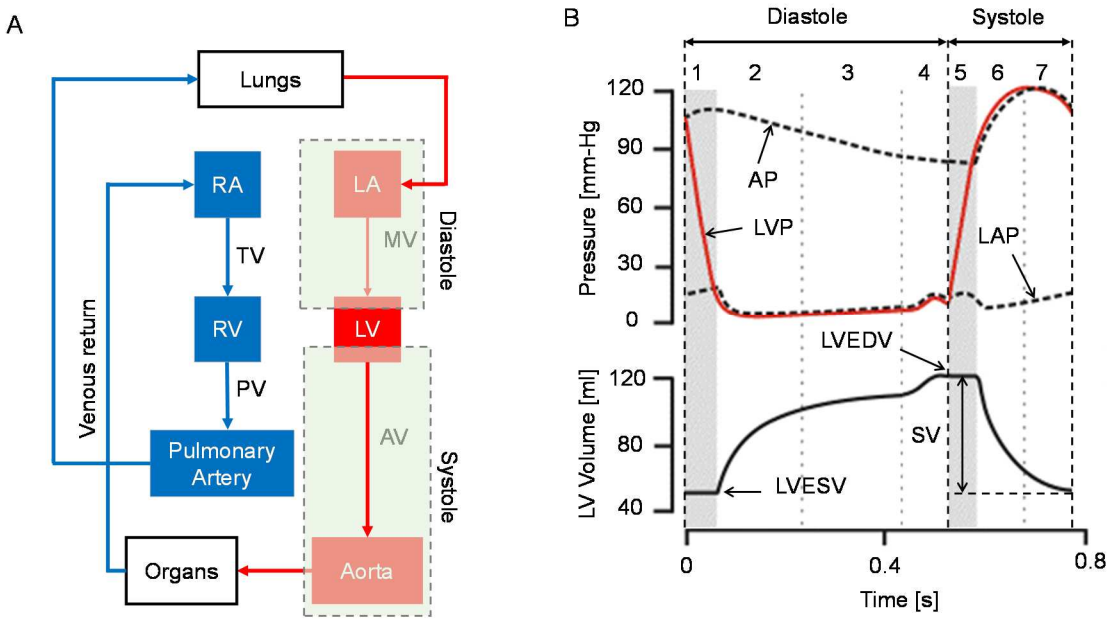

Figure 2-2. Human heart physiology: A) cardiac cycle. The shaded areas demonstrate diastole and systole (LA = left atrium, MV = mitral valve, LV = left ventricle, AV = aortic valve, RA = right atrium, TV = tricuspid valve, RV = right ventricle, and PV = pulmonic valve). B) Wiggers diagram: cardiac physiology (AP = aortic pressure, LVP = left ventricular pressure, LAP = left atrium pressure, LVEDV = left ventricular end-diastolic volume, LVESV = left ventricular end-systolic volume, and SV = stroke volume).

In one cardiac cycle, the left ventricle (LV) experiences two phases: a) diastole or filling phase in which the oxygenated blood injects from left atria to the left ventricle through mitral valve; and b) systole or ejection phase in which the oxygenated blood ejects the left ventricle to the aorta through the aortic valve (the shaded regions in **Figure 2-2**A).

The filling phase (diastole) consists of four sub-phases, as numbered in **Figure 2-2**B: 1) isovolumetric ventricular relaxation phase, in which all four valves are closed. The pressure inside the left ventricle (LV) will drop while the volume of the LV remains unchanged. The amount blood volume in the LV at this step is called end-systolic volume (ESV), and it is the minimum volume of the LV, which is typically ~50 ml in healthy adult hearts; 2) rapid filling or early diastole filling (E-wave), which is the most crucial part of filling. The blood flow pumps from the left atria to the LV in this step. The majority portion of total incoming blood into the LV

is injected in this stage. The ventricles are still under relaxation, and consequently, the intraventricular pressure still drops briefly; 3) diastasis, which mitral valve remains open, and the blood continues flowing into the LV with the nearly constant flow rate. By the end of this phase, the LV fills almost 90%. The intraventricular pressure tends to rise slightly, and the aortic pressure continues to fall during this phase; 4) and the last stage in diastole is an atrial contraction, which LAP increases and causes left atria contraction, which leads to rapid blood flow injection into the LV and generates the second flow wave (A-wave). About 10% of LV occurs at this phase for a resting heart at normal heart rate. This portion may increase up to 40% at high heart rates. The LV volume reaches the highest value and is called end-diastolic volume (EDV), which typically is ~120 ml in healthy adult hearts. The difference between EDV and ESV is called stroke volume (SV) and usually is ~70 ml in healthy adult hearts. The total amount of pumped blood by heart in one minute is called cardiac output (CO) and can be defined as the multiplication of heart rate (HR) by SV (CO = HR×SV). A normal HR at rest is ~70 bpm. Therefore an ordinary CO is ~5 L/min (6).

The ejection phase or systole consists of three sub-phases as numbered in **Figure 2-2**b: 5) isovolumetric contraction in which myocardium contracts while all four valves are closed. Therefore, the LV volume remains unchanged, and the intraventricular pressure increases rapidly (since all valves are closed) until it reaches atrial pressure, which is typically ~80 mm-Hg. The rate of pressure increase (dp/dt) in this phase is a crucial factor in determining the strength of muscle fiber contractions. 6) rapid ejection in which the aortic valve opens and lets the blood flow ejects rapidly into the aorta from LV, and the aortic pressure reaches ~120 mm-Hg. Therefore, the normal aortic pressure in systole is 80/120 mm-Hg, which doctors refer to and known as "blood pressure." 7), and the last phase of systole that ends one cardiac cycle is reduced ejection. In this phase, the aortic pressure and intraventricular pressure fall, and consequently, the rate of ejection decreases, and the LV cavity reaches the minimum volume (ESV).

This study is focused on the filling phase (diastole phase) of the LV. The amount of ejected blood from the left ventricle, which is called (SV), divided by the maximum volume of the left ventricle, which is called end-diastolic volume (EDV) during each cardiac cycle, defines as ejection fraction. Ejection fraction is a standard clinical metric for measuring heart pumping efficiency and can determine cardiac health. The healthy percentage of left ventricle EF is higher than 55% (7); however, in patients with heart failure with normal ejection fraction (HFNEF), the percentage of EF is higher than 50%, which makes the disease diagnose difficult for physicians. HFNEF is mostly associated with heart failure with diastolic dysfunction. The following elaborates common heart diseases related to the diastole phase of the LV.

2.2. Left ventricular disease

Heart failure with normal ejection fraction (HFNEF) is a clinical syndrome that occurs in 50% of HF patients (8-10). Several studies show that patients with diastolic dysfunction and/or hypertrophy, have normal EF (11). However, recent studies claim that systolic function is not entirely normal in patients with HFNEF (12). In many heart failures, the diastole part (LV filling dynamics) impairs (13, 14)and known as cardiac symptoms despite normal systole cardiac function (15-17). Moreover, the functionality of systolic ventricular can be impaired due to diastolic dysfunction (17). HFNEF is characterized by clinical symptoms of heart failure, such as dyspnea, fluid retention, and fatigue. Multiple factors contribute to HFNEF, including diastolic dysfunction (DDF), left ventricular systolic dysfunction (10, 18), systemic hypertension, vascular stiffening, left atrial (LA) size and dysfunction, right ventricular dysfunction, pulmonary hypertension, aging, diabetes, obesity, and chronic kidney disease (1, 2). The common causes of left ventricular dysfunction are explained as follow.

2.2.1. **Left ventricular diastolic dysfunction (LVDD)**

In patients with diastolic heart failure and left ventricular diastolic dysfunction (LVDD), the dynamics of LV filling is mainly malfunctioned, which is affected by 27% of the population (21). There is a significant clinical need to develop improved diagnostic measures and treatments to reduce mortality rates (22) among the growing number of HFNEF patients. The heterogeneous pathophysiology of HFNEF challenges both the diagnosis and treatment of the syndrome (23, 24) because diastolic dysfunction (DD) can be caused by a few coexistent causes such as impaired LV wall compliance or relaxation and also hypertension.

2.2.2. **cardiomyopathy**

The disease of heart muscles is known as cardiomyopathy in which the heart loses its efficiency to pump the blood flow. In cardiomyopathy, the heart muscles become more rigid, thick, or enlarged. Abnormal thickening of left ventricle muscles is called hypertrophic cardiomyopathy (HCM) and causes shrinking the left ventricle cavity size (**Figure 2-3**b). Dilated cardiomyopathy is another type of cardiomyopathy, in which the left ventricular chamber becomes enlarged and becomes unable to pump sufficient blood (**Figure 2-3**c). In another type of cardiomyopathy, the left ventricle muscles become stiffer, and the heart reduces the pumping efficiency, which is classified as hypertrophic cardiomyopathy.

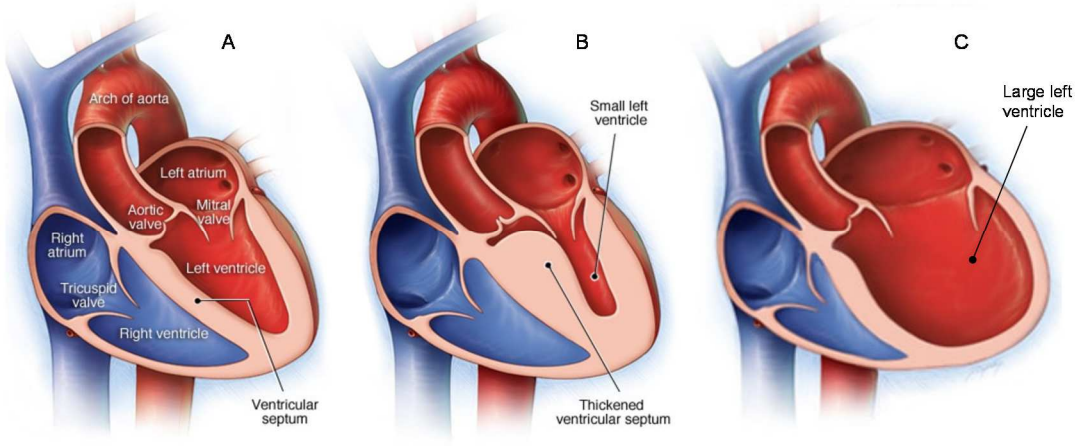

Figure 2-3. Types of cardiomyopathy. A) normal left ventricle: all four chambers are visible in this figure B) Hypertrophic cardiomyopathy (HCM): small left ventricular cavity and thick heart muscle are noticeable in the figure, and C) Dilated cardiomyopathy: large left ventricle cavity size and consequently lower pumping efficiency (retrieved from www.mayoclinic.org)

The following explains all types of cardiomyopathy in detail.

2.2.2.1. Hypertrophic cardiomyopathy (HCM)

Hypertrophy of left ventricle (LV) is called Hypertrophic cardiomyopathy or HCM, and it occurs in 0.2% of the general population (25-27). This disease is caused by gene mutations or family history and results in LV hypertrophy, which has an asymmetrical pattern most of the time. Aging changes the hypertrophy severity of left ventricular; however, the presence of HCM may identify even in very young children and is not documented in their medical history (28). On the other hand, the increase in LV wall thickness frequently happens throughout the teenage years and increases rapidly until their 20s. As a result, it is essential to evaluate the LV functionality by a non-invasive approach. From the fluid mechanics' viewpoint, the intraventricular flow properties can be examined by different modalities such as MRI and echocardiogram. Therefore, using the blood flow data along with a clinical metric to assess the LV functionality will be very valuable.

The intraventricular pressure drops rapidly at the start of diastole to let the blood flow injected into the LV; however, in HFNEF patients diastolic filling impairs. One of the probable causes is

LV wall stiffening, which is reported by a few studies under invasive measurements (29-31). Even though the EF preserved in HFNEF patients, the cardiac output reduces, especially under exercise conditions. Left ventricular stiffening is classified as hypertrophic cardiomyopathy, and it is not a type of cardiomyopathy on its own (32).

2.2.2.2. Dilated cardiomyopathy (DCM)

A common cause of heart failure and sudden cardiac death is left ventricular dilation, which is called Dilated cardiomyopathy (DCM). In this disease, the LV wall muscles stretch and become enlarged (EDV in this type of disease can reach as high as 250 ml) and weaker (26, 33, 34). As a result, the heart muscles lose the ability to pump blood flow like a healthy heart, and DCM is linked with systolic dysfunction. The ejection fraction drops significantly (EF as low as 20%) in DCM patients (35, 36). This disease is commonly initiated from the LV and may affect other chambers over time (33).

2.3. Transmitral inflow in different grades of diastolic dysfunction

A traditional approach to assess LV diastolic dysfunction is the evaluation of mitral inflow using echocardiogram. The pressure gradient between the left ventricle and left atrium causes transmitral velocity, which we can monitor by spectral Doppler. Characterizing the transmitral inflow patterns can deliver the diastolic functionality of the left ventricle. A normal pattern of transmitral flow is shown in **Figure 2-4**.

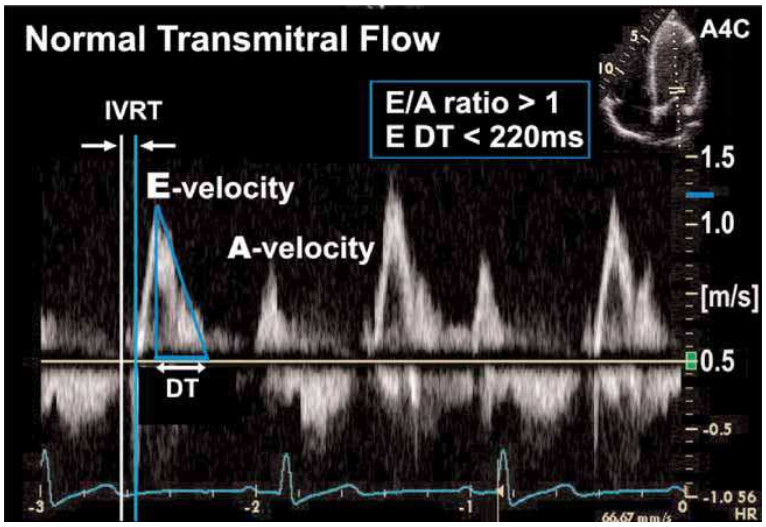

Figure 2-4. Normal transmitral Doppler flow (DT = deceleration time) (37).

In the normal transmitral flow, the E/A ratio is higher than one (E/A ~1-1.5), and the early filling deceleration is in the range of 150-220 ms. The A-wave duration does not exceed 20% typically, and the E-Wave peak velocity is ~ 0.65-0.8 m/s (16, 38-41). Any changes in the parameters above (E/A ratio, E-wave deceleration time, and E-wave peak velocity) can be classified as diastolic dysfunction. The transmitral pressure gradient between the left ventricle and left atrium (LA) accelerates inflow into the LV through the mitral valve. As a result, increasing the LA pressure increases the peak E-wave. E-wave deceleration time is inversely related compliance of LV. Therefore, during the aging process the LV becomes stiffer (less compliance), and consequently deceleration time becomes higher. There is also a limitation in using mitral inflow patterns to assess diastolic dysfunction because the LA pressure decrease can be linked with both deceleration time and peak value of E-Wave decrease (37).

2.3.1. **Grade I: Delayed relaxation**

Prolonged E-wave deceleration time (DT > 200 ms), and also E/A ratio less than 1 are two noticeable characteristics in the Doppler pattern of diastolic dysfunction with impaired relaxation as shown in **Figure 2-5**.

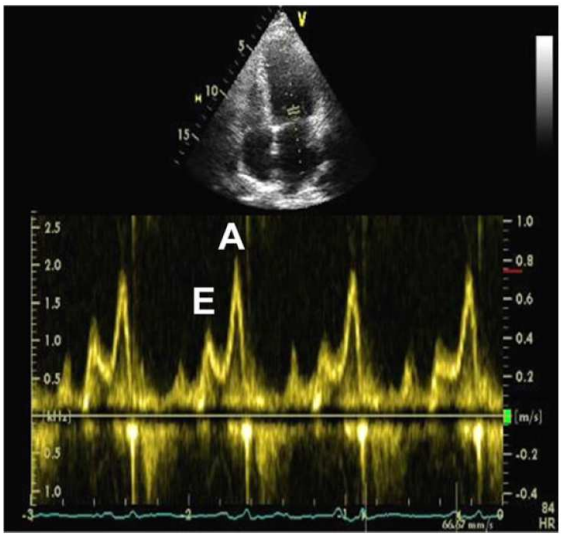

Figure 2-5. 2-D Doppler Echocardiogram of a patient with impaired relaxation pattern (16)

This pattern is typical in older people (more than 60 years), in which the LV becomes stiffer, or the LV relaxation becomes impaired, and eventually, it cannot supply enough pressure gradient during early filling (E-wave) to flow blood into the LV. Therefore, the E-wave peak velocity decreases and also decelerates slower. To compensate the blood flow shortage in E-wave, the left atrium contracts more than usual (atrial kick) to provide enough blood in a cardiac cycle. However, in younger people the impaired relaxation pattern is a sign for early stages of diastolic dysfunction as it is defined as Grade I.

2.3.2. **Grade II: Pseudonormal inflow**

Progression in impaired relaxation pattern, the left atrium pressure elevates to provide more pressure gradient between LV and LA and reestablishes a normal pressure gradient. Therefore, the mitral inflow can give the impression of having a normal diastolic function (E/A>1, and DT<180 ms). As a result, the relaxation still remains impaired; moreover, the LV and LA filling pressures are elevated. This stage is titled diastolic dysfunction under pseudonormal mitral inflow, and it is defined as Grade II. Therefore, using Doppler to measure mitral inflow cannot be

sufficient to characterize diastolic dysfunction at this stage, and another modality should be used beside Doppler.

2.3.3. **Grade III: Restrictive pattern**

Increasing LA pressure more and more will cause higher velocity early filling with abrupt deceleration time (DT < 150 ms, peak E-wave velocity > 0.8 m/s, and E/A ratio >2). Therefore, LV filling becomes restrictive. At this stage of diastolic dysfunction, the A-wave becomes shorter, and also atrial systolic dysfunction is usually observed. This pattern is titled as Grade III if it was reversible, and if it was not reversible, it makes as Grade IV. In the progression of diastolic dysfunction, Grade IV is known as the most advanced heart failure with diastolic dysfunction.

2.4. Left ventricular fluid dynamics

Left ventricular fluid dynamics is associated with stroke volume and correspondingly cardiac output (stroke volume × heart rate). Therefore, studying intraventricular fluid flow from fluid mechanics' viewpoint can give us a better understanding of left ventricular functionality. There are different types of modalities for cardiac flow studies, such as MRI and echocardiography. However, there are limitations in flow quantification technics, i.e. temporal and spatial resolutions. As a result, in-vitro studies with high-resolution equipment can help a better understanding of cardiac fluid flow. The primary purpose of this study is studying the diastole phase of the left ventricle, in which the LV fills with blood flow. The inflow jet enters the LV through the mitral valve. It has been reported that a vortex ring is formed inside the LV when the blood flow jet passes the mitral valves and rolling up into the LV. The properties of this formed vortex ring provide us valuable information about the functionality of left ventricle during the filling phase (diastole) (1, 42-44). Therefore, understanding of vortex ring mechanism in such confined domains is essential.

2.5. Vortex ring formation

A vortex ring is a donut-shaped vortex that forms in fluids. In this region, the fluid swirls about an imaginary circular axis and generates a closed circular tube. Vortex rings mostly form in turbulent flows; however, most of the published researches are in laminar vortex rings (45-47). The vortex ring formation has been a topic of study for a few decades and has an essential role in fluid dynamics. In the evolution of vortex ring, Gharib et al. (46) introduced an important non-dimensional parameter, which is called formation number and is defined as $\frac{L}{D} = \frac{\bar{U}_p t}{D}$, where L and D are the piston stroke length and diameter, respectively, in a piston-cylinder arrangement. $\bar{U}_p$ is averaged piston velocity, and t is the total duration of ejection. This time scale corresponds to the moment that the circulation strength of the vortex ring reaches the maximum and, consequently, the onset of vortex ring pinch-off time. They claimed that it is a universal metric (48), and it has an essential role in fluid transportations (44). Gharib et al. (48) used a piston-cylinder arrangement to investigate vortex ring properties in a semi-infinite domain and utilized a range of piston stroke to piston diameter ratio (L/D). They concluded that higher ratios of L/D form a vortex ring are attached to a trailing jet (**Figure 2-6**C). However, the vortices of the vortex ring were not connected to the trailing jet. For the lower stroke to diameter ratios, the vortex ring was detached completely from the tip of the vortex generator (**Figure 2-6**A), which is also called an isolated vortex ring (49). They discovered the transition for the appearance of trailing edge happens at L/D = 4, which they call it formation number. This formation number also recalls as the onset of vortex ring pinch-off in which the vortex ring reaches the maximum circulation value and cannot become stronger anymore.

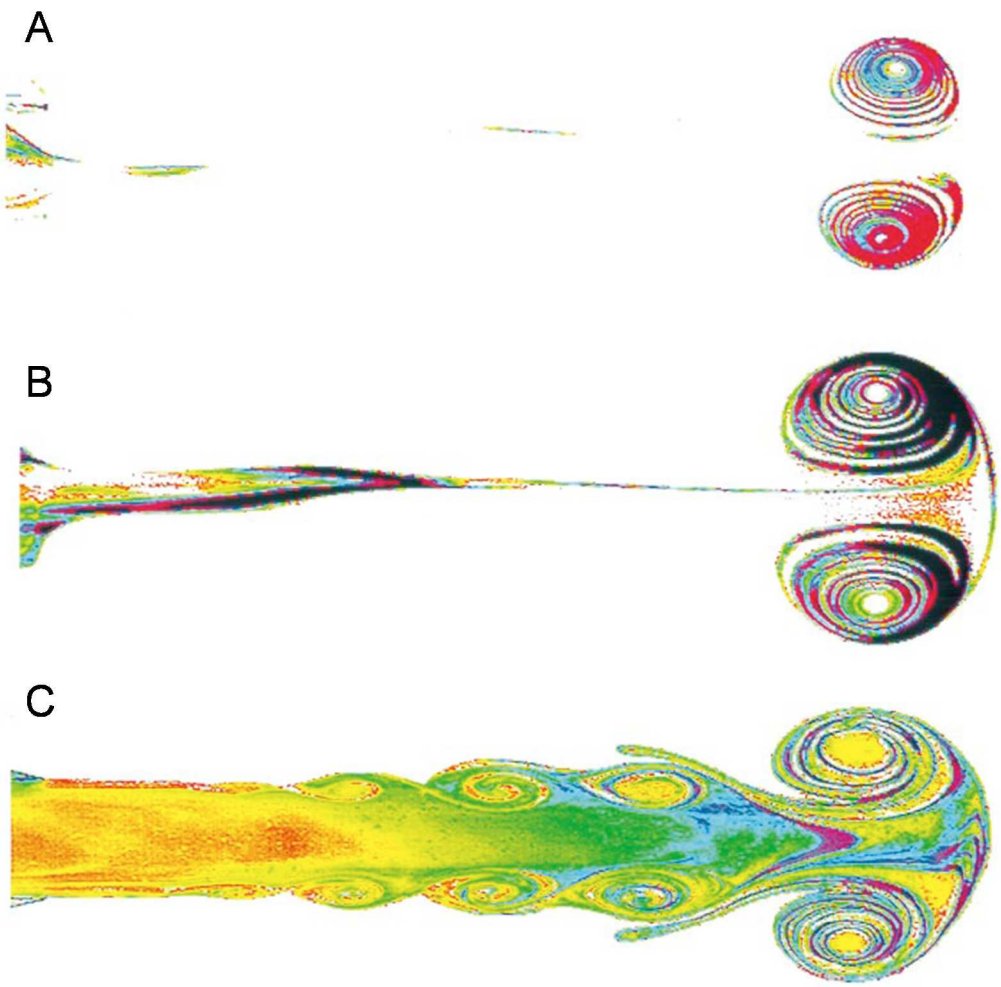

Figure 2-6. Vortex ring visualization for different ratio of piston stroke to piston diameter: a) L/D = 2, b) L/D = 3.8, and c) L/D = 14.5 (48)

Moreover, numerical studies investigated the trajectory and formation of vortex rings generated by a cylinder-piston arrangement (45). In nature, a vortex ring can be produced in various regions from open and semi-infinite regions such as formed vortex rings in the downstream of swimming jellyfish (50) to confined domains such as aortic sinus and left ventricle (51, 52).

2.5.1. **Slug flow model**

A simple representation of vortex generation can be introduced by slug model in which uniform flow with constant velocity, U_0, discharges from a constant diameter, D_0, orifice at a finite short

time interval, T_0. The slug length will be $L_0 = U_0 T_0$. However, we can modify the slug flow model and use for time-variant velocity profile as $\overline{U} = \int_0^T u(t)\,dt$, where u(t) is piston velocity at time t, which is assumed to be uniform over the orifice area. Then the modified slug length will be $L_0 = \int_0^T u(t)\,dt = \overline{U}T$.

A velocity program factor is introduced by Glezer et al. (53), which was accounted for variation of piston velocity as $P = \int_0^1 \frac{u^2}{\overline{U}^2} d\left(\frac{t}{T}\right) = \frac{\overline{u^2}}{\overline{U}^2}$. The values of P for different waveforms were calculated by Diddens as $P_{\text{square wave}} = 1$, $P_{\text{ramp wave}} = 4/3$, and $P_{\text{sine wave}} = 3/2$ (53).

By utilizing the boundary-layer approximation, we can define the peak slug circulation as $\Gamma_{\text{slug,peak}} = \frac{1}{2}\overline{u^2}\,T = p\frac{\overline{U}^2\,T}{2} = p\frac{\overline{U}\,L}{2}$. The peak circulation can be non-dimensionalized by dividing by kinematic viscosity as shown below (53):

$$Re_J = p\frac{\overline{U}\,L}{2\upsilon} \qquad \text{Eq. 2-1}$$

2.5.2. **Semi-infinite domains**

Many studies investigate the vortex formation and properties within semi-infinite domains because the formation of vortex rings usually occurs in semi-infinite domains. A vortex ring can be generated in two ways at laboratories: using a tube or an orifice opening by arranging a cylinder-piston setup. The vortex ring diameter, trajectories, and circulation are examined for both cases (45, 54). The examples of vortex rings in semi-infinite domains are numerous. Fishes, jellyfishes, salps, squids, and many other sea organisms produce a vortex ring and an essential mechanism for their propulsion (50, 55, 56). Dabiri et al. (50) studied and analyzed the generated flow pattern by swimming jellyfish. During the propulsive cycle of swimming jellyfish, vortex rings form in the wake region of the animal. They investigated the coupling between locomotor

and feeding vortex ring by dye visualization (**Figure 2-7**A and **Figure 2-7**B). They concluded vortex ring interaction following one after another helps the jellyfish propulsion. **Figure 2-7**C shows that sunfishes generate optimal vortex rings in their wake and consequently produce maximum thrust force for propulsion underwater (55).

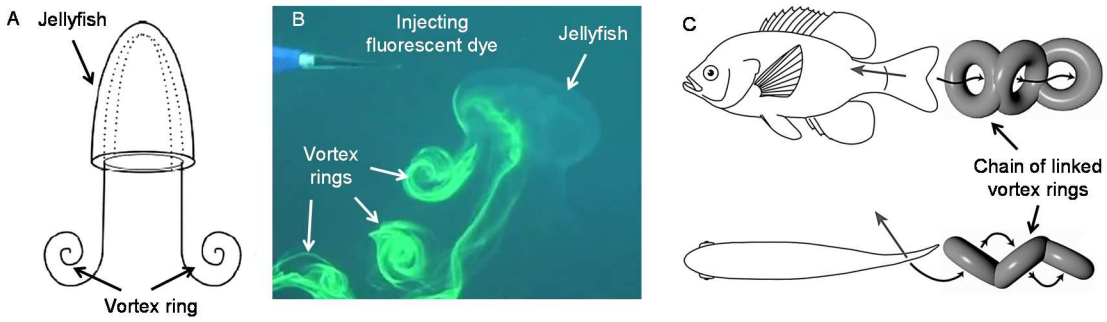

Figure 2-7. Swimming jellyfish and sunfish are an example of vortex ring formation within a semi-infinite domain a) schematic of swimming jellyfish that generates vortex rings in the wake region. b) fluorescent dye injection to visualize wake flow and formed a vortex ring of swimming jellyfish (50). c) front and top view of vortex wake of swimming sunfish that helps the fish for propulsion (55).

In another study, Anderson et al. studied the jet flow structure of swimming squid (56) utilizing particle image velocimetry (PIV) on an adult squid. They also arranged a piston-cylinder setup to mimic the squid jets under the steady condition and studied vortex rings formation and break down by having a wide range of L/D from 5.5 to 61.8, where L and D are piston stroke length and piston diameter, respectively. They observed a few smaller vortex rings combined and makes a more prominent ring that helps the animal for propulsion.

2.5.3. **Confined domains**

Vortex rings sometimes generate in confined domains such as left ventricle walls while it fills with blood during diastole. There are some vortex ring studies on interaction with free surfaces (57), solid walls (46, 58), parallel walls (59), inclined walls (60), and also radially confined domains (61-63). Stewart et al. (62) examined the vortex ring formation inside radially confined domains. They changed the severity of confinement from $D/D_0 = 1.25$ to 3, where D is the

confinement diameter, and D_0 is the constant orifice diameter. They claimed that they found a parameter that can predict the circulation decay in a confined domain based on confinement severity. In another study, they looked at the vortex ring decay in a radially confined domain by changing the piston stroke to diameter ratio from $L/D_0 = 1$ to 7 (61). They concluded the formation number and maximum circulation value remained unchanged by changing L/D_0. Studying vortex rings interaction with confined domains is also essential in studying of swirling flows, which has applications in turbomachinery (64-66).

To the best of our knowledge, both radial and axial confined domains have not been studied systematically, yet. Moreover, all of the previous vortex ring studies are in interaction with rigid walls. Therefore, systematic research on flexible radially-axially confined domain seems essential.

2.5.4. **Intraventricular vortex rings**

The left ventricle filling efficiency and cardiac function can be studied from the fluid mechanics' point of view. During diastole phase, a rapid blood inflow jet enters the left ventricle cavity through the mitral valve and generates a strong vortex ring because of rolling up the shear layers, which helps better blood flow circulation inside the LV and also assists the mitral valve closure (3, 5, 44). Many previous studies addressed the formation of vortex ring during early filling (E-wave) of the left ventricle (2, 44, 51, 67).

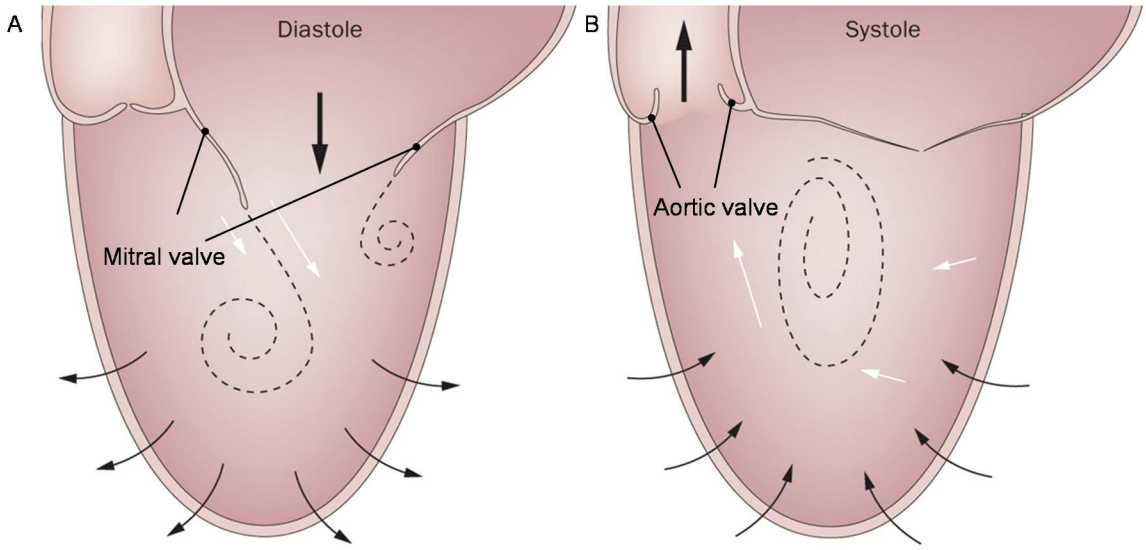

Figure 2-8. Schematic of vortex ring formation inside a healthy left ventricle. A) diastole phase: blood flow enters into the LV cavity through the mitral valve. White arrows on the two sides of the mitral valve leaflet show the velocity difference, which causes the shear layer moving into the LV and rolls up into a vortex ring B) systole phase: the rotating flow guides to the aortic valve by contracting the LV myocardium (5).

Vortex ring formations are not limited to LV, and it has been observed in other parts of the cardiovascular system. For instance, the first acknowledged vortex ring in the cardiovascular system is generating in the aortic sinus during systole (3). The strength of cardiac vortices has a critical role in blood rotating in contact with endocardium and correspondingly myocardial tissue health. As a result, any dysfunction in intraventricular vortex interaction with myocardium can lead to left ventricular remodeling towards heart failure. Therefore, quantification of cardiac flow after cardiac therapy or heart surgery in patients with heart failure can evaluate the procedure and help cardiologists and surgeons in terms of adverse heart remodeling.

2.6. In vivo and in vitro experiments

Previous in-vivo studies on the formed vortex ring inside the left ventricle were mainly compared with a vortex ring in semi-infinite domains. Therefore, it is relevant to study the formation and properties of vortex rings inside an in-vitro LV model with wall interactions. Previous in-vivo studies claimed that the formation number in LV diastole is in the range of 3.5 to 5.5, which can

be calculated based on mean E-wave velocity, duration of E-wave, and mitral valve diameter using Doppler images (44) to assess intraventricular velocity filed (two or three dimensional), and consequently, vortex rings researches use PCMRI (3, 42, 68, 69). In-vivo studies indicate that there is a correlation between vortex ring strength within the left ventricle and LV functionality. Most of the in-vitro studies used PIV to visualize flow patterns and also vortex formation in interested domains. Hatoum et al. studied three different aortic flow (early-peak, mid-peak, and late-peak) past through the aorta in a left heart simulator (70). They concluded that early-peak condition is observed in healthy people, and it is more efficient in terms of energy dissipation and aortic valve functionality.

2.7. References

1. Kheradvar, A., Assadi, R., Falahatpisheh, A., & Sengupta, P. P. (2012). Assessment of transmitral vortex formation in patients with diastolic dysfunction. *Journal of the American Society of Echocardiography*, *25*(2), 220-227.

2. Kheradvar, A., Milano, M., & Gharib, M. (2007). Correlation between vortex ring formation and mitral annulus dynamics during ventricular rapid filling. *Asaio Journal*, *53*(1), 8-16.

3. Kheradvar, A., Rickers, C., Morisawa, D., Kim, M., Hong, G. R., & Pedrizzetti, G. (2019). Diagnostic and prognostic significance of cardiovascular vortex formation. *Journal of cardiology*.

4. Gharib, M., Rambod, E., Kheradvar, A., Sahn, D. J., & Dabiri, J. O. (2006). Optimal vortex formation as an index of cardiac health. *Proceedings of the National Academy of Sciences*, *103*(16), 6305-6308.

5. Pedrizzetti, G., La Canna, G., Alfieri, O., & Tonti, G. (2014). The vortex—an early predictor of cardiovascular outcome?. *Nature Reviews Cardiology*, *11*(9), 545.

6. Betts, J. G., DeSaix, P., Johnson, E., Johnson, J. E., Korol, O., Kruse, D. H., ... & Young, K. A. (2014). Anatomy and physiology.

7. Mankad, R. (2016, February). Ejection fraction: What does it measure?. In *Mayo Clinic* (Vol. 11, No. 2).

8. Gaasch, W. H., & Zile, M. R. (2004). Left ventricular diastolic dysfunction and diastolic heart failure. *Annu. Rev. Med.*, *55*, 373-394.

9. Kitzman, D. W., & Upadhya, B. (2014). Heart failure with preserved ejection fraction: a heterogenous disorder with multifactorial pathophysiology.

10. Leite-Moreira, A. F. (2006). Current perspectives in diastolic dysfunction and diastolic heart failure. *Heart*, *92*(5), 712-718.

11. Maeder, M. T., & Kaye, D. M. (2009). Heart failure with normal left ventricular ejection fraction. *Journal of the American College of Cardiology*, *53*(11), 905-918.

12. Sanderson, J. E. (2007). Heart failure with a normal ejection fraction. *Heart*, *93*(2), 155-158.

13. Garcia, M. J., Thomas, J. D., & Klein, A. L. (1998). New Doppler echocardiographic applications for the study of diastolic function. *Journal of the American College of Cardiology*, *32*(4), 865-875.

14. Oh, J. K. (2007). Echocardiography in heart failure: beyond diagnosis. *European Journal of Echocardiography*, *8*(1), 4-14.

15. Appleton, C. P., Hatle, L. K., & Popp, R. L. (1988). Relation of transmitral flow velocity patterns to left ventricular diastolic function: new insights from a combined hemodynamic and Doppler echocardiographic study. *Journal of the American College of Cardiology*, *12*(2), 426-440.

16. Nagueh, S. F., Appleton, C. P., Gillebert, T. C., Marino, P. N., Oh, J. K., Smiseth, O. A., ... & Evangelisa, A. (2009). Recommendations for the evaluation of left ventricular diastolic function by echocardiography. *European Journal of Echocardiography*, *10*(2), 165-193.

17. Mirsky, I. S. R. A. E. L. (1984). Assessment of diastolic function: suggested methods and future considerations. *Circulation*, *69*(4), 836-841.

18. Borlaug, B. A., & Paulus, W. J. (2010). Heart failure with preserved ejection fraction: pathophysiology, diagnosis, and treatment. *European heart journal*, *32*(6), 670-679.

19. Borlaug, B. A. (2014). The pathophysiology of heart failure with preserved ejection fraction. *Nature Reviews Cardiology*, *11*(9), 507.

20. Ho, J. E., Lyass, A., Lee, D. S., Vasan, R. S., Kannel, W. B., Larson, M. G., & Levy, D. (2013). Predictors of new-onset heart failure: differences in preserved versus reduced ejection fraction. *Circulation: Heart Failure*, *6*(2), 279-286.

21. Khouri, S. J., Maly, G. T., Suh, D. D., & Walsh, T. E. (2004). A practical approach to the echocardiographic evaluation of diastolic function. *Journal of the American Society of Echocardiography*, *17*(3), 290-297.

22. Bursi, F., Weston, S. A., Redfield, M. M., Jacobsen, S. J., Pakhomov, S., Nkomo, V. T., ... & Roger, V. L. (2006). Systolic and diastolic heart failure in the community. *Jama*, *296*(18), 2209-2216.

23. Bhatia, R. S., Tu, J. V., Lee, D. S., Austin, P. C., Fang, J., Haouzi, A., ... & Liu, P. P. (2006). Outcome of heart failure with preserved ejection fraction in a population-based study. *New England Journal of Medicine*, *355*(3), 260-269.

24. Massie, B. M., Carson, P. E., McMurray, J. J., Komajda, M., McKelvie, R., Zile, M. R., ... & Ptaszynska, A. (2008). Irbesartan in patients with heart failure and preserved ejection fraction. *New England Journal of Medicine*, *359*(23), 2456-2467.

25. Maron, B. J. (2003). ACC/ESC clinical expert consensus document on hypertrophic cardiomyopathy: a report of the American College of Cardiology Task Force on Clinical Expert Consensus Documents and the European Society of Cardiology Committee for Practice Guidelines (Committee to Develop an Expert Consensus Document on Hypertrophic Cardiomyopathy). *J Am Coll Cardiol*, *42*, 1687-1713.

26. Maron, B. J., Towbin, J. A., Thiene, G., Antzelevitch, C., Corrado, D., Arnett, D., ... & Young, J. B. (2006). Contemporary definitions and classification of the cardiomyopathies: an American Heart Association scientific statement from the council on clinical cardiology, heart

failure and transplantation committee; quality of care and outcomes research and functional genomics and translational biology interdisciplinary working groups; and council on epidemiology and prevention. *Circulation*, *113*(14), 1807-1816.

27. Elliott, P., Andersson, B., Arbustini, E., Bilinska, Z., Cecchi, F., Charron, P., ... & Monserrat, L. (2007). Classification of the cardiomyopathies: a position statement from the European Society Of Cardiology Working Group on Myocardial and Pericardial Diseases. *European heart journal*, *29*(2), 270-276.

28. Maron, B. J., & Spirito, P. (1998). Implications of left ventricular remodeling in hypertrophic cardiomyopathy. *The American journal of cardiology*, *81*(11), 1339-1344.

29. Westermann, D., Kasner, M., Steendijk, P., Spillmann, F., Riad, A., Weitmann, K., ... & Tschope, C. (2008). Role of left ventricular stiffness in heart failure with normal ejection fraction. *Circulation*, *117*(16), 2051.

30. Zile, M. R., Baicu, C. F., & Gaasch, W. H. (2004). Diastolic heart failure—abnormalities in active relaxation and passive stiffness of the left ventricle. *New England Journal of Medicine*, *350*(19), 1953-1959.

31. Kawaguchi, M., Hay, I., Fetics, B., & Kass, D. A. (2003). Combined ventricular systolic and arterial stiffening in patients with heart failure and preserved ejection fraction: implications for systolic and diastolic reserve limitations. *Circulation*, *107*(5), 714-720.

32. Bonow, R. O. (1991). Left ventricular diastolic function in hypertrophic cardiomyopathy. *Herz*, *16*(1), 13-21.

33. Jefferies, J. L., & Towbin, J. A. (2010). Dilated cardiomyopathy. *The Lancet*, *375*(9716), 752-762.

34. Vanoverschelde, J. L. J., Raphael, D. A., Robert, A. R., & Cosyns, J. R. (1990). Left ventricular filling in dilated cardiomyopathy: Relation to functional class and memodynamics. *Journal of the American College of Cardiology*, *15*(6), 1288-1295.

35. Stevenson, L. W., Tillisch, J. H., Hamilton, M., Luu, M., Chelimsky-Fallick, C., Moriguchi, J., ... & Walden, J. (1990). Importance of hemodynamic response to therapy in predicting survival with ejection fraction≤ 20% secondary to ischemic or nonischemic dilated cardiomyopathy. *The American journal of cardiology*, *66*(19), 1348-1354.

36. Juilliere, Y., Barbier, G., Feldmann, L., Grentzinger, A., Danchin, N., & Cherrier, F. (1997). Additional predictive value of both left and right ventricular ejection fractions on long-term survival in idiopathic dilated cardiomyopathy. *European heart journal*, *18*(2), 276-280.

37. Ho, C. Y. (2007). Echocardiographic assessment of diastolic function. In *Essential Echocardiography* (pp. 119-131). Humana Press.

38. Galderisi, M. (2005). Diastolic dysfunction and diastolic heart failure: diagnostic, prognostic and therapeutic aspects. *Cardiovascular ultrasound*, *3*(1), 9.

39. Tschope, C., & Paulus, W. J. (2009). Echocardiographic evaluation of diastolic function can be used to guide clinical care (response to little and oh).

40. Leong, D. P., De Pasquale, C. G., & Selvanayagam, J. B. (2010). Heart failure with normal ejection fraction: the complementary roles of echocardiography and CMR imaging. *JACC: Cardiovascular Imaging*, *3*(4), 409-420.

41. Nagueh, S. F., Middleton, K. J., Kopelen, H. A., Zoghbi, W. A., & Quiñones, M. A. (1997). Doppler tissue imaging: a noninvasive technique for evaluation of left ventricular relaxation and estimation of filling pressures. *Journal of the American College of Cardiology*, *30*(6), 1527-1533.

42. Hong, G. R., Pedrizzetti, G., Tonti, G., Li, P., Wei, Z., Kim, J. K., ... & Narula, J. (2008). Characterization and quantification of vortex flow in the human left ventricle by contrast echocardiography using vector particle image velocimetry. *JACC: Cardiovascular Imaging*, *1*(6), 705-717.

43. Bermejo, J., Benito, Y., Alhama, M., Yotti, R., Martínez-Legazpi, P., Del Villar, C. P., ... & Fernández-Avilés, F. (2014). Intraventricular vortex properties in nonischemic dilated cardiomyopathy. *American Journal of Physiology-Heart and Circulatory Physiology*, *306*(5), H718-H729.

44. Gharib, M., Rambod, E., Kheradvar, A., Sahn, D. J., & Dabiri, J. O. (2006). Optimal vortex formation as an index of cardiac health. *Proceedings of the National Academy of Sciences*, *103*(16), 6305-6308.

45. Krueger, P. S. (2008). Circulation and trajectories of vortex rings formed from tube and orifice openings. *Physica D: Nonlinear Phenomena*, *237*(14-17), 2218-2222.

46. Weigand, A., & Gharib, M. (1997). On the evolution of laminar vortex rings. *Experiments in Fluids*, *22*(6), 447.

47. Didden, N. (1979). On the formation of vortex rings: rolling-up and production of circulation. *Zeitschrift für angewandte Mathematik und Physik ZAMP*, *30*(1), 101-116.

48. Gharib, M., Rambod, E., & Shariff, K. (1998). A universal time scale for vortex ring formation. *Journal of Fluid Mechanics*, *360*, 121-140.

49. Dabiri, J. O., & Gharib, M. (2004). Fluid entrainment by isolated vortex rings. *Journal of fluid mechanics*, *511*, 311-331.

50. Dabiri, J. O., Colin, S. P., Costello, J. H., & Gharib, M. (2005). Flow patterns generated by oblate medusan jellyfish: field measurements and laboratory analyses. *Journal of Experimental Biology*, *208*(7), 1257-1265.

51. Töger, J., Kanski, M., Carlsson, M., Kovács, S. J., Söderlind, G., Arheden, H., & Heiberg, E. (2012). Vortex ring formation in the left ventricle of the heart: analysis by 4D flow MRI and Lagrangian coherent structures. *Annals of biomedical engineering*, *40*(12), 2652-2662.

52. Moore, B., & Dasi, L. P. (2014). Spatiotemporal complexity of the aortic sinus vortex. *Experiments in fluids*, *55*(7), 1770.

53. Glezer, A. (1988). The formation of vortex rings. *The Physics of fluids*, *31*(12), 3532-3542.

54. Pullin, D. I. (1979). Vortex ring formation at tube and orifice openings. *The Physics of Fluids*, *22*(3), 401-403.

55. Linden, P. F., & Turner, J. S. (2004). 'Optimal'vortex rings and aquatic propulsion mechanisms. *Proceedings of the Royal Society of London. Series B: Biological Sciences*, *271*(1539), 647-653.

56. Anderson, E. J., & Grosenbaugh, M. A. (2005). Jet flow in steadily swimming adult squid. *Journal of Experimental Biology*, *208*(6), 1125-1146.

57. Gharib, M., & Weigand, A. (1996). Experimental studies of vortex disconnection and connection at a free surface. *Journal of Fluid Mechanics*, *321*, 59-86.

58. Rockwell, D. (1998). Vortex-body interactions. *Annual review of fluid mechanics*, *30*(1), 199-229.

59. Chang, T. Y., Hertzberg, J. R., & Kerr, R. M. (1997). Three-dimensional vortex/wall interaction: Entrainment in numerical simulation and experiment. *Physics of Fluids*, *9*(1), 57-66.

60. Lim, T. T. (1989). An experimental study of a vortex ring interacting with an inclined wall. *Experiments in Fluids*, *7*(7), 453-463.

61. Stewart, K. C., Niebel, C. L., Jung, S., & Vlachos, P. P. (2012). The decay of confined vortex rings. *Experiments in Fluids*, *53*(1), 163-171.

62. Stewart, K. C., & Vlachos, P. P. (2012). Vortex rings in radially confined domains. *Experiments in fluids*, *53*(4), 1033-1044.

63. Danaila, I., Kaplanski, F., & Sazhin, S. (2015). Modelling of confined vortex rings. *Journal of Fluid Mechanics*, *774*, 267-297.

64. Gharakhani, A., & Ghoniem, A. F. (1998). Simulation of the piston driven flow inside a cylinder with an eccentric port.

65. Escudier, M. P., Bornstein, J., & Maxworthy, T. (1982). The dynamics of confined vortices. *Proceedings of the Royal Society of London. A. Mathematical and Physical Sciences*, *382*(1783), 335-360.

66. Escudier, M. (1988). Vortex breakdown: observations and explanations. *Progress in Aerospace Sciences*, *25*(2), 189-229.

67. Pedrizzetti, G., Domenichini, F., & Tonti, G. (2010). On the left ventricular vortex reversal after mitral valve replacement. *Annals of biomedical engineering*, *38*(3), 769-773.

68. Wong, K. K., Kelso, R. M., Worthley, S. G., Sanders, P., Mazumdar, J., & Abbott, D. (2009). Cardiac flow analysis applied to phase contrast magnetic resonance imaging of the heart. *Annals of biomedical engineering*, *37*(8), 1495-1515.

69. Kerwin, W., Hertzberg, J., Cooke, J., Chluda, H., Shandas, R., & Gill, E. (2004, April). Vorticity imaging of diastolic cardiac inflow by phase-contrast MRI. In *2004 2nd IEEE*

International Symposium on Biomedical Imaging: Nano to Macro (IEEE Cat No. 04EX821) (pp. 300-303). IEEE.

70. Hatoum, H., Moore, B. L., & Dasi, L. P. (2018). On the significance of systolic flow waveform on aortic valve energy loss. *Annals of biomedical engineering*, *46*(12), 2102-2111.

CHAPTER III

3. VORTEX RING DECAY IN FLEXIBLE-WALLED SPHEROIDAL CONFINED DOMAINS

Abstract: Recent studies investigated the decay of vortex rings in radially confined domains; however, they overlooked the effects of confinement flexibility and also axially confinement. A biological example of both radially and axially flexible confined domain is the formation of vortex rings in the left ventricle (LV) as blood flow passes through the mitral valve into the LV cavity. We hypothesized that the rate of circulation decay increases in more axially confined domains. To investigate our hypothesis, we arranged a cylinder-piston setup to generate laminar vortex rings. The method we used to create and analyze vortex rings was verified with previously published data on radially confined domains. 2D time-resolved PIV was used to quantify the flow fields within three different aspect ratios of spheroidal silicon models (0.8, 1, and 1.25) under different filling duration (T = 110 ms and 211 ms), Reynolds number (Re = 1400, 1700, and 2600), and piston velocity profile (sharp ramp-up, sinewave, and sharp ramp-down waveforms). Velocity vector filed, vorticity contours, and circulation values were measured and calculated for all cases. The formation number and peak circulation value remained unaffected by changing the shape of silicon models. However, for the cases with the same filling duration, the vortex ring pinched-off earlier for cases with shorter acceleration time (sharp ramp-up waveform). Increasing

the Reynolds number led to increasing in vortex ring size and eventually caused earlier decay since the bigger vortex ring was more affected by walls. We quantified the rate of circulation decay for all cases and we noticed an increased decay rate by changing the model from semi-prolate (less axially confined) to semi-oblate (more axially confined). Moreover, vortex ring circulation decayed faster by increasing Reynolds number. The results can enhance our understanding of vortex behavior in restricted spheroidal domains, such as left ventricle.

Keywords: Laminar vortex rings, particle image velocimetry, flexible confinement, circulation decay, pinch-off time.

3.1. Introduction

Vortex rings can be identified as an essential feature of flow in wide ranges of phenomena from jellyfish and squid propulsion to blood flow discharges into the aortic sinus (during systole) and the left ventricular cavity (during diastole). The fluid mechanics of the vortex ring has been investigated in numerous experimental, analytical, and numerical studies. Fundamental studies on vortex ring size, trajectories, evolution, and circulation reveal a valuable understanding of vortex ring nature (1-4). Gharib et al. set up a cylinder-piston arrangement to generate vortex rings in the laboratory, and they showed that the core region vorticity of vortex ring has a Gaussian distribution (5). After that, they investigated the evolution and formation of the laminar vortex ring, fundamentally in semi-infinite domains (5). They introduced a universal time scale (formation number), which was defined as L/D, where L is the piston stroke (the column of ejected fluid from a cylinder with a diameter of D), and D is piston diameter. They showed the vortex ring peak circulation occurs at the time of formation number. The circulation cannot grow after the formation number and the vortex ring detaches from the trailing jet (pinch-off time), which is valuable information. The energy maximization theory has also predicted vortex pinch-off (6). The maximum achievable formation number is approximately four, and after that, the

vortex ring cannot hold additional vorticity and trailing jet formed behind it (7). The constraint on the growth of the vortex ring brings up a question about the existence of an "optimal vortex ring," which is whether we can produce the most potent vortex ring with minimum energy. Surprisingly, recent studies showed that some kinds of jellyfish and also juvenile squids take advantage of an optimal vortex ring in their propulsion (8, 9). Moreover, the formation number of a formed vortex ring in the left ventricle during diastole is close to four for a healthy LV, and this value can be used as an index of cardiac health (10-13). Some experimental and computational studies verified the universality of the formation number (14-16).

Several experimental and numerical studies have looked at vortex ring interaction with rigid objects such as a wall which is vertical or inclined to the direction of flow (17, 18), and also within two parallel walls (19). Walker et al. experimentally examined the vortex ring interaction with the flow adjacent to the wall using dye to visualize flow in water, and they studied the developed boundary layer on the wall (17). They concluded secondary vorticities with the opposite direction of rotation are formed on the wall because of unsteady separation in the boundary layer. This process continued until a secondary vortex ring is fully ejected from the boundary layer and interacts with the primary vortex (18). Lim et al. experimentally examined the interaction of inclined ejected vortex ring with a wall and also with another vortex ring (18). They showed that the formation of the secondary vortex (with the opposite direction of the primary vortex ring) is due to the no-slip condition at the wall (18). In another study, Chang et al. studied vortex ring interaction within two parallel plates numerically and validated their results by experimental approach (19). They investigated the vorticity layer formation at the wall. They concluded that during the attaching of the secondary vortex ring to the primary one, the secondary vortex stretches and generates helical axial waves and pushes the fluid away from the wall, and generates two helical flows from the wall to the vortex ring, which eventually causes the vortex ring breakdown (19). Most of the studies on vortex ring interaction with walls focused on secondary formed vortical structures during vortex interactions

with walls. These studies revealed valuable and fundamental information for understanding the vortex rings interaction with more complex geometries, such as the left ventricular cavity. There are few recent experimental (20, 21) and numerical (22) studies on vortex ring interaction with radially rigid confined domains. Stewart et al. examined the effects of the radial confinement on vortex propagation under 1) different confinement ratios and 2) different piston-stroke-to-diameter ratios. They concluded vortex circulation peak had lower values and also decayed earlier in more confined domains. However, the vortex ring pinch-off was not influenced by changing confinement ratio. Also, they developed a model to predict the circulation decay for a specific radial confinement (21).

To the best of our awareness, there has not been a fundamental study on vortex ring formation within both radial and axial confinement with flexible walls. The current study examined the dynamics of vortex rings within spheroidal confined domains with different aspect ratios under different test conditions, i.e. Reynolds number, piston velocity profile, and filling time.

3.2. Material and methods

3.2.1. **Experimental setup**

A cylinder-piston arrangement was designed in this study to generate vortex rings inside flexible confined domains, and properties of vortex rings were examined. A programmable piston pump (programmable piston pump PPP, Vivitro Systems Inc., Victoria, Canada) was used to drive fluid flow into semi-spheroidal silicon models, which were transparent and flexible (40A shore hardness). Pump outflow was measured instantaneously by an ultrasonic flowmeter (Transonic Systems Inc., Ithaca, NY). A PVC pipe with a constant inside diameter of $D_0 = 12.7$ mm was used as an orifice in upstream of the silicon model, and the region of interest started just after the end of the orifice, as shown in **Figure 3-1A**.

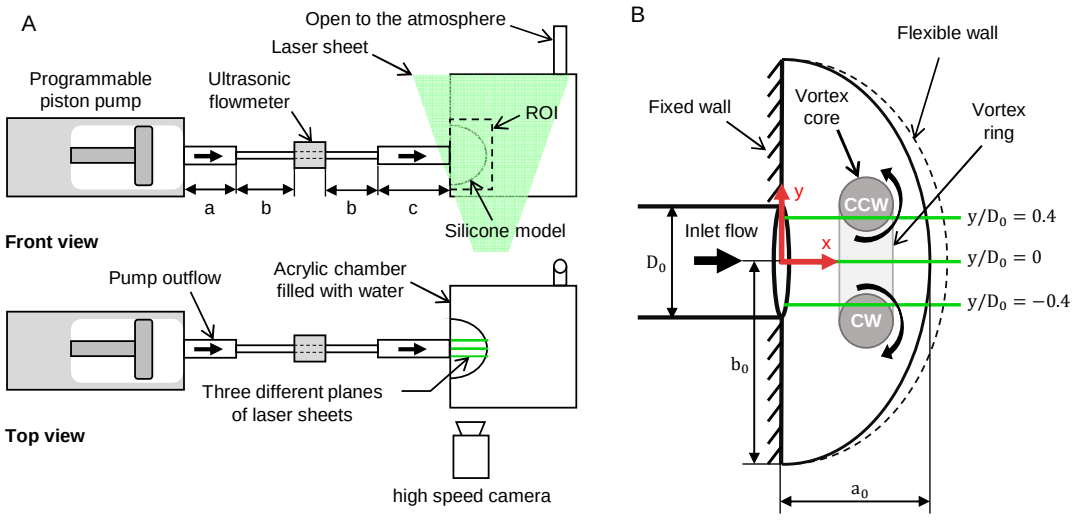

Figure 3-1. Experimental arrangement used in this study. A) Front and top views of vortex generator and PIV setup. Flexible-walled silicon models were filled into a clear acrylic chamber that was filled with water and open to the atmosphere. The flow rate was measured by a clamp-on ultrasonic flowmeter attached to a 200 mm long tube. Different pipes were used in the flow circuit, with length of a = 110 mm (ID = 15mm), b = 85 mm (ID = 13mm), and c = 185 mm (ID = 12.7mm). B) Flexible-walled semi-spheroidal confined domain. 2D PIV measurements were acquired at three parallel planes that were each illuminated with a laser sheet. The orifice diameter is D_0 = 12.7 mm. The shape of the bag is defined as $\left(\frac{x}{a_0}\right)^2 + \left(\frac{y}{b_0}\right)^2 + \left(\frac{z}{b_0}\right)^2 = 1$ ($0<x<a_0$, $-b_0<y<b_0$, $-b_0<z<b_0$) , where a_0 and b_0 are defined in the figure and z is normal to the plane based on the right-handed coordinates. ROI = region of interest, ID = inside diameter, CW = clockwise, and CCW = counterclockwise.

The silicon model was secured in an acrylic chamber, and both inside and outside of the silicon model were filled with water at room temperature. A vortex ring was generated by sudden flow discharge from the orifice and traveled through the end of the silicon model, which is demonstrated in **Figure 3-1B** with the corresponding coordinate system. To let the silicon model expand spontaneously without any external resistance, we connected the chamber to the atmosphere through a vertical column. We should note that the flexible walls moved passively since the flow was directly injected into the silicon model (unlike the intraventricular flow in the left ventricle, which is caused by muscle relaxation). The mathematical equation of semi-spheroidal models is as follows:

$$\left(\frac{x}{a_0}\right)^2 + \left(\frac{y}{b_0}\right)^2 + \left(\frac{z}{b_0}\right)^2 = 1, \qquad \text{Eq. 3-1}$$

where $-a_0 < x < a_0$, $-b_0 < y < b_0$, $-b_0 < z < b_0$. Three different flexible-walled semi-spheroidal models with aspect ratios of a_0/b_0 = 0.8, 1.0, and 1.25 were examined for this study, as shown in **Figure 3-2A**. The inflow rate (or velocity) had two phases: a ramp up or acceleration and a ramp down or deceleration, and the associated time with these two phases were called acceleration time (AT) and deceleration time (DT), respectively (**Figure 3-2B**). We examined the influence of AT/DT ratio on vortex mechanics in flexible-walled confined domains for three conditions of rapid acceleration (AT/DT<1), mild acceleration-deceleration (AT/DT~1), and rapid deceleration (AT/DT>1). **Figure 3-2C** shows normalized piston displacement prescribed to the programmable piston pump for three different AT/DT ratio. The summation of AT and DT determined the filling time, T = AT+DT. We examined two different filling times (T = 110 ms and 211 ms) for this study. **Figure 3-2D** shows normalized piston displacement prescribed for the programmable piston pump according to two different filling times.

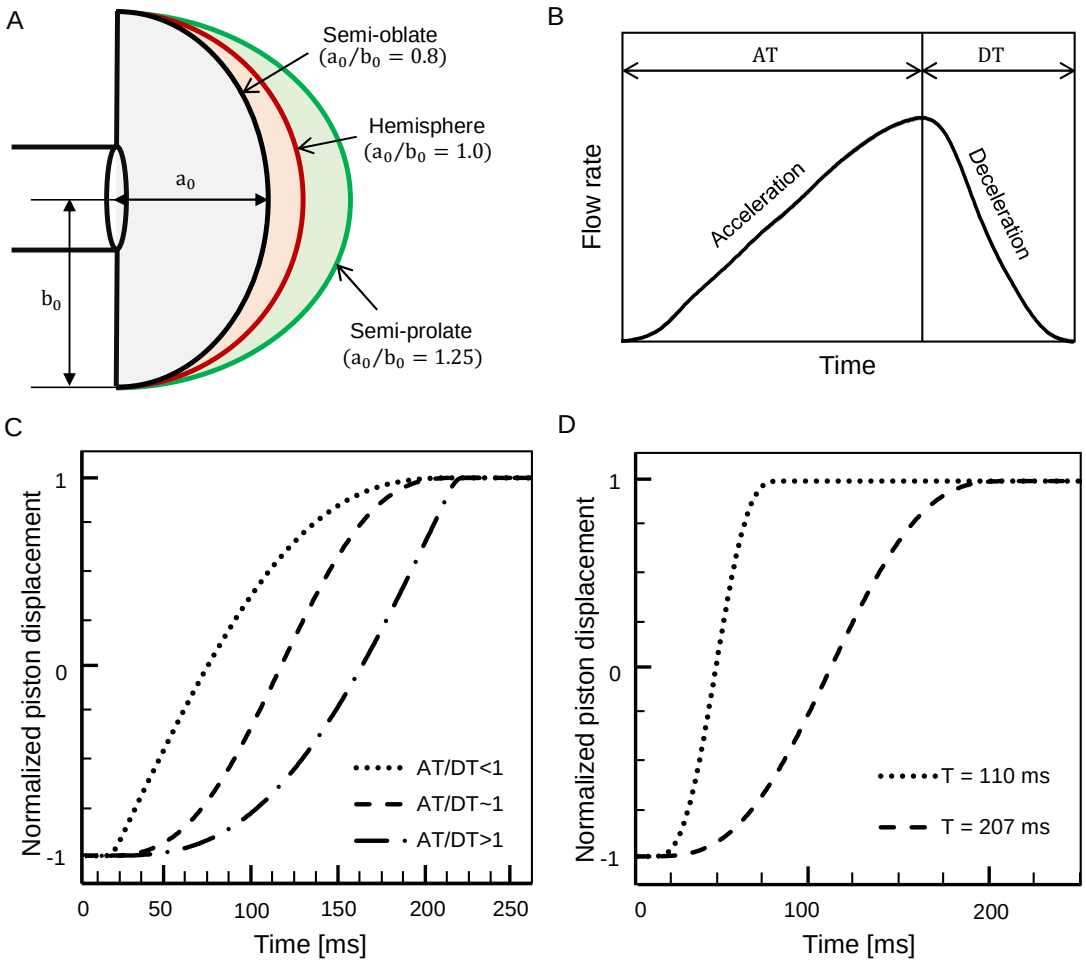

Figure 3-2. Test conditions examined in this study. A) Three flexible-walled semi-spheroidal models with different aspect ratio (a_0 / b_0) of: 0.8 (semi-oblate), 1.0 (hemisphere), and 1.25 (semi-prolate). B) Definition of acceleration time (AT) to deceleration time (DT) ratio (AT/DT) for a sample flow rate. C) Normalized piston displacement prescribed for three different AT/DT ratios: AT/DT<1, AT/DT~1, AT/DT>1, where filling time (T) is 211 ms. Exact values for different test conditions of AT/DT are provided in **Table 3-1**. D) Normalized piston displacement prescribed for three T: T = 110 ms, T = 211 ms, and T = 366 ms, where AT/DT~1. Increasing the pump gain in c and d will result in an increased flow rate. Three different Reynolds numbers (Re) of 1400, 1700, and 2600 were considered for this study.

The prescribed piston displacements in **Figure 3-2c** and **Figure 3-2d** were normalized waveforms. As a result**,** pump gain determined the piston velocity magnitude and consequently, inflow and Reynolds number (Re). Three different Re = 1400, 1700, and 2600 were examined for this study, as shown in **Figure 3-3**. Reynolds number was defined as $\mathrm{Re} = \frac{U_{ave} D_0}{\upsilon}$, where U_{ave} was the average piston velocity, D_0 was the orifice diameter, and υ was the kinematic viscosity of

water at room temperature. **Figure 3-3** shows the average values of 10 consecutive measured inflow waveforms in all different physical models. Each plot provides three AT/DT ratios for three Re at a specific filling time. The Reynolds values are displayed only in **Figure 3-3a** to avoid redundancy. Exact values of DT and AT/DT ratios for all filling times (T) and all of the silicon models are provided in **Table 3-1**.

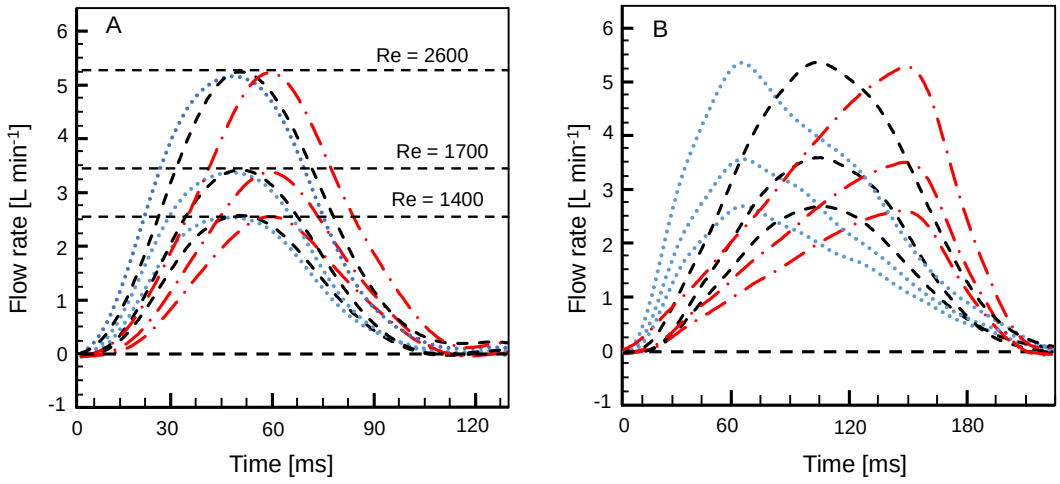

Figure 3-3. Averaged values of 10 inlet flow rate cycles for all physical models (semi-oblate, hemisphere, and semi-prolate), Re (1400, 1700, and 2600), and AT/DT ratios examined in this study. A) T = 110±2 ms, nad B) T = 211±8 ms, AT/DT<1: dotted line; AT/DT~1: dashed line; and AT/DT>1: dash-dotted line.

All the DT, and AT/DT values in **Table 3-1** were according to the averages and standard deviations of ten consecutive cycles of measured inflow under three different Reynolds numbers (Re = 1400, 1700, and 2600) at each physical model. The values of DT and AT/DT did not alter by changing Re for each case, as we expected, and it is observable in **Figure 3-3**. The second column represents the expected AT/DT ratios according to the prescribed piston displacement waveforms.

Table 3-1: Measured DT and AT/DT ratios for all test conditions. Three filling times (T = 110 ms, 211 ms, and 366 ms) under three different AT/DT ratios. Each value in the table was measured from the average of ten consecutive cycles. The expected AT/DT was based on the piston displacement waveforms.

Filling time	Expected AT/DT	Semi-oblate		Hemisphere		Semi-prolate	
		DT [ms]	AT/DT	DT [ms]	AT/DT	DT [ms]	AT/DT
T = 110±6 ms	AT/DT<1	64±1	0.75±0.04	66±2	0.68±0.04	62±1	0.74±0.04
	AT/DT~1	53±1	1.05±0.06	56±1	1.02±0.06	55±1	1.02±0.06
	AT/DT>1	42±1	1.62±0.12	44±1	1.45±0.11	40±1	1.57±0.13
T = 211±8 ms	AT/DT<1	141±2	0.43±0.03	150±2	0.36±0.02	141±2	0.44±0.03
	AT/DT~1	102±2	1.03±0.04	106±2	0.91±0.04	108±2	0.96±0.04
	AT/DT>1	69±2	2.19±0.13	60±2	2.51±0.15	67±2	2.27±0.14
T = 366±11 ms	AT/DT<1	298±2	0.21±0.01	311±2	0.18±0.01	294±2	0.21±0.01
	AT/DT~1	180±2	1.04±0.03	184±2	0.98±0.03	177±2	1.07±0.03
	AT/DT>1	46±2	7.17±0.50	49±2	7.29±0.51	47±2	7.01±0.48

3.2.2. **Vortex ring formation under active filling**

The direct pumping inflow into the silicon model caused the vortex generation, as we described in **Figure 3-1**. In this case, the elastic walls of the model are moved passively as we name it passive-filling. However, in some other applications, the source of the flow is wall movement, as we title it as active-filling. Transmitral inflow during E-wave (in which the left ventricle (LV) wall relaxation is the cause of blood flow jet entrance into the LV) is an example of active-filling (23). In contrast, transmitral inflow during A-wave (in which the contraction of left atrium pushes the blood flow into the LV) is an example of passive-filling (24). Therefore, it is valuable to compare vortex properties in active-filling and passive-filling.

A very similar setup with small modification was used to generate vortex rings inside a flexible semi-spheroidal silicon model under active-filling. The piston pump drove water into a sealed acrylic chamber, was filled with water and held the silicon model. The water inside the silicon model was connected to the atmosphere through a PVC pipe with an inside diameter of D_0 = 12.7 mm and a tube with ID = 13 mm. The pump was in contact with outside of the silicon model, and the piston movement caused the silicon wall movement, and it eventually led to run a fluid flow

inside the silicon model. An adjustable resistance was used at the end of the tube to stabilize flow and absorb systematic fluctuations. A clamps-on ultrasonic flowmeter (Transonic Systems Inc., Ithaca, NY) was used to monitor the flow inside the silicon model. A vortex ring was generated by sudden discharge from an orifice with a constant diameter of D_0 (**Figure 3-4**b). It is important to note that the silicon walls were moved actively.

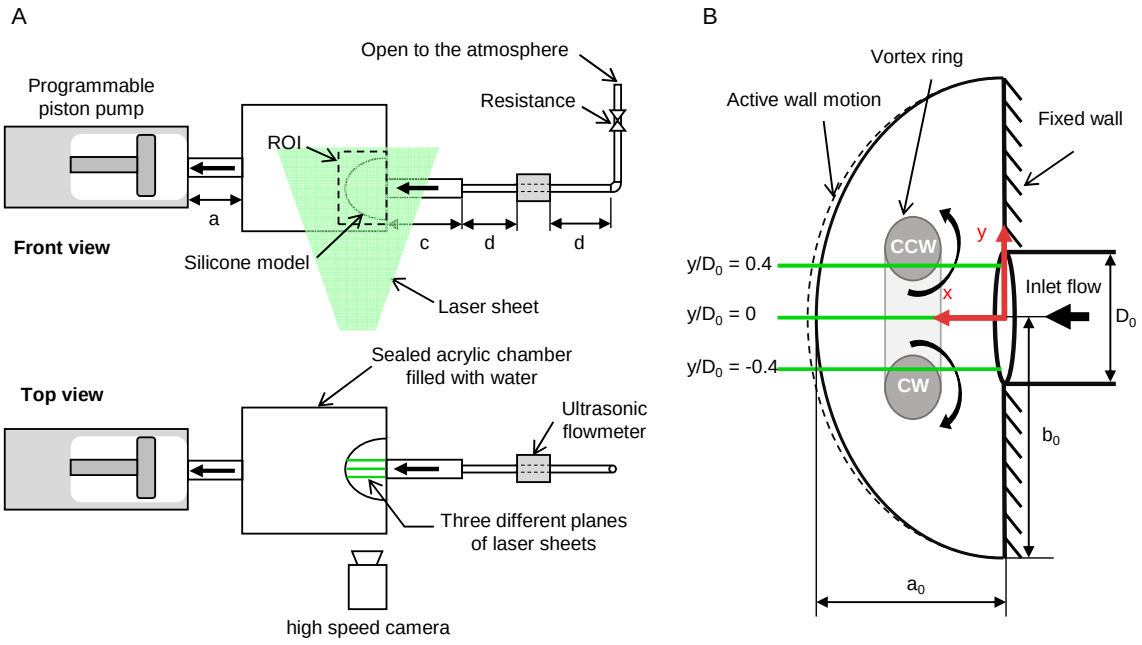

Figure 3-4. Experimental setup. a) Front and top views of vortex generator and PIV setup. A flexible-walled silicon model of semi-spheroidal geometry was mounted on a clear acrylic chamber and open to the atmosphere. The flow rate was measured by a clamp-on ultrasonic flowmeter attached to a 200 mm long tube. Different pipes were used in the flow circuit, with length of c = 185 mm (ID = 12.7mm) and d = 85 mm (ID = 13mm). b) Flexible-walled semi-spheroidal confined domain. 2D PIV measurements were acquired at 3 parallel planes that were each illuminated with a laser sheet. The orifice diameter is D_0 = 12.7 mm. The shape of the bag is defined as $x^2/a_0 + y^2/b_0 + z^2/b_0 = 1$ ($0<x<a_0$, $-b_0<y<b_0$, $-b_0<z<b_0$) , where a_0 and b_0 are defined in the figure and z is normal to the plane. ID = inside diameter, CW = clockwise, and CCW = counterclockwise.

We studied three different velocity profiles by changing the ratio of acceleration time (AT) to deceleration time (DT) as AT/DT<1, AT/DT~1, and AT/DT>1, which is demonstrated in **Figure 3-5**a. All three velocity profiles were examined under four different Reynolds numbers (Re = 800, 1350, 2400, and 3350) by changing piston stroke length in a specified time. All test

conditions are shown in **Figure 3-5**b. The Re was defined based on averaged velocity as $Re = \frac{\bar{U}D_0}{\upsilon}$, where $\bar{U} = \frac{4}{\pi T {D_0}^2}\int_0^T Q(t)\,dt$ and Q(t) was the instantaneous flow rate.

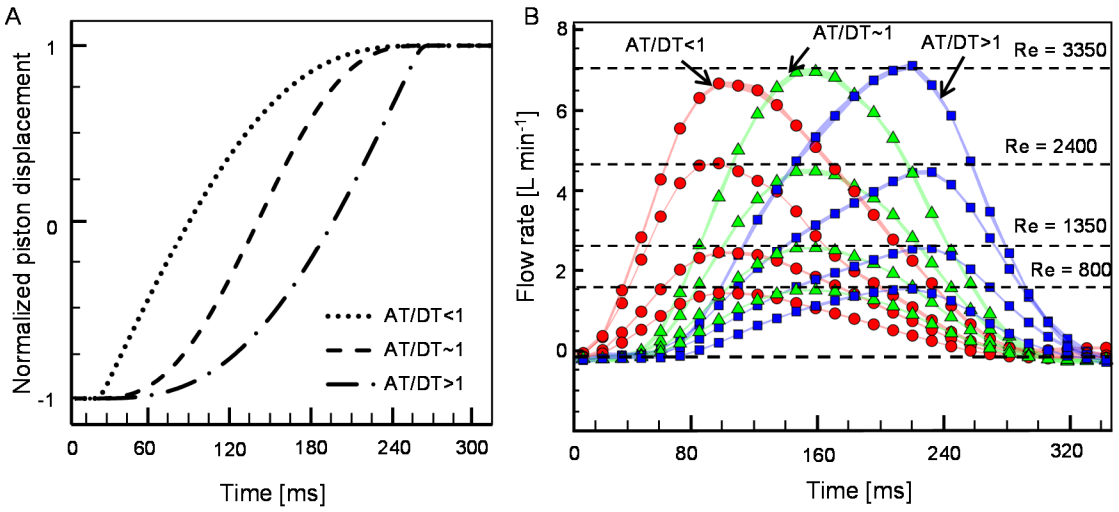

Figure 3-5. Test conditions examined in this study. a) Normalized piston displacement prescribed for three different At/DT ratios: AT/DT<1, AT/DT~1, AT/DT>1, where filling time (T) is 270 ms. b) Averaged values of 10 inlet flow rate cycles at different Re (800, 1350, 2400, and 3350), and different AT/DT ratios. Increasing the pump gain resulted in an increased flow rate and correspondingly the Reynolds number.

3.2.3.**Validation**

To validate our experimental setup, we first arranged a radially-confined domain setup similar to previous studies, and we compared the results with published data (25). The fluid was discharged from a cylindrical orifice (D_0 = 12.7 mm) and generated a vortex ring inside an optically transparent cylindrical confined domain (D = 22.2 mm). The ratio of the piston stroke to diameter (L/D_0) was equal to 1.2, which was corresponded to laminar flow with Re = 1700 ($Re = \frac{U_{ave}D_0}{\upsilon}$). The field of view began exactly from the tip of the orifice to ten orifice-diameter in downstream.

3.2.4.**Particle image velocimetry (PIV)**

Fluid flow was visualized by utilizing 2D time-resolved particle image velocimetry (2D TR-PIV) (**Figure 3-1**a). The fluid in the circuit was seeded with polymethyl methacrylate (PMMA)

fluorescent particles with a diameter of 1-20 µm, 532 nm excitation, and 584 nm emission (LaVision GmbH, Göttingen, Germany). For illuminating the plane of interest in silicon models, a high-speed Nd: YLF laser with a single cavity (Photonics Industries International, Inc., NY, USA) was used at 20 mJ/pulse and three different repetition rates based on flow velocity: 1 kHz, 1.25 kHz, and 1.66 kHz (**Figure 3-1**). The laser beam was focused by using a pair of converging-diverging lenses and transformed into a laser sheet by placing a cylindrical lens with 10 mm focal length. A high-speed 1 MP CMOS camera (Phantom Miro 110, Vision Research Inc., Wayne, NJ, USA) with a resolution of 1280×800 pixels (the spatial resolution was 113 µm) was used for recording images. Ten cycles were acquired from the beginning of vortex ring formation to break down. A 550 nm long-pass filter lens was attached on a 60 mm constant focal length lens (Nikon Micro Nikkor, Nikon Corporation, Tokyo, Japan) on the camera for observing the illuminated particles (wavelength > 550 nm). The camera frame rate was set in 1000, 1250, and 1660 frames per second based on flow velocity to match with laser repetition rates. The camera and laser were triggered precisely at the starting time of filling. Fifty cycles ran before acquiring PIV data for satisfying the repeatability. Besides the central plane, two other parallel planes on both sides of the central plane with equal distances were observed ($y/D_0 = \pm 0.4$, where D_0 was the diameter of the orifice). To ensure the distances of off-centered planes from the central plane were exactly symmetric on both sides, we mounted the housing acrylic chamber on a traverse with the resolution of 20 revolutions to 1 inch. Therefore, we moved the acrylic chamber (and consequently the physical model), and kept the camera and laser sheet stationary in order to have different y-positions.

We processed the PIV data in DaVis 8.3.0 software (LaVision GmbH, Göttingen, Germany). Multi-pass cross-correlation with the initial interrogation window size of 64×64 pixels (2 passes) to a final window size of 32×32 pixels with 50% overlap was used. In pre-processing, the background was subtracted with a scale length of 5 pixels. In post-processing, empty vectors were

replaced by the velocity vectors with a peak ratio of less than 0.1 m/s. After post-processing, all six cycles for each experiment were exported as DAT files for analyzing using Tecplot 360 (Tecplot, Inc., Bellevue, WA) or custom-written scripts in MATLAB (The Mathworks, Inc., Natick, MA). Vorticity contours were plotted in Tecplot after averaging six cycles, but the rest of the results, e.g., circulation, were analyzed based on single cycle analyzing and after that averaging was executed to achieve mean and standard deviation of analyzed data.

3.2.5. **Definitions of calculated quantities**

3.2.5.1. Formation time and Formation number.

Laminar vortex rings have been investigated for a wide range of applications, and Garib et al. (7) introduced formation time as a non-dimensional parameter, which is defined as follows:

$$T^* = \frac{\overline{U}\, t}{D_0} \qquad \text{Eq. 3-2}$$

where D_0 is orifice diameter, and $\overline{U}$ is averaged velocity during a filling time and was calculated as $\overline{U} = \frac{4}{\pi T {D_0}^2} \int_0^T Q(t)\, dt$, where T is the total duration of filing time, and Q(t) is instantaneous inflow. Gharib et al. also showed that the circulation value of a vortex ring cannot grow more than a specific number and will pinch off after that time point. They claimed that the onset of vortex ring pinch-off is a universal number, which is called formation number and is defined as $FN = \frac{L}{D_0} = \frac{\overline{U}\, T}{D_0}$, where L is piston stroke length and L/D_0 is also called stroke ratio.

3.2.5.2. Vorticity.

In this study, the vorticity dynamics were calculated to investigate vortex development in the silicon models for different inflow patterns. Physically, the tendency of a fluid flow to rotate describes as vorticity and mathematically, it is defined as the curl of a velocity field, $\vec{V}$. The out-

of-plane z-vorticity field (ω_z) with units of s^{-1} was calculated from PIV-based 2D velocity vector field (V_x, V_y) and it was calculated using the following equation:

$$\omega_z = \nabla \times \vec{V} = -(\frac{dV_x}{dy} - \frac{dV_y}{dx}) \quad \text{Eq. 3-3}$$

where V_x and V_y refer to the x- and y-component of the velocity vector field. The normalized vorticity field was displayed in this study, and it was defined as follows:

$$\omega^* = \frac{\omega_z D_0}{U_{max}} \quad \text{Eq. 3-4}$$

3.2.5.3. Vortex identification and circulation.

The filling vortex ring was a three-dimensional donut-shaped flow structure. In the case of 2D visualization of the flow (as in the current study), only a cross-section of the 3D flow structure can be observed, and it appears in the form of two counter-rotating vortices. However, two off-center planes on both sides of the central PIV plane ($y/D_0 = \pm 0.4$) were observed for evaluating the symmetricity of vortex rings. Both clockwise (CW) and counterclockwise(CCW) vortex cores were identified from the processed PIV data using the swirling strength criterion (26), which is defined as the imaginary part of the complex eigenvalue of the velocity gradient tensor:

$$\lambda_{ci} = \mathrm{Im}[\mathrm{eig}(\nabla u)] = \frac{1}{2}\,\mathrm{Im}\left[\sqrt{\left(\frac{du}{dx} - \frac{dv}{dy}\right)^2 + 4\frac{du}{dy}.\frac{dv}{dx}}\right] \quad \text{Eq. 3-5}$$

The iso-surfaces of λci were normalized by 2.6% of the maximum value, as recommended in previous studies (27). After identifying both CW and CCW vortex cores, we automatically tracked each vortex core at a time for the entire period of vortex ring appearance to breakdown.

Circulation, Γ (in units of $cm^2\ s^{-1}$) was calculated to quantify the strength of a filling vortex, by integrating the out-of-plane z-vorticity, ω_z, over the surface area enclosed by the vortex A, as:

$$\Gamma = \iint_A \omega_z \, dA = \sum_A (\omega_z \, dx \, dy) \qquad \text{Eq. 3-6}$$

We used negative and positive signs for CW and CCW circulations, respectively. Circulation provides a large-scale estimate of the rotational strength of a vortex. Previous studies of vortex rings have examined this quantity using 2D PIV in physical models (20, 28), and semi-infinite domains (10, 29).

3.2.5.4. Slug flow model

A simple representation of vortex generation can be introduced by slug model in which uniform flow with constant velocity, U_0, discharges from a constant diameter, D_0, orifice at a finite short time interval, T_0. The slug length will be $L_0 = U_0 T_0$. However, we can modify the slug flow model and use for time-variant velocity profile as $\overline{U} = \int_0^T u(t)\, dt$, where u(t) is piston velocity at time t, which is assumed to be uniform over the orifice area. Then the modified slug length will be $L_0 = \int_0^T u(t)\, dt = \overline{U}T$.

A velocity program factor is introduced by Glezer et al. (4), which was accounted for variation of piston velocity as $P = \int_0^1 \frac{u^2}{\overline{U^2}} d\left(\frac{t}{T}\right) = \frac{\overline{u^2}}{\overline{U^2}}$. The values of P for different waveforms were calculated by Diddens as $P_{\text{square wave}} = 1$, $P_{\text{ramp wave}} = 4/3$, and $P_{\text{sine wave}} = 3/2$ (4). In this study, the calculated velocity program factor for the velocity profiles with AT/DT<1 and AT/DT>1 was in the range of 1.35 to 1.42, which was corresponded to value for a ramp wave of 4/3, and for the velocity profiles with AT/DT~1 was in the range of 1.49 to 1.59, which was corresponded to value for a sine wave of 3/2.

The peak slug circulation is defined by boundary-layer approximation as $\Gamma_{slug,peak} = \frac{1}{2}\overline{u^2}\,T = p\frac{\bar{U}^2\,T}{2} = p\frac{\bar{U}\,L}{2}$. The peak circulation can be non-dimensionalized by dividing by kinematic viscosity as shown below:

$$Re_J = p\frac{\bar{U}\,L}{2\upsilon} \qquad \text{Eq. 3-7}$$

3.2.5.5. Pressure calculation.

We obtained the velocity filed (u, v) from 2D-PIV measurements, and we used a MATLAB script to estimate the pressure filed corresponding to the velocity vector field (30). The MATLAB script calculates pressure gradient from the Navier–Stokes equation:

$$\nabla p = -\rho\left(\frac{Du}{Dt} - \upsilon\nabla^2 u\right) \qquad \text{Eq. 3-8}$$

By path integration through the pressure gradient, the pressure field can be calculated:

$$p_2 - p_1 = \int_{x_1}^{x_2} \nabla p dx \qquad \text{Eq. 3-9}$$

3.2.6. Defining the vortex ring pinch-off time (formation time)

The vortex ring can obtain a specific amount of circulation strength and after that, the isolated vortex ring detaches from the trailing jet. By definition, this time is known as the pinch-off time, in which the maximum circulation occurs. We used the change point method to calculate this point statistically. In this method, we calculated the cumulative-sum of the difference between mean circulation and actual circulation in the vicinity of the pinch of time. We assumed the vicinity of the pinch-off time within the first time point in which the circulation reaches 60% of

the peak value and the first time pint in which the circulation drops to 90% of the peak value. The maximum value of the cumulative sum was labeled as the formation time.

3.3. Results and discussion

3.3.1. **Experimental setup Validation**

We validated our experimental setup with the previous vortex ring study on radially confined domains (21). Two different conditions of a) semi-infinite domain and b) radially a domain with normalized confinement ratio of $D/D_0 = 1.75$ were considered, where D and D_0 were the diameter of cylindrical confinement and orifice, respectively as shown in **Figure 3-6**. We used piston displacement as an input for our programmable pump in this study. As a result, we integrated the reported piston velocity (21) in time to achieve the piston displacement waveform. Instantaneous velocity was calculated by measured flow rate, Q, divided by the cross-sectional area of the orifice as $u_{piston} = 4Q/{D_0}^2$. **Figure 3-6B** shows a comparison between the used piston velocity in this study for validation and the one from published data (21). 2D PIV was used to visualize the axial center-plane of the cylindrical confined domain to characterize the generated vortex ring properties. Normalized circulation values versus non-dimensional time (formation time, $T^* = \frac{U_{ave}t}{D_0}$, where U_{ave} was time-averaged piston velocity) were plotted for two different cases of semi-infinite and confined domains, and results were compared with published data (21)).

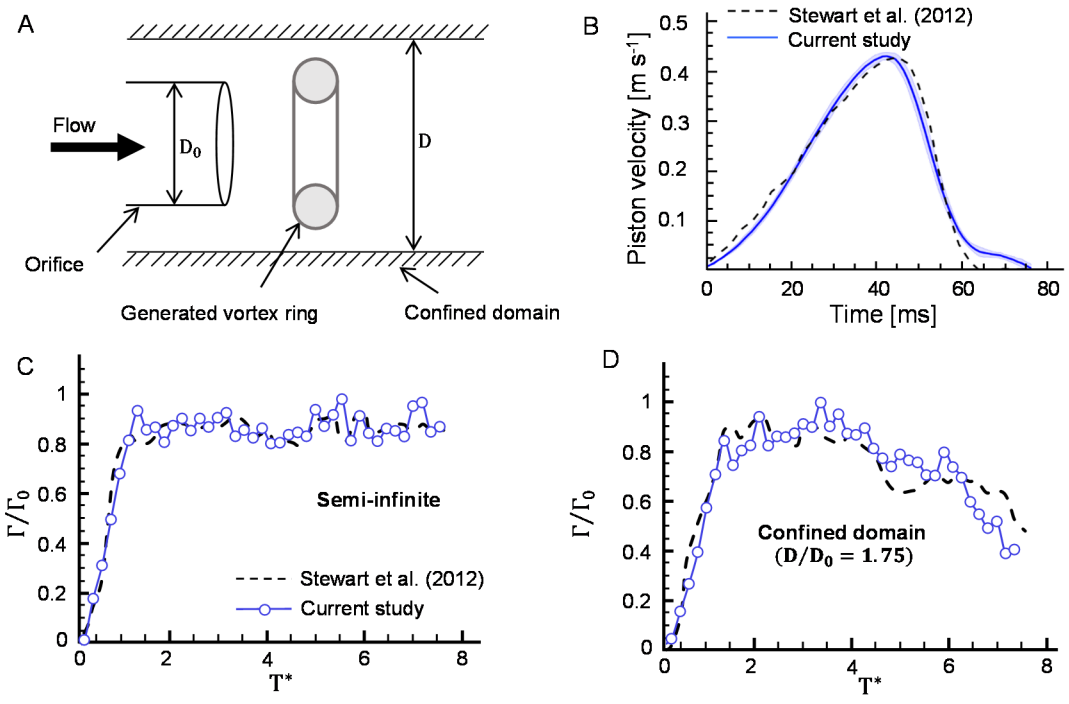

Figure 3-6. Experimental setup and results for validation of methods used in this study by conditions with Stewart et al. (Experiments in Fluids 53 (1), 2012). A) Schematic of cylindrical confined domain with a ratio of $D/D_0 = 1.75$, where D and D_0 were the diameter of confinement and the orifice, respectively. B) Comparison of piston velocity profile used for validation study and published data. C) Comparison of normalized circulation for semi-infinite domain, and D) confined domain ($D/D_0 = 1.75$). The standard deviations of the average of 10 cycles for both negative and positive circulation were 7% and 9% for the semi-infinite and confined domain, respectively. $T^* = \frac{U_{ave}t}{D_0}$ indicates non-dimensional time, where U_{ave} was time average of piston velocity.

The values from published data were very comparable with the results from this study for similar conditions (semi-infinite and radially confined domain with $D/D_0 = 1.75$); however, there was a slight discrepancy between two results for the confined domain case in the decay portion. The possible reason could be associated with the extreme confined condition ($D/D_0 < 2$), in which circulation decay became very sensitive to changing the confinement ratio. As reported in previous studies (25) the onset of circulation decay was varied significantly by changing D/D_0 ratio from 2 to 1.5 as opposed to the cases with $D/D_0 > 3$. Therefore, the slight divergence in the circulation decay between this study and published data in **Figure 3-6B** is entirely acceptable. The ratio of the piston to diameter in this validation study was $L/D_0 = 1.2$, which was in good

agreement with circulation pinch-off time ($T^* = 1.21 \pm 0.03$) for both semi-infinite and radially confinement in this study.

After validation of our methodology in this study (21), the behavior of vortex rings in flexible-walled semi-spheroidal confined domains was examined under different conditions to explore the variation in vortex ring properties, i.e. vortex formation, circulation decay rate, and vorticity patterns. The test conditions were considered on the effects of confinement shape (semi-oblate, hemisphere, and semi-prolate); effects of piston velocity profile (AT/DT<1, AT/DT~1, and AT/DT>1); effects of filling time (T = 110 ms and T = 211 ms); and effects of filling Reynolds number (Re = 1400, Re = 1700, and Re = 2600) on fluid flow and vortex ring properties. Therefore, the overall of 54 test conditions were examined in this study. The detailed results for each condition are presented in the following subsections.

3.3.2. **Effects of semi-spheroidal confinement aspect ratio on vortex ring properties**

Vortex ring properties and behaviors were examined at three different physical models with aspect ratios of a_0/b_0 = 0.8, 1, and 1.25 in this study. In this section, the vorticity contours, vortex circulation, and vortex core positions were presented for the case with $T = 211$ ms, $AT/DT \sim 1$, and $Re = 1700$ at centered PIV plane ($y/D_0 = 0$) and two off-center PIV planes ($y/D_0 = \pm 0.4$). We assumed the vortex ring propagated symmetric in confined domains since the axis of the orifice was aligned perfectly with the axial axis of rotation of semi-spheroidal physical models. To quantify the probable non-symmetric propagation of vortex ring and also in properties in this study, two off-center cross-sections of vortex rings ($y/D_0 = \pm 0.4$) were examined and compared with each other, which is elaborated.

3.3.2.1. Vorticity contours

The normalized out-of-plane vorticity field ($\omega^* = \frac{\omega_z D_0}{U_{max}}$) demonstrated as contours with different levels for the case with $T = 211$ ms, $AT/DT \sim 1$, and $Re = 1700$ at centered PIV plane ($y/D_0 = 0$) in **Figure 3-7** and one of the off-center PIV planes ($y/D_0 = 0.4$) in **Figure 3-8**. In both figures, the first, second, and third rows were corresponded to semi-oblate, hemisphere, and semi-prolate confinements, respectively. Positive (CCW) and negative (CW) vorticities are displayed as solid and dashed lines, respectively. Seven different levels with equal increments of 14% were considered from 10% to 94% of maximum vorticity of the entire cycle. Five different time points were chosen to display. The flow is from left to right at every single plot. In general, a set of counter-rotating vortex cores are visible, which grew from the leftmost column and broke down at the rightmost column. In the first column (a, f, and k), the vortex ring reached half of the maximum circulation strength, where $\Gamma/\Gamma_0 \sim 0.5$. At this point, the vortex ring was attached to the orifice (base of the models) regardless of the shape of confinement. In the second column (b, g, and l), the circulation strength reached the maximum value($\Gamma/\Gamma_0 \sim 1$) and it cannot grow more. At this point, the vortex ring pinched-off from the trailing jet and traveled by its own. The properties of vortex rings, i.e., circulation, vortex ring size, and propagation speed, were not affected by confinement shapes at this point. According to Stwart et al. (25), a vortex ring did not get affected by a confined domain with $D/D_0 > 3$, where D and D_0 were the diameter of confinement and orifice, respectively. At this stage (b, g, and l) the position vortex ring was was corresponded to $D/D_0 > 4$. As a result, we did not see any difference in the formation of vortex rings at this stage across different physical models. After this point, the vortex ring traveled with constant circulation strength until the onset of decay. We should note that from the second column afterward, the bag shape did not change since there was no more inflow from the orifice, and the vortex ring travels by its momentum. The third column corresponds to halfway between pinch-off

time and the start of circulation decay. At this stage, a set of vorticies with opposite signs were generated at the walls nearby to the vortex cores.

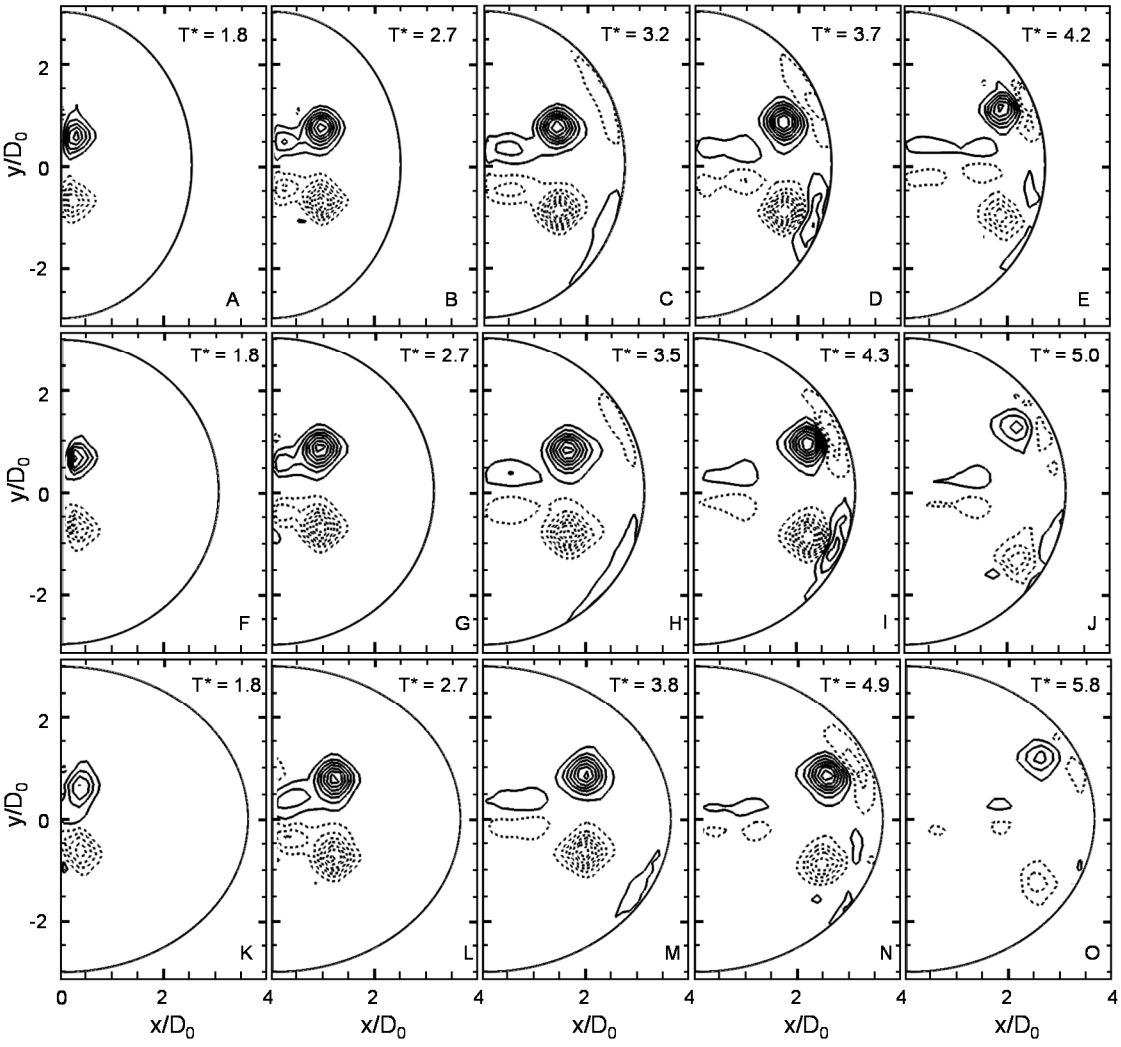

Figure 3-7. Normalized out-of-plane z-vorticity contours at the central plane ($y/D_0 = 0$) at different time points for each silicone model at $T = 211$ ms, $AT/DT \sim 1$, and $Re = 1700$. a-e) Semi-oblate, f-j) Hemisphere, and k-o) Semi-prolate models. Based on circulation values, five different time points are shown for each model. At a, f, and k, the vortex ring reaches half of the peak circulation ($\Gamma/\Gamma_0 \sim 0.5$). At b, g, and l, the vortex ring pinches off from the trailing jet. At d, i, and n, the vortex ring circulation starts to decay. Time points in c, h, and m occur in between pinch-off and onset of circulation decay, where the circulation has reached a constant peak. The vortex ring breaks down at e, j, and o. Dashed and solid lines represent negative and positive vorticity, respectively. The minimum contour level is 10% of $|\omega^*_{max}| = 7.25$, where $\omega^* = \frac{\omega_z D_0}{U_{max}}$ and the maximum level is 94% of $|\omega^*_{max}|$. Seven levels are shown with equal 14% increments for both negative and positive vorticities.

As we can see, the formed vorticies at the wall were more significant for semi-oblate shape, which means the vortex ring would decay faster for the more axial confined model. However, the value of vortex ring decay should be quantified by an in-depth analysis of vortex ring for different cases. In the fourth column (d, I, and n), the vortex ring started to decay, and the circulation strength was absorbed by the formed vortex ring at the walls.

Normalized vorticity contours at the off-central plane ($y/D_0 = 0.4$) are displayed in **Figure 3-8**. The same conditions and exact time points as **Figure 3-7** were chosen to demonstrate the trend of the vortex ring from the formation (leftmost column) to breakdown (rightmost column). Similar patterns were noticed as **Figure 3-7**; however, there were some differences between the vortex cores corresponded to the center and off-centered PIV plane. First, the two vortex cores in **Figure 3-8** were more oval-shaped, and also the distance between the two was shorter compared to the vortex cores in **Figure 3-7**. Plus, there was no trailing jet captured in the off-centered plane, which means the trailing jet mostly existed in the center of the vortex ring.

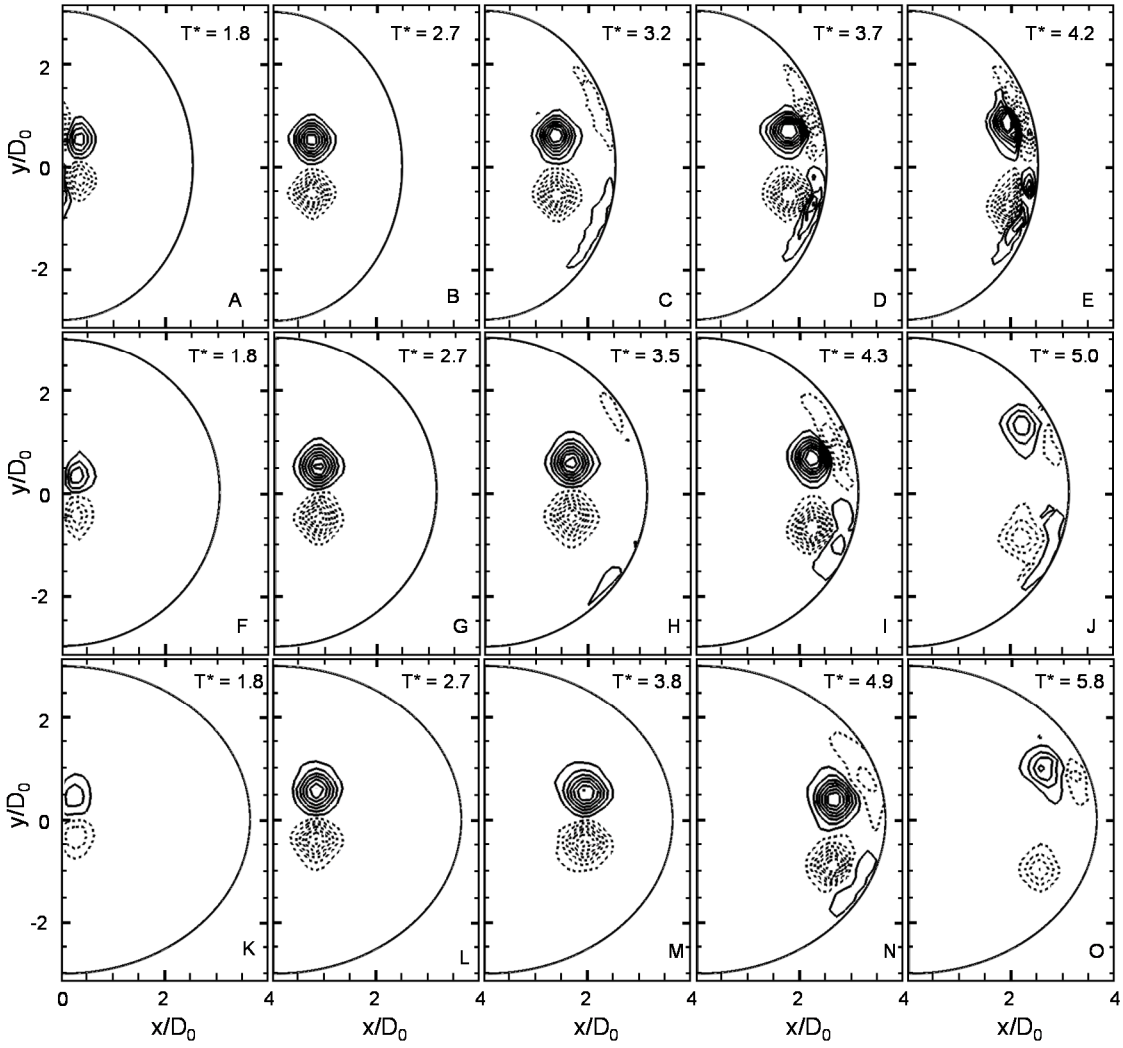

Figure 3-8. Normalized out-of-plane z-vorticity contours at the off-central plane ($y/D_0 = 0.4$) at different time points for each silicone model at $T = 211$ ms, $AT/DT \sim 1$, and $Re = 1700$. a-e) Semi-oblate, f-j) Hemisphere, and k-o) Semi-prolate models. Based on circulation values, five different time points are shown for each model. At a, f, and k, the vortex ring reaches half of the peak circulation ($\Gamma/\Gamma_0 \sim 0.5$). At b, g, and l, the vortex ring pinches off from the trailing jet. At d, i, and n, the vortex ring circulation starts to decay. Time points in c, h, and m occur in between pinch-off and onset of circulation decay, where the circulation has reached a constant peak. The vortex ring breaks down at e, j, and o. Dashed and solid lines represent negative and positive vorticity, respectively. The minimum contour level is 10% of $|\omega^*_{max}| = 7.25$, and the maximum level is 94% of $|\omega^*_{max}|$. Seven levels are shown with equal 14% increments for both negative and positive vorticities.

3.3.2.2. Vortex Circulation

The vortex ring circulation strengths for all three different shapes (circle, triangle, and square represent semi-oblate, hemisphere, and semi-prolate, respectively.) with filling time of $T = 211$ ms, $AT/DT \sim 1$, and $Re = 1700$ were plotted versus time for the centered PIV plane, $y/D_0 = 0$ (filled markers), and two off-centered PIV planes of $y/D_0 = 0.4$ (gray colored markers), and $y/D_0 = -0.4$ (hollow markers) in **Figure 3-9a**.

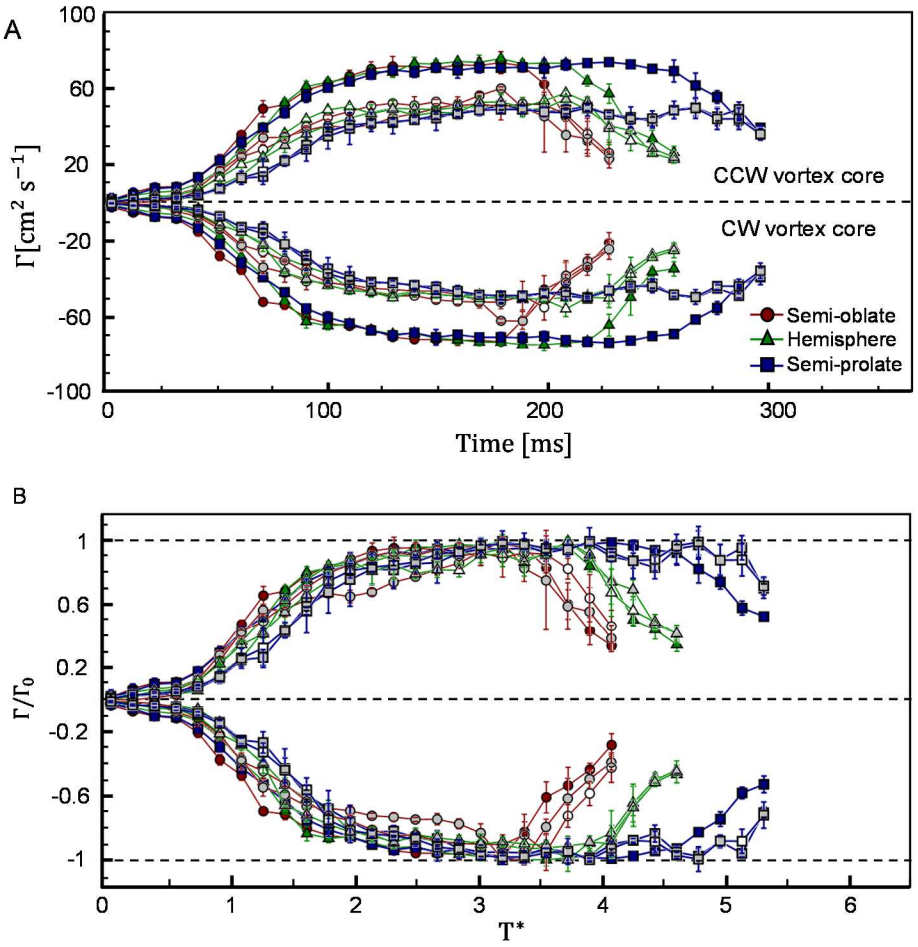

Figure 3-9. Vortex ring circulation for $T = 211$ ms, $AT/DT \sim 1$, and $Re = 1700$. A) Dimensional circulation versus time. Filled markers correspond to the centered PIV plane ($y/D_0 = 0$). Gray-colored and hollow markers correspond to off-center PIV planes at $y/D_0 =$

0.4 and $y/D_0 = -0.4$, respectively. B) Normalized circulation versus non-dimensional time $T^* = \frac{U_{ave}t}{D_0}$.

The circulation was normalized by peak circulation, Γ_0, and plotted versus non-dimensional timescale (formation time), $T^* = \frac{U_{ave}t}{D_0}$, and displays in **Figure 3-9b**. Positive and negative values of circulation in both figures is corresponded to CCW and CW vortex cores, respectively.

All the circulation plots in **Figure 3-9** had the same trend of the increasing, plateau, and then decreasing. The overall circulation values corresponded to off-center planes were lower than the centered PIV plane because the off-centered planes did not cut through the vortex ring orthogonally, and as a result, the actual circulation strength value could not be achieved. However, the trend of circulation strength variation was similar between the values corresponded to the off-center plane and the center plane. The averaged difference of circulation values between two off-centered planes was less than 4%. By normalizing circulation by Γ_0, the plots corresponded to different planes of PIV were more comparable. The normalized circulation grew until attained the maximum value of $\Gamma/\Gamma_0 \sim 1$ at $T^* \sim 2.5$ regardless of the shape of confined domains. After that, the vortex rings were pinched-off from the jet, and the vortex rin could not gain more strength. Shortly after the pinch-off time (depending on piston velocities this time was varied between $\Delta T^* = 0.1 - 1.2$), the piston was stopped form moving and the fully expanded silicon models had not inflated anymore since there was no more feeding flow rate injected from the orifice into the silicon models. At this point, the circulation strength had constant values of $\Gamma/\Gamma_0 \sim 1$ until the vortex ring became close to the end of the confinement and began to decay until it broke down. The onset of decay was $T^* \sim 3.5, 3.8, and\ 4.5$ for semi-oblate, hemisphere, and semi-prolate confinements, respectively. We should note that at all different conditions in this study, the silicon models were already expanded before the vortex ring affected by physical model walls and starting to decay.

3.3.2.3. Characteristics of Filling Jets

Both CW and CCW vortex cores were tracked automatically in time from the time of appearance to the time of breakdown. The X and Y positions of CW and CCW vortex cores are displayed in **Figure 3-10**. The difference between y positions tells us the vortex ring size, which can be normalized with orifice diameter (D_{VR}/D_0). As shown in **Figure 3-10A**, the initial size of the vortex rings was not affected by the shape of confinement and had a value of $D_{VR}/D_0 = 1 \pm 0.15$ for the vortex rings correspond to the centered PIV plane (filled markers). The vortex ring size did not remain constant in this study. The value of D_{VR}/D_0 grew irrespective to the shape of confinement until the onset of decay ($D_{VR}/D_0 \sim 1.52$). After vortex ring decay started, the more axial confined shaped showed a higher rate of growth in D_{VR}/D_0. The curvature of physical models played a critical role in vortex ring size and also decay rate. It is observable from **Figure 3-10A** that the overall size of the vortex ring was bigger at the centered PIV plane compare to off-centered planes; however, the Y-position trends between different planes of PIV was similar. We also looked at the X-positions of vortex cores and the difference between CW and CCW core positions, as shown in **Figure 3-10B**. The slope of X-position versus time tells us the vortex ring propagation speed. As we can see in all the models, the slope of the X-position increased from zero to a constant value and then decreased to zero, again. Therefore, two time-points were interesting: first, the onset of X-position slope became constant (pinch-off time) and second, the onset of X-position slope started to decrease (start of decay time). These two points examined for all cases and were perfectly matched with the corresponding circulation plots in **Figure 3-9B**. The vortex ring seems to have higher propagation speed in the semi-prolate model compare to the hemisphere and semi-prolate models. Plus, the vortex ring higher penetration into the semi-prolate model due to having a lower wall curvature in comparison with the hemisphere and semi-prolate models. Comparing the X and Y positions of vortex cores between two off-

centered planes, we can claim the vortex ring propagates symmetrically within the physical models in this study.

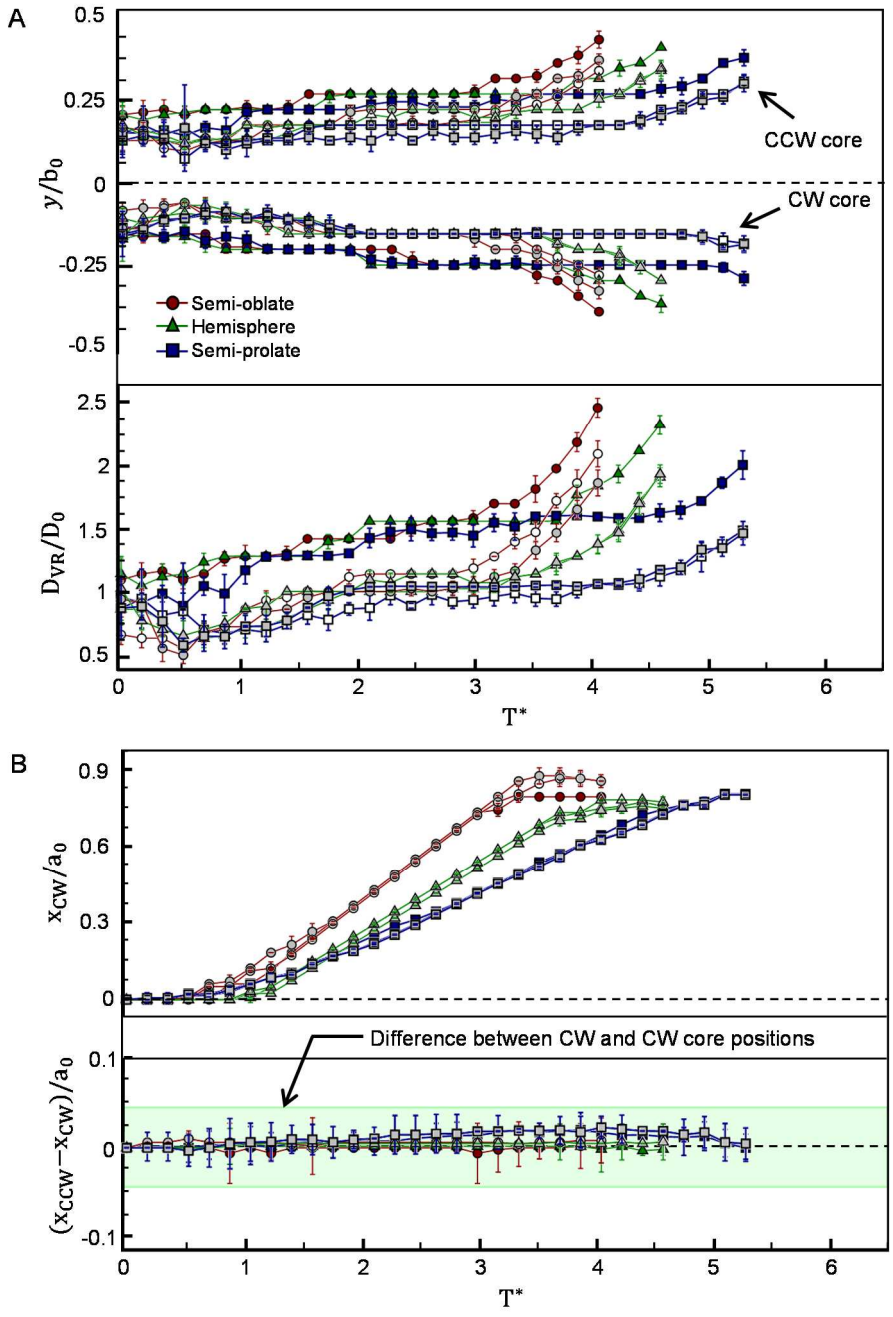

Figure 3-10. Non-dimensional position of CW and CCW vortex cores. A) Y-position (non-dimensionalized by model base radius, b_0) and nondimensional vortex ring diameter, D_{VR}/D_0. B) X-position of CW vortex core (non-dimensionalized by model major axial length, a_0). The difference between the non-dimensional x-position of CW and CCW vortex cores is shown.

We observed that circulation decayed earlier for the more confined domain. Also, the non-dimensional x had a higher slope in the semi-oblate case. Therefore, there should be a relation between the geometry of the confinement and the circulation plot. We introduced a modified time scale as a formation time based on the geometry of confinement as below:

$$T^* = \frac{U_{ave}t}{D_0\sqrt{\frac{a_0}{b_0}}} \qquad \text{Eq. 3-10}$$

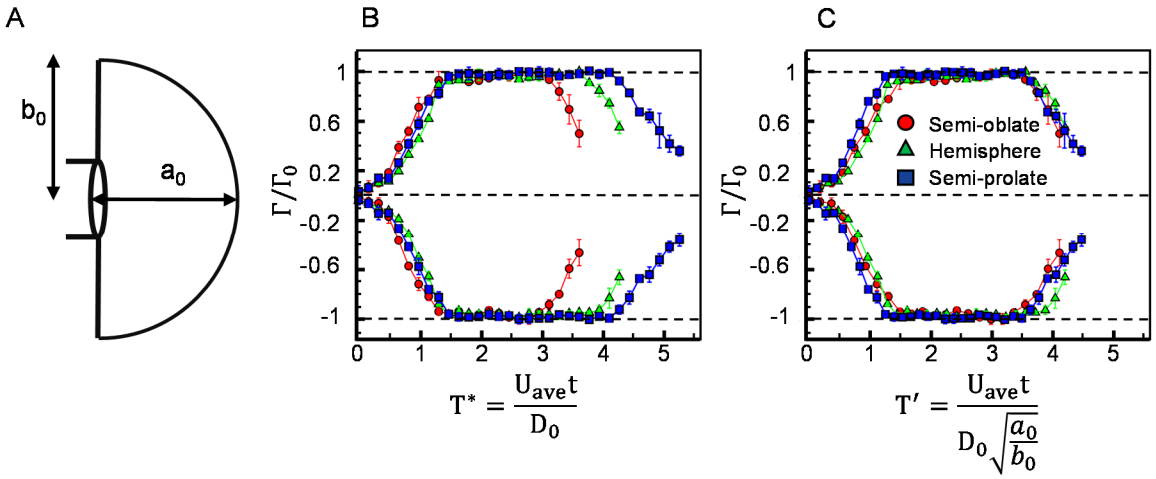

Figure 3-11. Modified vortex formation time based on confinement severity. A) confinement geometry; B) Normalized circulation versus non-dimensional time, $T^* = \frac{U_{ave}t}{D_0}$, at three different confinements for the case with $T = 211$ ms, $AT/DT \sim 1$, and $Re = 1400$. C) Normalized circulation versus modified non-dimensional time, $T^* = \frac{U_{ave}t}{D_0\sqrt{\frac{a_0}{b_0}}}$ for the same condition as B.

As we can see in **Figure 3-11C,** all the circulation plots are decaying at the same time. Therefore, the effects of geometry are embedded in the time scale, which is a valuable result since that can provide us the decay time regardless of confinement shape.

3.3.3. **Effects of AT/DT on vortex ring properties**

The normalized out-of-plane vorticity contours with different levels for the case with $T = 211$ ms, $AT/DT > 1$, and $Re = 1700$ at centered PIV plane ($y/D_0 = 0$) is shown in

Figure 3-12. The only condition difference in **Figure 3-12** compare to **Figure 3-7** was the piston velocity profile in which we increased the AT/DT ratio. Similar time points as **Figure 3-7** was chosen for this figure.

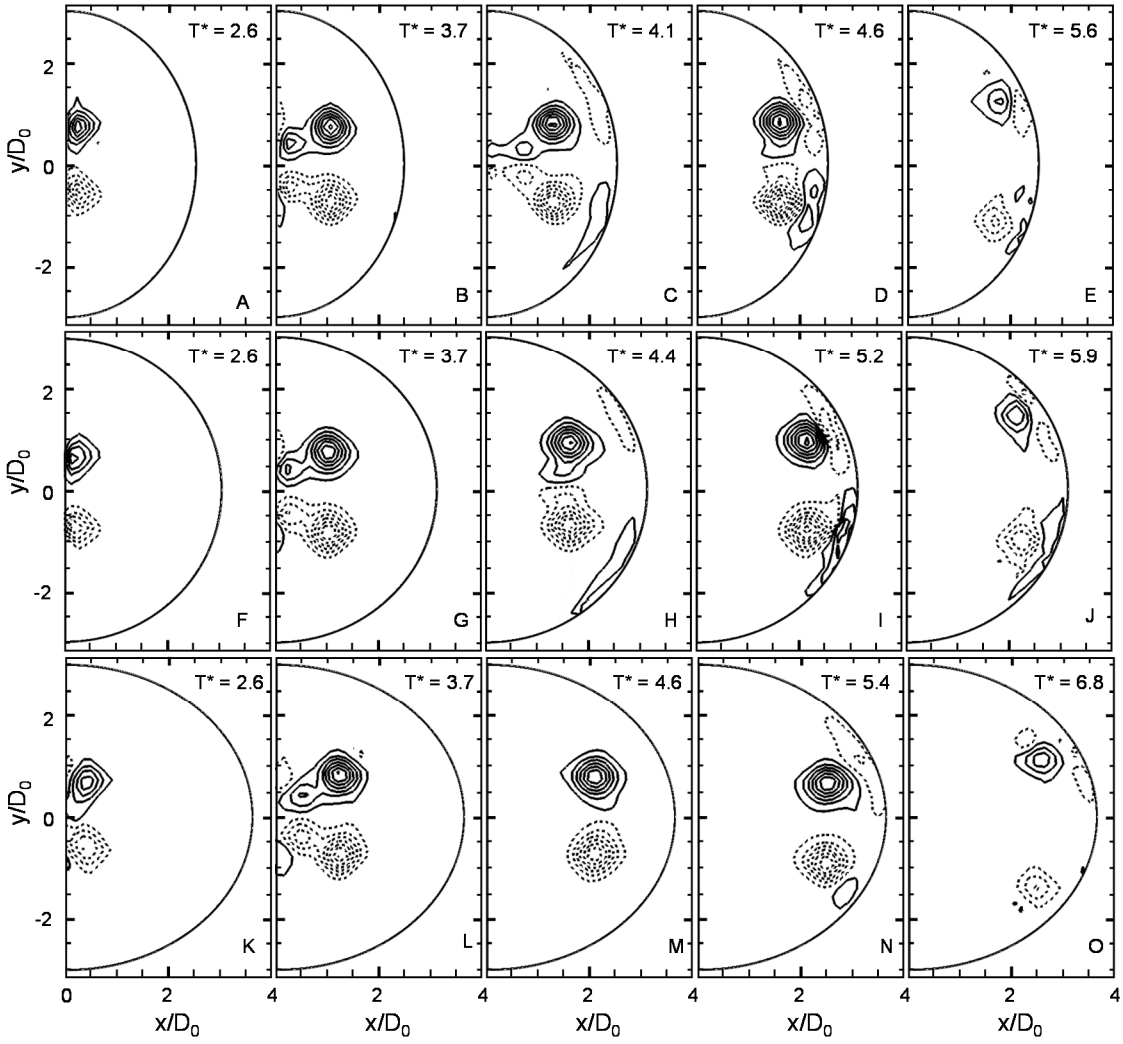

Figure 3-12. Normalized out-of-plane z-vorticity contours at the central plane ($y/D_0 = 0$) at different time points for each silicone model at $T = 211$ ms, $AT/DT > 1$, and $Re = 1700$. a-e) Semi-oblate, f-j) Hemisphere, and k-o) Semi-prolate models. Based on circulation values, five different time points are shown for each model. At a, f, and k, the vortex ring reaches half of the peak circulation ($\Gamma/\Gamma_0 \sim 0.5$). At b, g, and l, the vortex ring pinches off from the trailing jet. At d, i, and n, the vortex ring circulation starts to decay. Time points in c, h, and m occur in between pinch-off and onset of circulation decay, where the circulation has reached a constant peak. The vortex ring breaks down at e, j, and o. Dashed and solid lines represent negative and positive vorticity, respectively. The minimum contour level is 10% of $|\omega^*_{max}| = 7.25$, and the maximum

level is 94% of $|\omega^*_{max}|$. Seven levels are shown with equal 14% increments for both negative and positive vorticities.

The most significant effect of changing the piston velocity profile was associated with vortex pinch-off time and vortex decay time. The peak circulation values were not affected by changing AT/DT ratio.

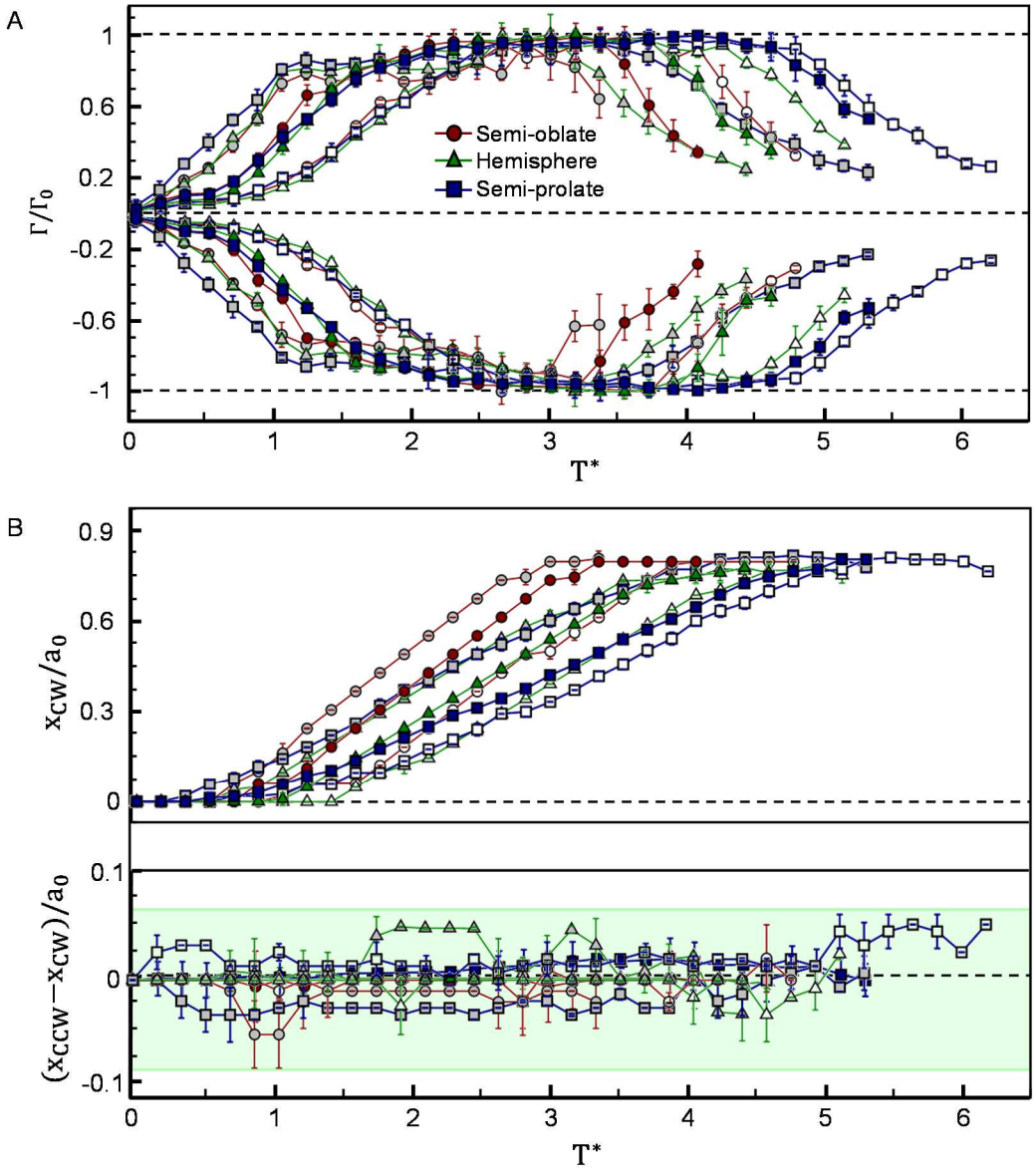

Figure 3-13. Vortex ring circulation and non-dimensional position of CW and CCW vortex cores for T = 211 ms and Re = 1700 at centered PIV plane ($y/D_0 = 0$). A) Normalized circulation versus non-dimensional time. Filled, gray-colored and hollow markers correspond to $AT/DT \sim 1$, $AT/DT < 1$, and $AT/DT > 1$, respectively. B) X-position of CW vortex core (non-

dimensionalized by model major axial length, a_0). The difference between non-dimensional x-position of CW and CCW vortex cores is shown.

3.3.4. **Effects of filling time on vortex ring properties**

The normalized out-of-plane vorticity contours with different levels for the case with $T =$ 110 ms, $AT/DT \sim 1$, and $Re = 1700$ at centered PIV plane ($y/D_0 = 0$) is shown in **Figure 3-14**.

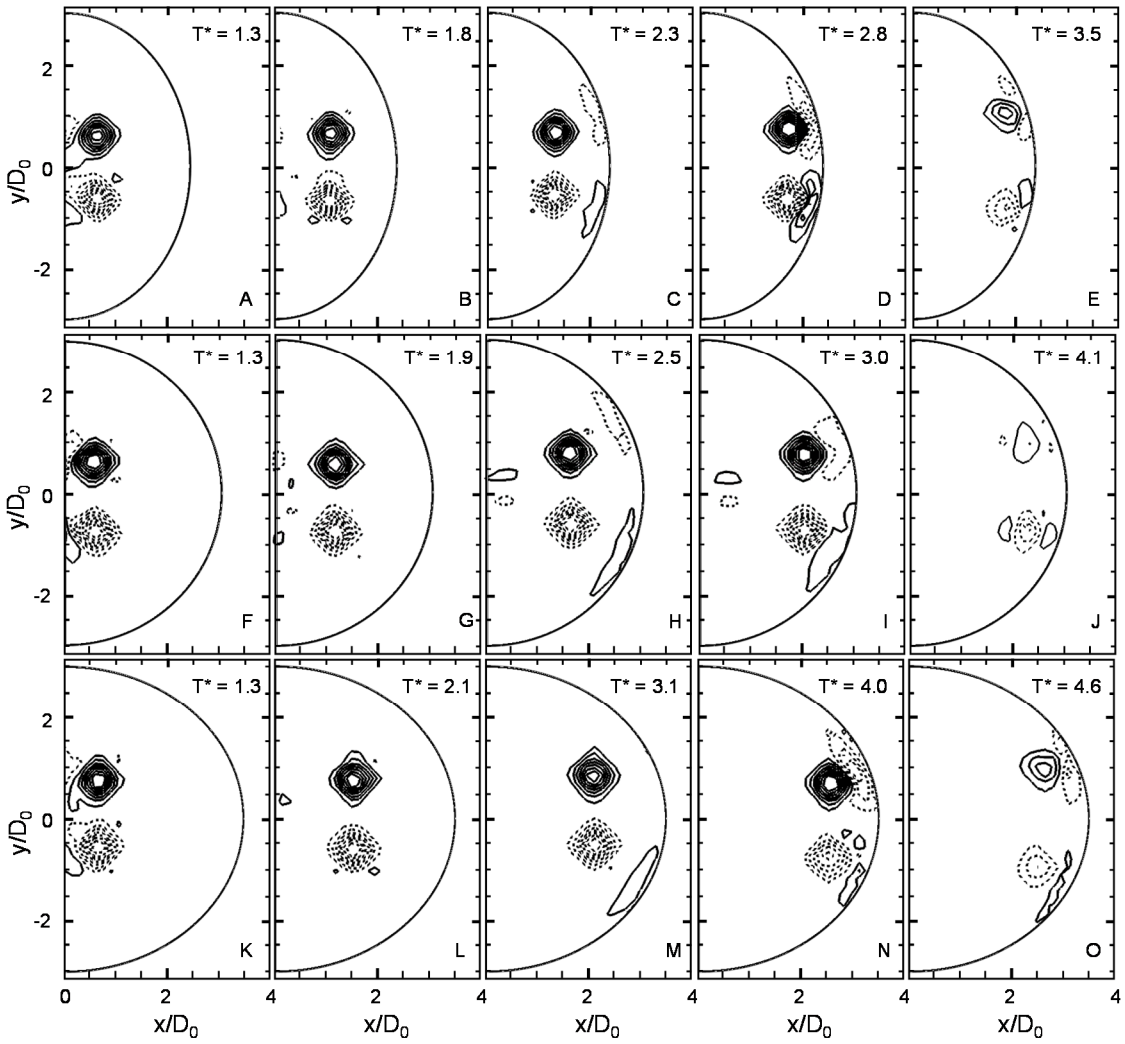

Figure 3-14. Normalized out-of-plane z-vorticity contours at the central plane ($y/D_0 = 0$) at different time points for each silicone model at $T = 110$ ms, $AT/DT \sim 1$, and $Re = 1700$. a-e) Semi-oblate, f-j) Hemisphere, and k-o) Semi-prolate models. Based on circulation values, five different time points are shown for each model. At a, f, and k, the vortex ring reaches peak circulation (onset of pinch-off). At d, i, and n, the vortex ring circulation starts to decay. Time points in b, g, l, c, h, and m occur in between pinch-off and onset of circulation decay, where the circulation has reached a constant peak. The vortex ring breaks down at e, j, and o. Dashed and

solid lines represent negative and positive vorticity, respectively. The minimum contour level is 10% of $|\omega^*_{max}| = 6.69$, and the maximum level is 94% of $|\omega^*_{max}|$. Seven levels are shown with equal 14% increments for both negative and positive vorticities.

The only condition difference in **Figure 3-14** compare to **Figure 3-7** was the filling time in which we shortened the filling time to T = 110 ms. Since the vortex pinched off very early, we associated the first column as the pinch-off time, and the second and third columns were divided equally between the pinch-off time (first column) and decay time (fourth column). And the last column was associated with the onset of the vortex ring breakdown.

Unlike vortex cores in **Figure 3-7**, we did not see a noticeable trailing jet in **Figure 3-14** , and all different levels of vorticies were concentrated in the vortex cores since the filling time was shorter in this case and the primary vortex ring traveled by its own, which is in agreement with previous studies (7, 29, 31). As a result, the vortex cannot carry more particles with itself compare to the case with longer filling time. The peak vorticity magnitude was lower, and vortex ring pinched off earlier compared to longer filling time (T = 211 ms).

The vortex ring circulation strengths for all three different shapes with filling time of $\mathrm{Re} = 1700$, and piston velocity profile of $\mathrm{AT/DT} \sim 1$ at the centered PIV plane were plotted for two different filling times of $\mathrm{T} = 110\ \mathrm{ms}$ (hollow markers), and $\mathrm{T} = 211\ \mathrm{ms}$ (filled markers). For changing the filling time and keeping Reynolds number the same, we have to change the stroke length to diameter ration in a cylinder-piston arrangement. Therefore, decreasing the $\mathrm{L/D_0}$ (filling time) resulted in a decrease in the pinch-off time as we can see in **Figure 3-6**. We quantified the vortex ring diameter from tracking vortex cores and we noticed $\mathrm{D_{VR}/D_0} \sim 1.36, and\ 1.52$ for the cases with $\mathrm{Re} = 1700$ and $\mathrm{AT/DT} \sim 1$ under $\mathrm{T} = 110\ \mathrm{ms}$ and $\mathrm{T} = 211\ \mathrm{ms}$, respectively. By looking at circulation decay portions, we note that the rate of decay was higher in shorter filling time compare to longer filling time (decay rates were quantified in **Figure 3-21**).

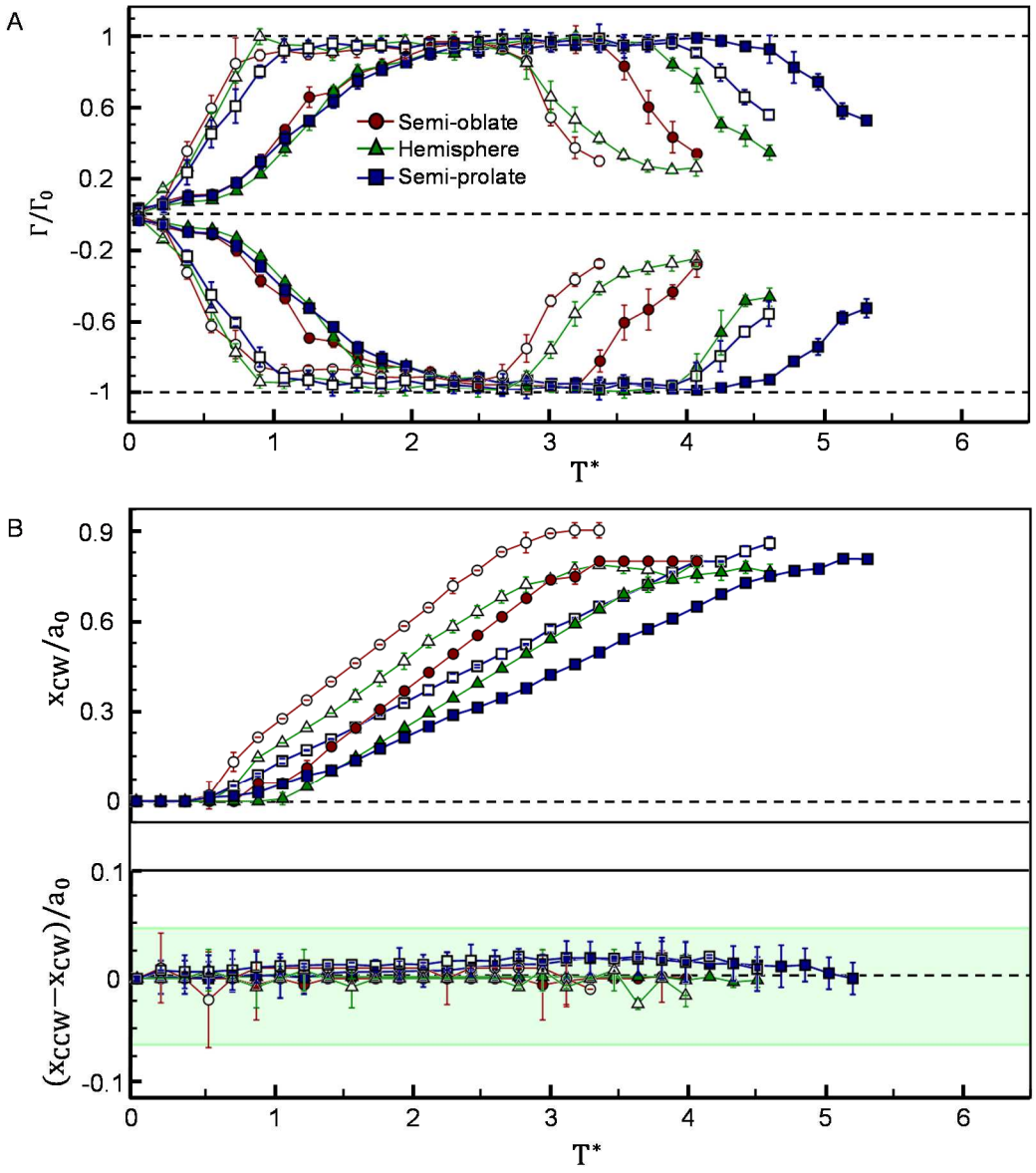

Figure 3-15. Vortex ring circulation and non-dimensional position of CW and CCW vortex cores for AT/DT ~1 and Re = 1700 at centered PIV plane ($y/D_0 = 0$). A) Normalized circulation versus non-dimensional time. Filled and gray-colored markers correspond to T = 211 ms and T = 110 ms, respectively. B) X-position of CW vortex core (non-dimensionalized by model major axial length, a_0). The difference between the non-dimensional x-position of CW and CCW vortex cores are shown.

3.3.5. **Effects of Re on vortex ring properties**

The normalized out-of-plane vorticity contours, ω^*, with different levels for the case with $T = 211$ ms, $AT/DT \sim 1$, and $Re = 2600$ at centered PIV plane ($y/D_0 = 0$) is shown in **Figure 3-16**.

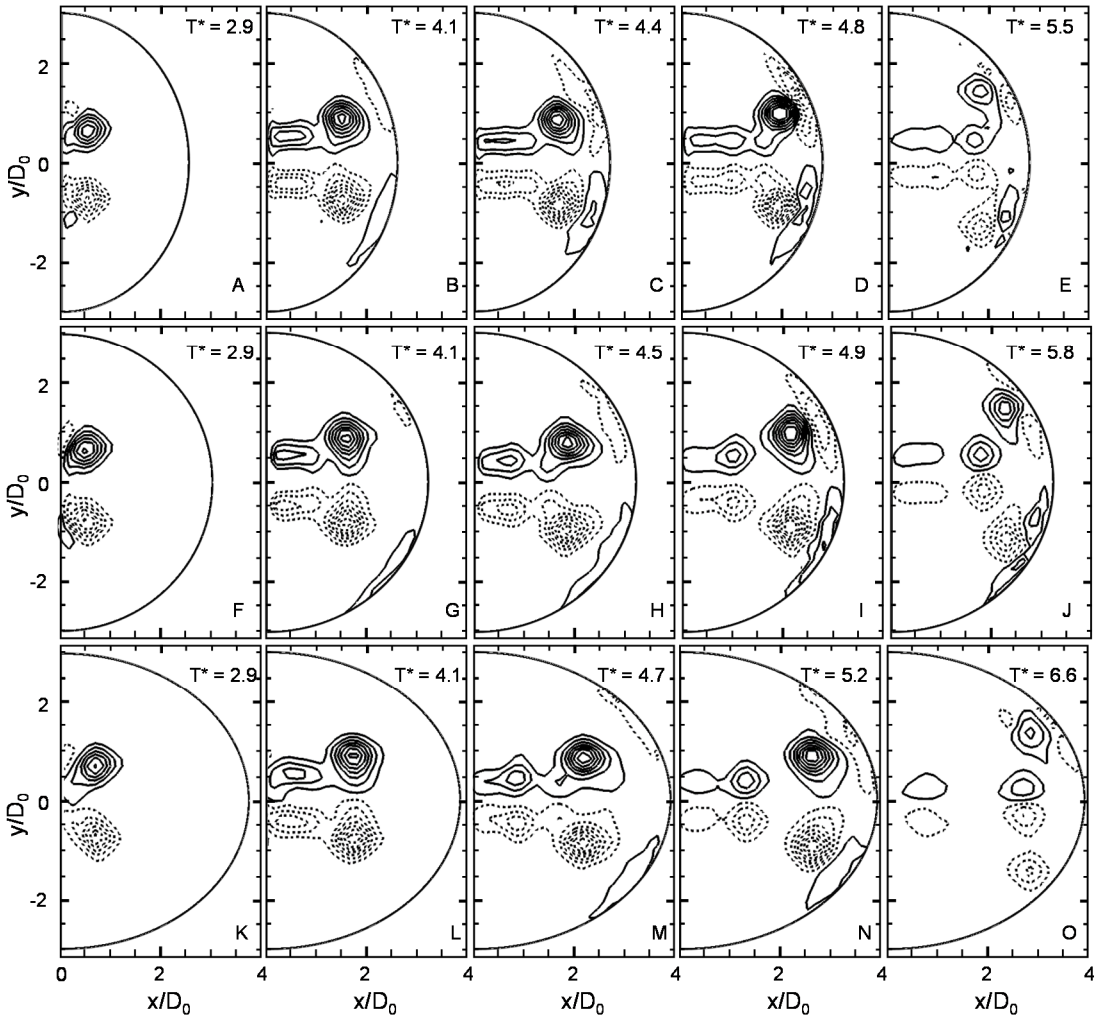

Figure 3-16. Normalized out-of-plane z-vorticity contours at the central plane ($y/D_0 = 0$) at different time points for each silicone model at $T = 211$ ms, $AT/DT \sim 1$, and $Re = 2600$. a-e) Semi-oblate, f-j) Hemisphere, and k-o) Semi-prolate models. Based on circulation values, five different time points are shown for each model. At a, f, and k, the vortex ring reaches half of the peak circulation ($\Gamma/\Gamma_0 \sim 0.5$). At b, g, and l, the vortex ring pinches off from the trailing jet. At d, i, and n, the vortex ring circulation starts to decay. Time points in c, h, and m occur in between pinch-off and onset of circulation decay, where the circulation has reached a constant peak. The vortex ring breaks down at e, j, and o. Dashed and solid lines represent negative and positive vorticity, respectively. The minimum contour level is 10% of $|\omega^*_{max}| = 7.64$, and the maximum

level is 94% of $|\omega^*_{max}|$. Seven levels are shown with equal 14% increments for both negative and positive vorticities.

The only condition difference in **Figure 3-16** compare to **Figure 3-7** was the averaged inflow, which was higher and led to having higher Reynolds numbers. Similar time points as **Figure 3-7** was chosen for this figure.

The pattern of vorticities in time was similar to the ones in **Figure 3-7**. However, few differences were recognized. First, the trailing jet was more elongated and dragged along with the primary vortex ring because of having more inflow. Therefore, the vortex ring had a few following rings with lower strength, which is more visible in the fourth and fifth columns. Second, vortex rings were bigger $D_{VR}/D_0 \sim 1.65$ and consequently decayed faster since it had more interaction with walls. As opposed to **Figure 3-7**, the secondary vortex at the walls was formed earlier (second column at the time of pinch-off), which means the process of decaying started earlier. Third, the pinch-of time had a higher value $T^* = 4.1$ since the stroke length to diameter ratio was higher (7).

The vortex ring circulation strengths for all three different shapes with filling time of $T = 211$ ms, and piston velocity profile of $AT/DT \sim 1$ at the centered PIV plane were plotted for three different Reynolds numbers of $Re = 1400$ (gray-colored markers), $Re = 1700$ (filled markers), and $Re = 1700$ (hollow markers). One of the ways to increase Re in cylinder-piston arrangements is increasing the stroke length as we utilized in this study. Therefore, increasing the L/D_0 (increasing Re) resulted in increasing the pinch-off time as we can see in **Figure 3-17**. We quantified the vortex ring diameter from tracking vortex cores and we noticed $D_{VR}/D_0 \sim 1.41, 1.52, and\ 1.65$ for the cases with $T = 211$ ms, $AT/DT \sim 1$ under of $Re = 1400, 1700, \text{and } 2600$, respectively. Also, Auerbach estimated vortex ring diameter as a function of L/D_0 (for a range of $1 < L/D_0 < 3.3$) as $D_{VR}/D_0 = 1.18(L/D_0)^{1/5}$ (3), which was in good agreement with our results. Therefore, the higher values of vortex ring diameter resulted in earlier circulation decay as shown in **Figure 3-17**.

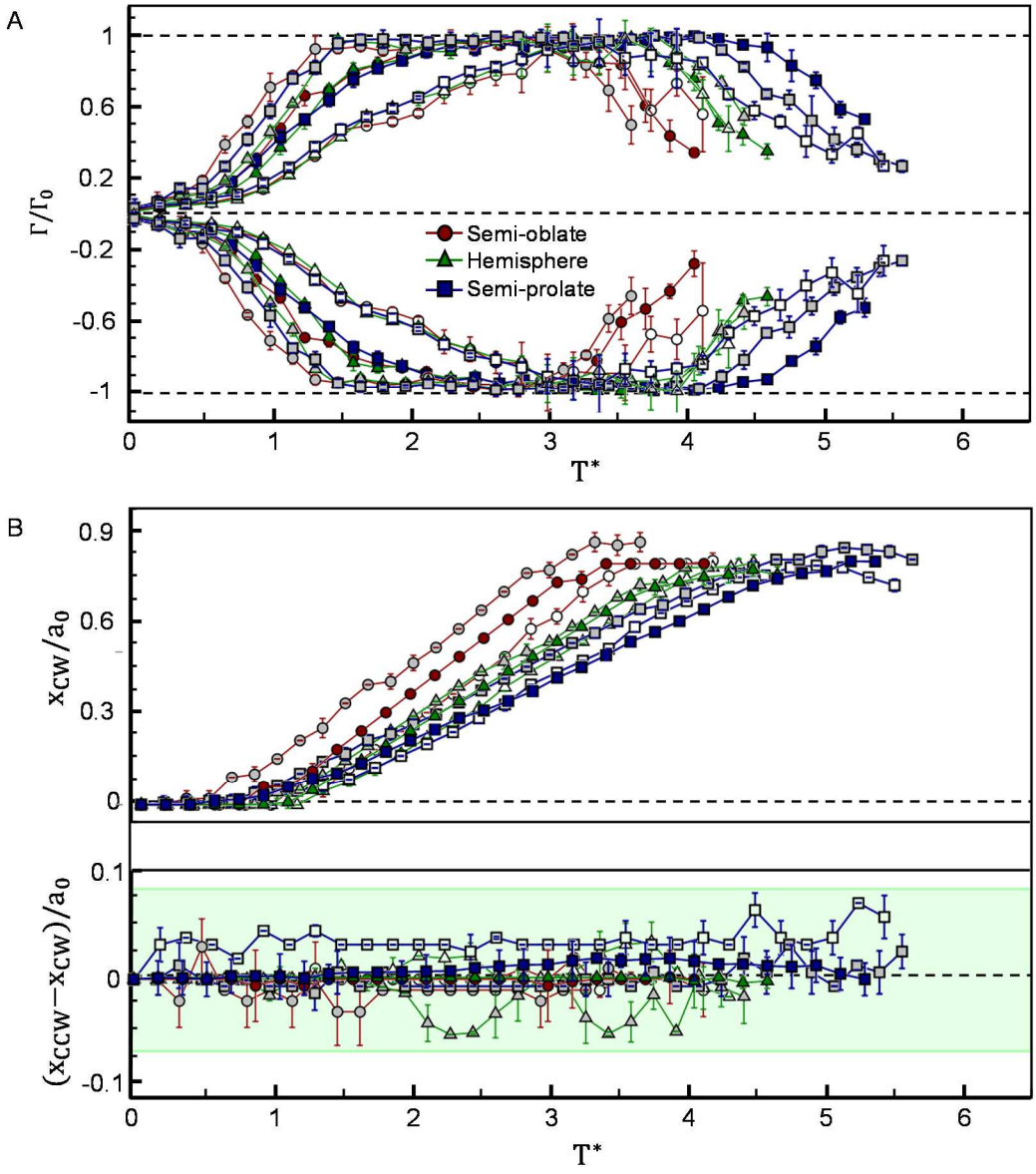

Figure 3-17. Vortex ring circulation and non-dimensional position of CW and CCW vortex cores for $AT/DT \sim 1$ and $T = 211$ ms at centered PIV plane ($y/D_0 = 0$). A) Normalized circulation versus non-dimensional time. Gray-colored, filled, and hollow markers correspond to $Re = 1400$, $Re = 1700$, and $Re = 2600$, respectively. B) X-position of CW vortex core (non-dimensionalized by model major axial length, a_0). The difference between the non-dimensional x-position of CW and CCW vortex cores is shown.

3.3.6. **Peak circulation and pinch-off time**

The dimensional values for peak circulation versus Re at different filling times are shown in **Figure 3-18A** (T = 110 ms) and **Figure 3-18B** (T = 211 ms). Increasing Re resulted in increasing peak circulation; however, the piston velocity profile affected the trend. At the same Re, the circulation value for a vortex ring corresponded to piston velocity profile with smaller deceleration portion (AT/DT>1) became larger rather than those with bigger deceleration portion (AT/DT<1). This difference is more noticeable in **Figure 3-18B** at Re = 2600. By having a gradual acceleration and sudden deceleration of piston velocity profile (AT/DT>1), the vortex ring attained more momentum, and correspondingly higher peak circulation compare to AT/DT<1 piston velocity profile.

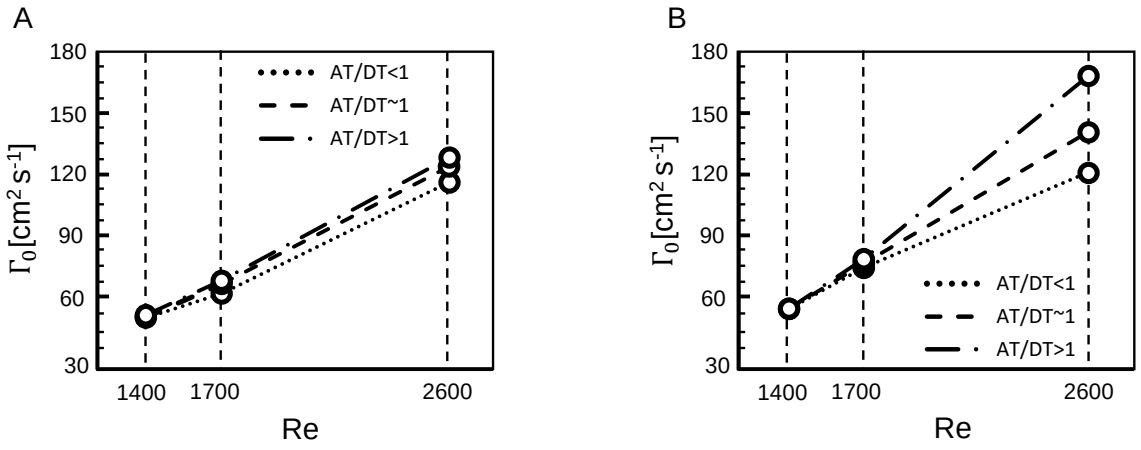

Figure 3-18. Peak circulation versus Re for different AT/DT for the semi-prolate model ($a_0/b_0 = 1.25$) at different filling times. A) $T = 110\ ms$ and B) $T = 211\ ms$.

Non-dimensional peak circulation ($Re_{\Gamma_0} = \Gamma_0/\upsilon$, where υ is kinematic viscosity of water at room temperature) versus modified Reynolds number under the assumption of slug flow ($Re_J = P\frac{U_{ave}L}{2\upsilon}$) was plotted and is shown in **Figure 3-19**. The data from this study were compared with published data from Glezer's study (solid line in **Figure 3-19**) (4).

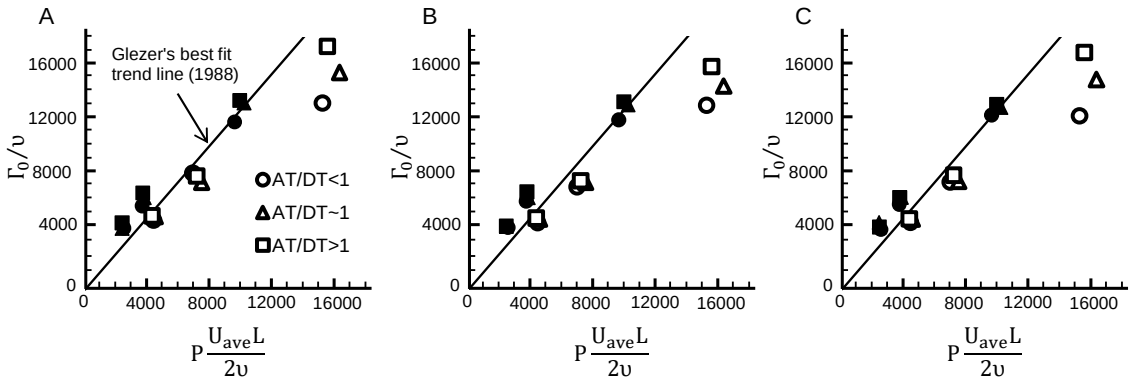

Figure 3-19. Non-dimensional peak circulation (Γ_0/υ) versus modified Re, based on peak circulation in slug flow ($Re_J = P\frac{U_{ave}L}{2\upsilon}$) for different physical models; A) semi-prolate, B) hemisphere, and C) semi-prolate. The solid line was extracted from the best-fit trend line of Glezer's study (1988). Filled and hollow markers correspond to T = 110 ms, and T = 211 ms, respectively.

The trend line fit by Glezer was plotted for data with $Re_J < 10000$. The data points corresponded to T = 110 ms (Re = 1400, 1700, and 2600) and also T = 211 ms (Re = 1400 and 1700) nearly followed Glezer's trend line; however, the higher values of Γ_0/υ corresponded T = 211 ms with Re = 2600 (the rightmost three data points) deviated from the reported linear fit. We also noticed that the Γ_0/υ values versus Re_J was not affected noticeably by changing the types of confinement as we can see in **Figure 3-19**.

By analyzing non-dimensional circulation versus formation time, we assessed the vortex ring pinch-off time and plotted versus theoretical formation number (L/D_0), shown in **Figure 3-20**. It has been reported that pinch-off time grows with increasing L/D_0 until $L/D_0 \sim 4$, and after that, the vortex ring cannot gain more circulation, and the rest of the vorticities will detach from the ring into the trailing jet (5, 7, 10, 20, 29). In this study the maximum observed formation number (pinch-off time) was $T^* = 4.1$, as shown in **Figure 3-20**, which was in agreement with previous studies.

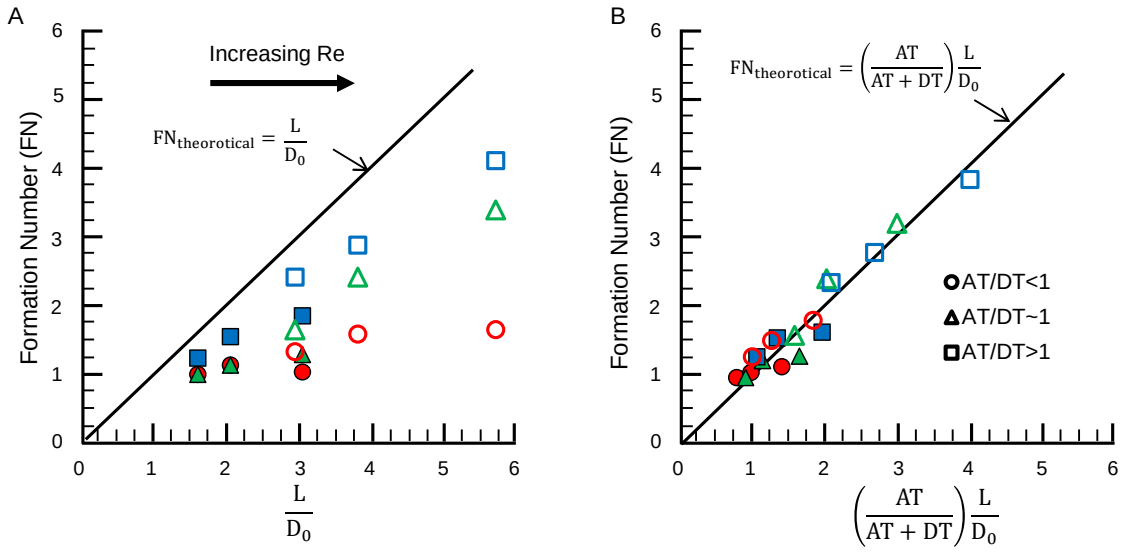

Figure 3-20. Comparison of the calculated formation number (non-dimensional pinch-off time) with theoretical values estimated following $FN = L/D_0$ Gharib et al. (1997). A) Formation number versus theoretical formation number. B) Same data with the presence of the correction factor of $\left(\frac{AT}{AT+DT}\right)$ in the abscissa. Filled and hollow markers corresponded to $T = 110$ ms, and $T = 211$ ms, respectively.

Based on our analysis in this study, the pinch-off time was affected by the piston velocity profile as data points corresponded to AT/DT>1 case showed higher agreement with theoretical formation number as opposed to data points corresponded to AT/DT<1 piston velocity profile. We introduced a modified formation number based on the percentage of acceleration time in the piston velocity profile as $\left(\frac{AT}{AT+DT}\right)\frac{L}{D_0}$. Therefore, in theory for the piston velocity profiles with a sharp deceleration ($AT \gg DT$), we will have $\left(\frac{AT}{AT+DT}\right) \sim 1$ in which the theoretical formation number (7) (L/D_0) will be valid. **Figure 3-20b** shows the same data from **Figure 3-20a** with introducing a correction factor, which described as $\left(\frac{AT}{AT+DT}\right)$, and multiplied in the abscissa. As we can see, all data points were fallen on the forty-five-degree solid line.

3.3.7. **Circulation decay**

The decay process of a vortex ring occurs at the onset of vortex ring circulation decay until the vortex ring breaks down.

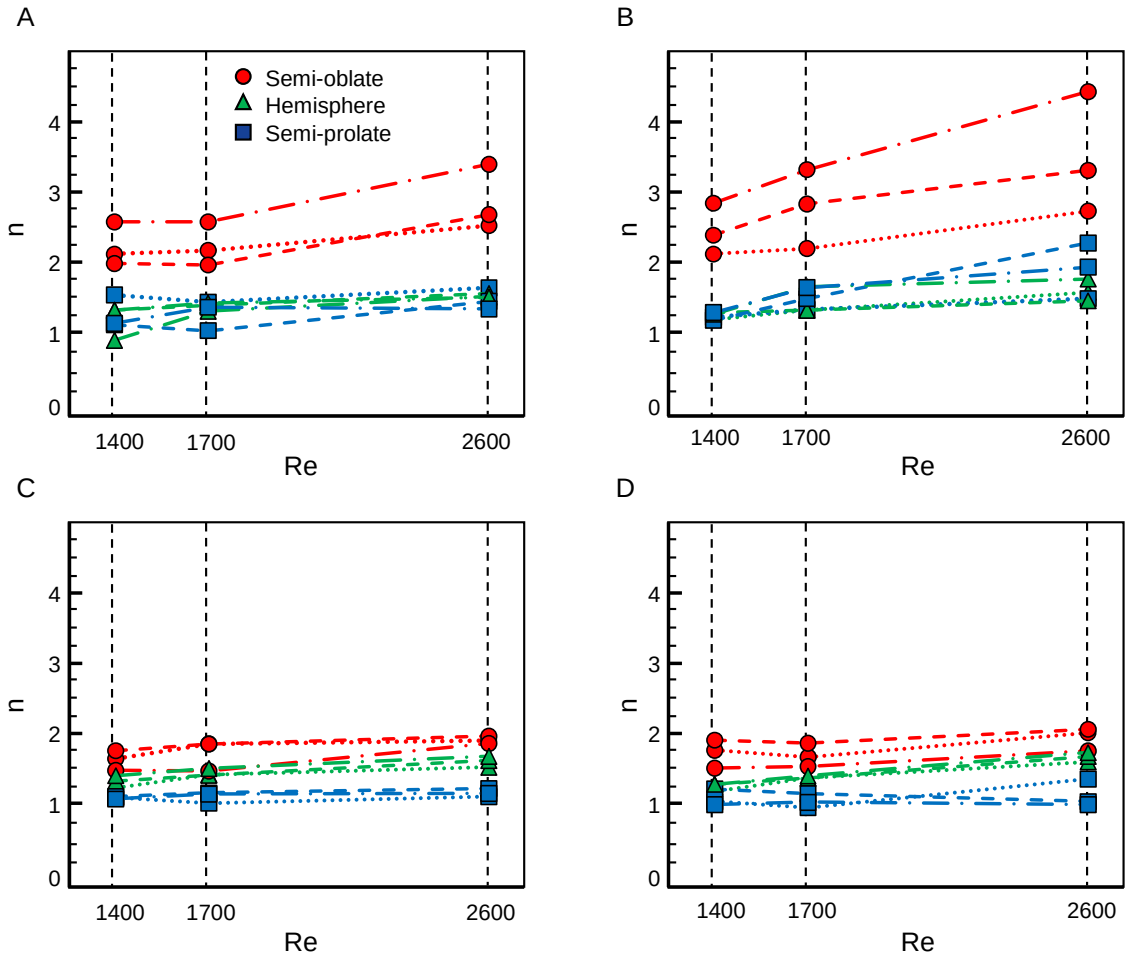

Figure 3-21. Circulation decay rate as a function of Re. The decay rate was obtained from linear regression of plots of $\ln(\Gamma/\Gamma_0)$ versus T^* so that $\Gamma/\Gamma_0 = e^{-nT^*}$, where n is the best-fit linear slope. $\frac{d}{dT^*}(\Gamma/\Gamma_0)$ is the time rate of decay of normalized circulation and this is proportional to n. For the entire test conditions, $0.934 < R^2 < 0.997$ and $1.14 \times 10^{-16} < p - value < 2.32 \times 10^{-7}$. a and b) CCW and CW circulation decay rate at $T = 110$ ms. c and d) CCW and CW circulation decay rate at $T = 211$ ms. AT/DT<1: dotted line; AT/DT~1: dashed line; and AT/DT>1: dash-dotted line.

We plotted the decay portion for all different test conditions and we noticed the decay rate of normalized circulation, Γ/Γ_0, may relate the formation time, T^* exponentially as $\frac{\Gamma}{\Gamma_0} = e^{-nT^*}$.

Therefore, we fitted the best-fit linear slope to the semi-log form of the equation to find the n value as $\frac{d}{dT^*}\left(\frac{\Gamma}{\Gamma_0}\right) = -ne^{-nT^*}$. **Figure 3-21** displays the rate of decay for all test conditions.

The P-values were very low (P-value << 0.05), and $R^2 > 0.93$ for all test conditions in this study, which means we can reject the null hypothesis and we had an acceptable correlation in our curve fitting.

The values of decay rates show a significant difference between shapes for the case with T = 110 ms (a and b) rather than T = 211 ms (c and d) because the vortex ring was isolated from the trailing jet for shorter filling time (T = 110 ms), and we can conclude the effects of axial confinement better. On the other hand, a longer filling time (T = 211 ms) helps the vortex ring to decay slower by feeding more momentum to the leading primary vortex ring.

Now, here is the question that why the circulation decays faster in the more axial-confined domain. We investigated this question by looking at the generated vorticities near the wall and also the pressure field at three different axial-confinement. The vortex very close to the wall, but before decay (T^* = 0.5 before the onset of decay) is plotted for all confinements in **Figure 3-22**. As we can see in **Figure 3-22A-C**, the formed secondary vorticies near the wall are stronger in the more confined domain.

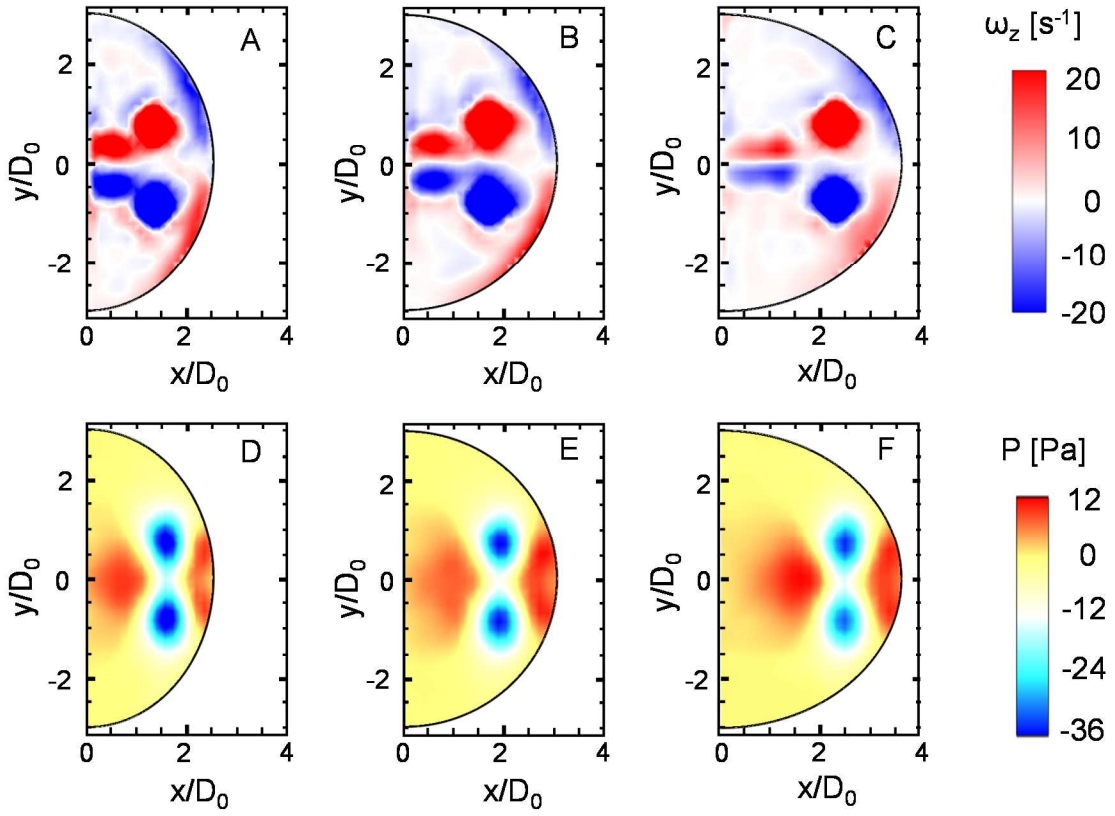

Figure 3-22. Vorticity and pressure fields for different confinement at T = 211 ms, AT/DT ~1, and Re = 1700 at the formation time equal to the onset of decay – 0.5. From A, B, C, and D, E, F corresponds to semi-oblate, hemisphere, and semi-prolate respectively.

The secondary vorticity near the wall has an opposite sign of the primary vortex cores and as a result, by getting the vortex ring closer to the wall, the circulation of the vortex ring will absorb. Therefore, the higher values of vorticity on the walls led to faster vortex ring decay. The tangential pressure gradient sources the formation of secondary vorticies on the wall. On the other hand, the relative volume change in the semi-oblate is higher than the semi-prolate. As a result, the pressure gradient might be higher in the more confined domain, which led to stronger secondary vorticities and finally, a higher rate of circulation decay. Another possibility is the more negative pressure in the vortex cores at the semi-oblate model compared to the semi-prolate, as we can see in **Figure 3-22D-F**. As a result, higher vortex core pressure led to a higher strain of the vortex lines, which forms the vortex ring, and as a result, a higher rate of decay.

3.3.8. **Vortex circulation and circulation decay for active-filling**

The normalized vortex ring circulation in semi-prolate silicon model for all three different AT/DT ratios (AT/DT<1, AT/DT~1, and AT/DT>1) were plotted versus non-dimensional timescale (formation time), $T^* = \frac{U_{ave}t}{D_0}$, at specific Reynolds number (**Figure 3-23**). Positive and negative values of circulation in both figures is corresponded to CCW and CW vortex cores, respectively.

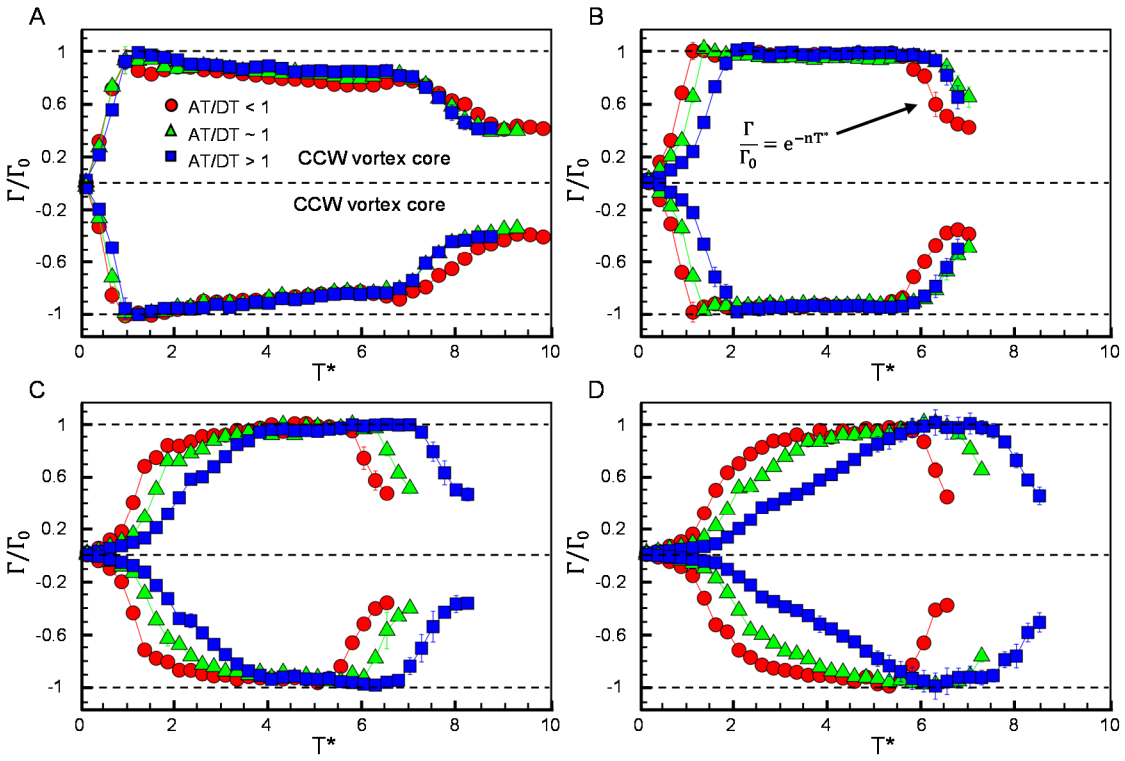

Figure 3-23. Normalized circulation versus non-dimensional time $T^* = \frac{U_{ave}t}{D_0}$ for different AT/DT, and specific Reynolds number. A) Re = 800, B) Re = 1350, C) Re = 2400, and D) Re = 3350.

The trend of normalized circulation shows a difference between the lowest Re (Re = 800) and the rest of the Reynolds numbers. For the cases with Re = 800 (**Figure 3-23A**), the normalized circulation gains the maximum value at the onset of pinch-off, and after that, it decays slowly, and it did not remain constant until the time of decay. A possible reason is the vortex ring is weaker in lower Re, and as a result the vortex ring loses its energy and, consequently, circulation

strength by traveling in a viscose media. Also, the decay rate for the lowest Re case was very gradual compared to the rest of Reynolds number cases (**Figure 3-24**). As a general trend, the pinch-off time was increased by increasing AT/DT and also Reynolds number.

The circulation decays were quantified for all cases (AT/DTs and Re) for both CW and CCW vortex cores and are shown in **Figure 3-24**.

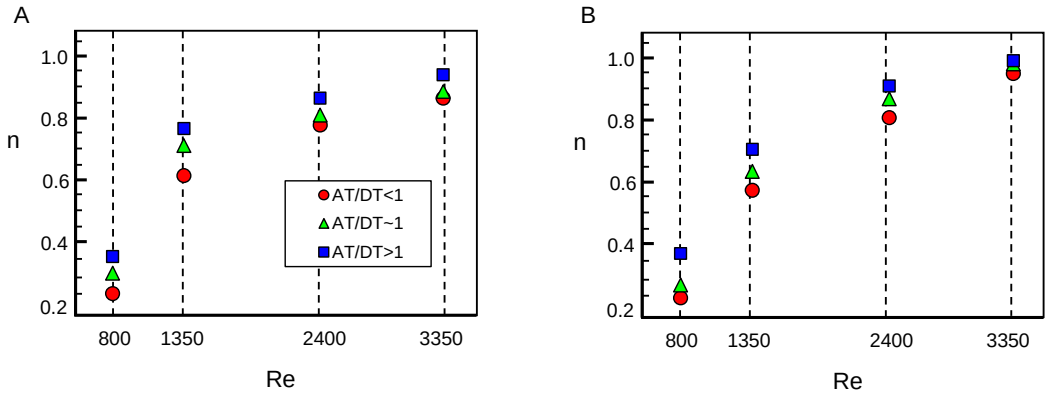

Figure 3-24. Circulation decay rate as a function of Re for different AT/DT ratios. The decay rate was obtained from linear regression of plots of $\ln(\Gamma/\Gamma_0)$ versus T^* so that $\Gamma/\Gamma_0 = e^{-nT^*}$, where n is the best-fit linear slope. $\frac{d}{dT^*}(\Gamma/\Gamma_0)$ is the time rate of decay of normalized circulation and this is proportional to n. For the entire test conditions, $0.956 < R^2 < 0.996$ and $5.41 \times 10^{-15} < p - value < 7.21 \times 10^{-9}$. A, B) CCW and CW circulation decay rates, respectively.

Similar to the study on passive-filling, a similar trend for the decay rate was noticed in active-filling. Increasing the AT/DT ratio and also Reynolds number resulted in a higher rate of decay. Also the trend of circulation was not different between active-filling and passive-filling. As we know, the primary source of running flow into the silicon model was different between active-filling and passive-filling. Therefore, we need to investigate the flow structure more in-depth by calculating and plotting pressure contours for each filling type (active or passive) at different time steps.

3.3.9. **Pressure field for active and passive filling**

The active and passive filling were compared between two similar conditions (at Re = 2500±100), as it is shown in **Figure 3-25**. The centerline velocity and pressure were plotted over time of vortex ring traveling.

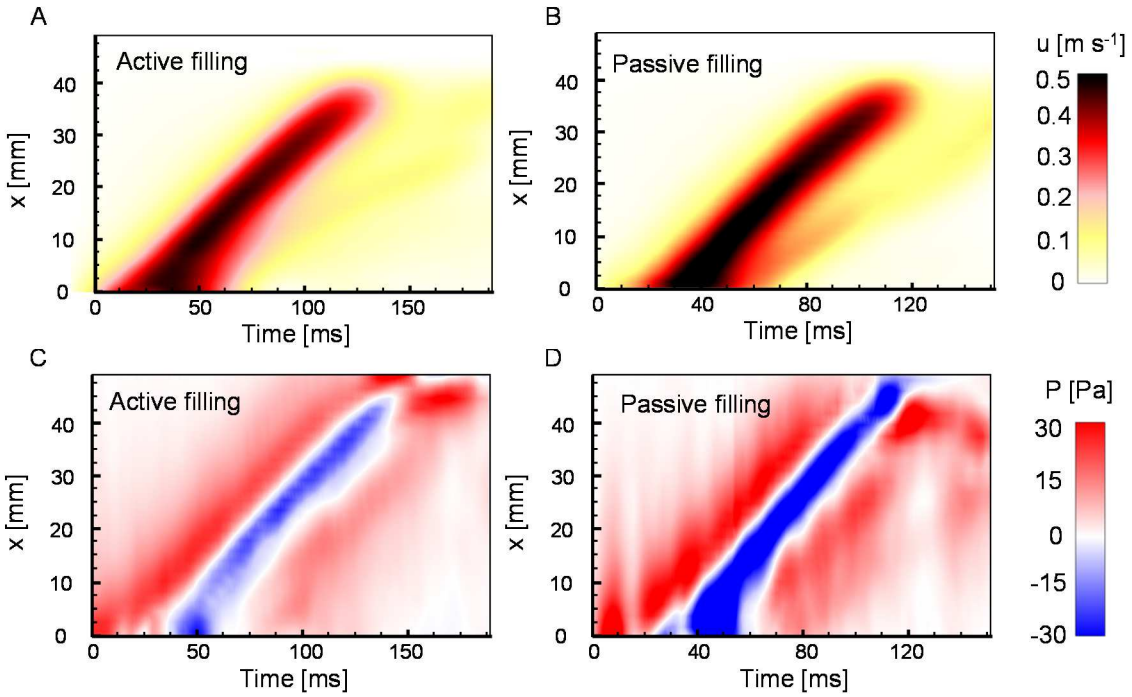

Figure 3-25. The centerline velocity and Pressure values versus time for active and passive filling. A and C) velocity and pressure values at centerline for an active-filling condition corresponds to the case with Re = 2400, and AT/DT~1. B and D) velocity and pressure values at centerline for a passive-filling condition corresponds to the case with Re = 2600, and AT/DT~1, FT = 211, and semi-prolate shape.

As we can see in **Figure 3-25**, the pattern of velocity and pressure at centerline was very similar between active and passive fillings; however, the values are different because of a slight difference in filling time and Reynolds number between the two conditions. We were suspicious about any difference in pressure near the wall between the active and passive filling in the beginning (at $t < 50$ ms); but, the pressure values and also the pattern near the wall (at $x \sim 45$ mm) was not showing a significant difference between the two types of filling.

3.4. Conclusion

This study investigated the properties of the vortex ring within semi-spheroidal confinements. The effects of axial confinement and also flow pattern and Reynolds number on formation and decay of the produced vortex ring were examined in this work. We found that the formation number (pinch-off time) of a vortex ring within a semi-spheroidal domain was nearly unaffected by changing axial confinement. However, by increasing the axial confinement we found: 1) the peak circulation was decreased by up to 10%. Since the same amount of fluid was injected into three different confinement, the pressure inside the most axial-confined domain (semi-prolate) was higher compared to the semi-prolate and hemisphere. As a result, the vortex ring was formed under a higher pressure field, and it gained less circulation strength. 2) The vortex ring reached the end of axial confinement earlier. Therefore, the vortex ring began to decayed more prior in semi-oblate compared to semi-prolate and hemisphere. 3) Since the pressure field is higher in the semi-oblate model, the vortex core had more negative pressure. 4) The vortex ring decay rate was increased. As the vortex ring gets closer to the walls, secondary vorticies are formed in the wall with opposite signs to absorb the strength of the primary vortex ring. The source of the secondary vorticies formation is the tangential pressure gradient on the walls. For the same amount of inflow, the relative change in volume and also pressure magnitude in the more axial-confined domain was higher. Therefore, we can conclude the formed vorticies in the wall were stronger in the semi-oblate case. Another possibility is the higher pressure in the vortex core could lead to a higher strain of the vortex lines. As a result, the vortex ring can break-down faster.

We examined the effects of flow deceleration ratio on vortex ring properties by changing the flow pattern from slow deceleration (AT/DT < 1) to sharp deceleration (AT/DT > 1). The vortex ring was pinched off earlier in AT/DT < 1. As a result, our experimental data on pinch-off time deviated from the theoretical formation number ($\frac{L}{D_0}$). Therefore we introduced a modified

formation number based on acceleration ratio as $\left(\frac{AT}{AT+DT}\right)\frac{L}{D_0}$ and it was correlated with our experimental data. This modified formation time will be similar to Gharib's et al. for the sharp deceleration flow pattern since $\frac{AT}{AT+DT}$ ~ 1 if AT >> DT. The peak circulation and the rate of decay were higher for AT/DT > 1 compared to AT/DT < 1. Increasing the filling time and also Reynolds number led to increasing the pinch-off time since both of them were tied to increasing L/D. Increasing in Reynolds number led to increasing the rate of decay; however, the rate of decay was nearly unaffected across all confinements at large filling time.

This study is the first to examine the vortex ring properties systematically within the semi-spheroidal domain under different flow patterns. The previous work on vortex ring interaction within a confined domain was in radial confinement (20). This work looked at 2D cross-section of the vortex ring at three parallel planes. However, to further understanding the vortex ring behavior it is better to conduct a 3D PIV to better understanding the vortex ring properties.

Funding. This work was supported by a Carroll M. Leonard Faculty Fellowship to Arvind Santhanakrishnan.

3.5. References

1. Didden, N. (1979). On the formation of vortex rings: rolling-up and production of circulation. *Zeitschrift für angewandte Mathematik und Physik ZAMP*, *30*(1), 101-116.

2. Maxworthy, T. (1977). Some experimental studies of vortex rings. *Journal of Fluid Mechanics*, *81*(3), 465-495.

3. Auerbach, D. (1988). Some open questions on the flow of circular vortex rings. *Fluid Dynamics Research*, *3*(1-4), 209.

4. Glezer, A. (1988). The formation of vortex rings. *The Physics of fluids*, *31*(12), 3532-3542.

5. Weigand, A., & Gharib, M. (1997). On the evolution of laminar vortex rings. *Experiments in Fluids*, *22*(6), 447.

6. Benjamin, T. B. (1976). The alliance of practical and analytical insights into the nonlinear problems of fluid mechanics. In *Applications of methods of functional analysis to problems in mechanics* (pp. 8-29). Springer, Berlin, Heidelberg.

7. Gharib, M., Rambod, E., & Shariff, K. (1998). A universal time scale for vortex ring formation. *Journal of Fluid Mechanics*, *360*, 121-140.

8. Linden, P. F., & Turner, J. S. (2004). 'Optimal'vortex rings and aquatic propulsion mechanisms. *Proceedings of the Royal Society of London. Series B: Biological Sciences*, *271*(1539), 647-653.

9. Bartol, I. K., Krueger, P. S., Stewart, W. J., & Thompson, J. T. (2009). Pulsed jet dynamics of squid hatchlings at intermediate Reynolds numbers. *Journal of Experimental Biology*, *212*(10), 1506-1518.

10. Gharib, M., Rambod, E., Kheradvar, A., Sahn, D. J., & Dabiri, J. O. (2006). Optimal vortex formation as an index of cardiac health. *Proceedings of the National Academy of Sciences*, *103*(16), 6305-6308.

11. Dabiri, J. O., & Gharib, M. (2005). The role of optimal vortex formation in biological fluid transport. *Proceedings of the Royal Society B: Biological Sciences*, *272*(1572), 1557-1560.

12. Kheradvar, A., Rickers, C., Morisawa, D., Kim, M., Hong, G. R., & Pedrizzetti, G. (2019). Diagnostic and prognostic significance of cardiovascular vortex formation. *Journal of cardiology*.

13. Pedrizzetti, G., La Canna, G., Alfieri, O., & Tonti, G. (2014). The vortex—an early predictor of cardiovascular outcome?. *Nature Reviews Cardiology*, *11*(9), 545.

14. Krueger, P. S., Dabiri, J. O., & Gharib, M. (2006). The formation number of vortex rings formed in uniform background co-flow. *Journal of Fluid Mechanics*, *556*, 147-166.

15. Dabiri, J. O., & Gharib, M. (2004). Delay of vortex ring pinchoff by an imposed bulk counterflow. *Physics of Fluids*, *16*(4), L28-L30.

16. Mohseni, K., Ran, H., & Colonius, T. (2001). Numerical experiments on vortex ring formation. *Journal of Fluid Mechanics*, *430*, 267-282.

17. Walker, J. D. A., Smith, C. R., Cerra, A. W., & Doligalski, T. L. (1987). The impact of a vortex ring on a wall. *Journal of Fluid Mechanics*, *181*, 99-140.

18. Lim, T. T. (1989). An experimental study of a vortex ring interacting with an inclined wall. *Experiments in Fluids*, *7*(7), 453-463.

19. Chang, T. Y., Hertzberg, J. R., & Kerr, R. M. (1997). Three-dimensional vortex/wall interaction: Entrainment in numerical simulation and experiment. *Physics of Fluids*, *9*(1), 57-66.

20. Stewart, K. C., Niebel, C. L., Jung, S., & Vlachos, P. P. (2012). The decay of confined vortex rings. *Experiments in Fluids*, *53*(1), 163-171.

21. Stewart, K. C., & Vlachos, P. P. (2012). Vortex rings in radially confined domains. *Experiments in fluids*, *53*(4), 1033-1044.

22. Danaila, I., Kaplanski, F., & Sazhin, S. (2015). Modelling of confined vortex rings. *Journal of Fluid Mechanics*, *774*, 267-297.

23. Courtois, M., Kovács Jr, S. J., & Ludbrook, P. A. (1988). Transmitral pressure-flow velocity relation. Importance of regional pressure gradients in the left ventricle during diastole. *Circulation*, *78*(3), 661-671.

24. Lisauskas, J. B., Singh, J., Bowman, A. W., & Kovács, S. J. (2001). Chamber properties from transmitral flow: prediction of average and passive left ventricular diastolic stiffness. *Journal of Applied Physiology*, *91*(1), 154-162.

25. Stewart, K. C. (2011). *Hydrodynamics of Cardiac Diastole* (Doctoral dissertation, Virginia Tech).

26. Krittian, S., Janoske, U., Oertel, H., & Böhlke, T. (2010). Partitioned fluid–solid coupling for cardiovascular blood flow. *Annals of biomedical engineering*, *38*(4), 1426-1441.

27. Charonko, J. J., Kumar, R., Stewart, K., Little, W. C., & Vlachos, P. P. (2013). Vortices formed on the mitral valve tips aid normal left ventricular filling. *Annals of biomedical engineering*, *41*(5), 1049-1061.

28. Okafor, I. U., Santhanakrishnan, A., Chaffins, B. D., Mirabella, L., Oshinski, J. N., & Yoganathan, A. P. (2015). Cardiovascular magnetic resonance compatible physical model of the left ventricle for multi-modality characterization of wall motion and hemodynamics. *Journal of Cardiovascular Magnetic Resonance*, *17*(1), 51.

29. Dabiri, J. O., & Gharib, M. (2004). Fluid entrainment by isolated vortex rings. *Journal of fluid mechanics*, *511*, 311-331.

30. Dabiri, J. O., Bose, S., Gemmell, B. J., Colin, S. P., & Costello, J. H. (2014). An algorithm to estimate unsteady and quasi-steady pressure fields from velocity field measurements. *Journal of Experimental Biology*, *217*(3), 331-336.

31. O'Farrell, C., & Dabiri, J. O. (2014). Pinch-off of non-axisymmetric vortex rings. *Journal of Fluid Mechanics*, *740*, 61-96.

CHAPTER IV

4. DIASTOLIC VORTEX ALTERATION WITH REDUCING LEFT VENTRICULAR VOLUME: AN IN VITRO STUDY

Abstract: Despite the large number of studies of intraventricular filling dynamics for potential clinical applications, little is known as to how the diastolic vortex ring properties are altered with reduction in internal volume of the cardiac left ventricle (LV). The latter is of particular relevance in LV diastolic dysfunction (LVDD), where pathological remodeling can lead to diminished LV internal volume (concentric LV hypertrophy). Congenital diseases such as hypertrophic cardiomyopathy (HCM) can also decrease LV internal volume. We hypothesized that peak circulation and the rate of decay of circulation of the diastolic vortex would be altered with reducing end diastolic volume (EDV) due to increasing confinement. We tested this hypothesis on physical models of normal LV and HCM geometries, under identical prescribed inflow profiles and for multiple EDVs, using time-resolved particle image velocimetry measurements on a left heart simulator. Formation and pinch-off of the vortex ring were nearly unaffected with changes to geometry and EDV. Pinch-off occurred well before the end of early filling in all test conditions. Peak circulation of the vortex core near the LV septal wall increased with lowering EDV in both models. The rate of decay of normalized circulation (n) in dimensionless formation time (T^*) increased with decreasing EDV. n was found to scale nearly identically across all EDVs

in the normal LV model, when using a modified version of T^* that included average LV cross-sectional area and EDV. Collectively, our results show that LV shape and internal volume play a critical role in diastolic vortex ring dynamics.

Keywords: left heart simulator, intraventricular flow, diastolic vortex, end diastolic volume, hypertrophic cardiomyopathy

4.1. Introduction

A large number of studies have examined the fluid dynamics of filling (diastole) in the human cardiac left ventricle (LV) (1-17). Vortex ring formation is observed as blood enters the LV from the left atrium via the mitral valve. Diastolic filling vortex properties have been observed to change between normal cardiac function and impaired pumping (LV systolic dysfunction) (2,4,9), as well as in impaired filling or LV diastolic dysfunction (LVDD) (5,7,18-20). Pathological remodeling of the LV can occur in LVDD on account of pressure overload. The LV wall subsequently thickens with simultaneous reduction in LV internal volume, leading to concentric LV hypertrophy (LVH) (21). In addition to factors such as hypertension and coronary artery disease, congenital diseases such as hypertrophic cardiomyopathy (HCM) can also result in LVDD with reduction in LV internal volume (22). Recent evidence shows that healthy hearts show strong coupling between the volumes of the filling vortex ring and the LV (15), suggesting an elevated importance of LV shape. However, a mechanistic understanding of how diastolic vortex properties are altered with reduction in internal volume of the LV (as in concentric LVH) remains unavailable. As multiple pathological conditions resulting in LVDD are typically accompanied by reduced internal volume of the LV, such a fundamental understanding can help in determining whether changes in diastolic vortex properties can be potentially useful in monitoring progression of LVDD.

The vortex formation time (VFT) is the most commonly evaluated index (23-25) based on the diastolic vortex. VFT signifies the dimensionless time instant when a vortex ring stops growing, reaching both maximum volume and strength (circulation), and pinches-off from the inflow jet. VFT was originally formulated by considering the propagation of a vortex ring in an unconfined (semi-infinite) surrounding domain (26). The entire duration of early filling (E-wave) portion of diastole is typically used in cardiac VFT calculation (2). However, a recent study employing clinical data (27) showed that vortex ring pinch-off occurs well *before* the completion of E-wave, questioning the appropriateness of VFT definition. This study (27) also observed that VFT, when re-calculated by only accounting for pinch-off time and not the entire E-wave, was *not* affected by diastolic impairment. The main reason for this discrepancy was noted to be the assumption of an unconfined domain in VFT formulation (27,28). In LVDD, reduction in LV internal volume (due to LVH and/or impaired LV relaxation) would further increase the confinement imposed by the LV cavity on the filling vortex. A previous study (29) showed that confined vortex rings experience an increased rate of decay of circulation when compared to vortex rings that propagate in an unconfined domain. Collectively, these findings suggest that confinement from the LV cavity needs to be considered when examining filling vortex dynamics in LVDD. Excluding dilated cardiomyopathy where systolic dysfunction with eccentric LVH are observed (increased LV internal volume) (9), no study has systematically examined how decreasing LV internal volume impacts circulation of the diastolic vortex.

The purpose of this study was to comparatively examine how diastolic vortex properties are altered with reduction in LV internal volume. We hypothesized that increasing confinement imposed on the diastolic vortex ring, by decreasing LV internal volume, would alter peak circulation and increase the rate of circulation decay following pinch-off. We used an in vitro approach and examined diastolic vortex dynamics within a flexible-walled anatomical LV physical model (denoted hereafter as *normal LV*) that was incorporated into a left heart simulator

with a pulsatile flow circuit. As a representative example of asymmetric LV wall thickening, we also examined filling vortex dynamics within a HCM physical model fitted into our left heart simulator. End diastolic volume (EDV) was changed iteratively between tests by adjusting the initial volume of each model, which in turn altered the time-variation of LV volume during the cardiac cycle. All flow circuit variables, including most importantly the inflow rate profile, were maintained constant while varying the physical model geometry and EDV. Our results showed that vortex ring formation and pinch-off process were unaffected by changes in the EDV and physical model geometry. In the normal LV model, circulation of the vortex core closer to the LV outflow tract (LVOT) increased with reducing EDV. Peak circulation of the filling vortex core proximal to LVOT was lower in the HCM model. Finally, the rate of decay of circulation decreased with increasing EDV in both geometries. These findings highlight the need to consider LV internal volume when evaluating diastolic vortex properties in LVDD with LV wall thickening.

4.2. Experimental Methods

4.2.1. **Physical modeling**

Two different physical model geometries were considered in this study: 1) anatomical normal LV model that has been used in previous studies (**Figure 4-1A**) (30-32); and 2) obstructive HCM geometry (**Figure 4-1B**).

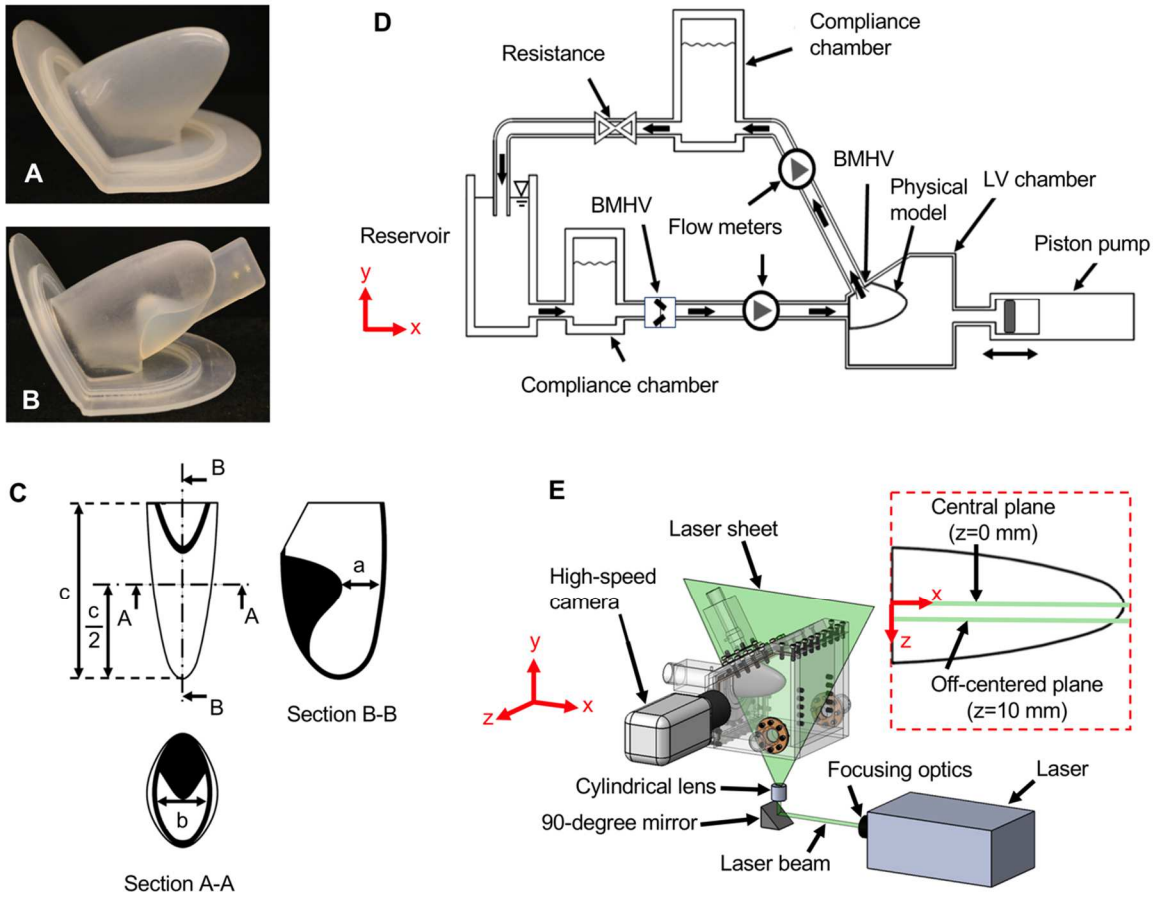

Figure 4-1. Physical models and left heart simulator used in this study. Flexible-walled, optically clear physical models of: (A) normal LV and (B) HCM geometries were individually tested in a pulsatile flow circuit at different EDVs specified in **Table 4-1**. LVSI of each model geometry was calculated using equation **Error! Reference source not found.**Eq. 4-1) based on dimensions illustrated in (C). Schematic diagrams of: (D) left heart simulator and flow circuit; and (E) experimental setup for quantitative flow visualization using 2D TR-PIV. TR-PIV data were acquired at the following two parallel x-y planes: z=0 mm (central axis of model) and z=10 mm. LVSI=left ventricle sphericity index; BMHV=bi-leaflet mechanical heart valve.

The HCM geometry was based on previously published data obtained from HCM patients with septal wall thickening (33,34). For geometric characterization of model shape, LV sphericity index (LVSI) was calculated using the relation:

$$\mathrm{LVSI} = \left(\frac{a+b}{2}\right)/c \qquad \text{Eq. 4-1}$$

where a, b and c are the model dimensions along axes running from: septal wall to lateral wall, anterior to inferior wall, and apex to base of LV, respectively (**Error! Reference source not found.**C). LVSI of normal LV and HCM models were 0.42 and 0.28, respectively (**Table 4-1**).

Table 4-1. Mechanical and geometric characteristics of physical models and test conditions examined in this study. Passive wall stiffness of a physical model was measured experimentally as follows: each model was filled with a known volume of water and the static pressure inside the model was measured using an absolute pressure transducer. Linear regression of pressure-volume data was performed, and wall stiffness was calculated from the slope of the line of best-fit (R^2=0.99 in both models). The acrylic chamber surrounding the model was filled with water and open to atmosphere during stiffness measurements. LV sphericity index (LVSI) was calculated using equation Error! Reference source not found.) based on the dimensions illustrated in **Figure 4-1**. Both normal LV and HCM models had the same wall thickness (1.59 mm) and were case from the same type of silicone (shore hardness: 40A). Finally, physiologically relevant range of EDVs are indicated for each test condition.

Physical model	Test conditions	EDV range [ml]
Normal LV (LVSI = 0.42) Stiffness = 2.2 mm Hg/ml	Normal LV $_{\text{Low EDV}}$	100-120
	Normal LV $_{\text{Normal EDV}}$	120-130
	Normal LV $_{\text{High EDV}}$	160-180
HCM (LVSI = 0.28) Stiffness = 2.9 mm Hg/ml	HCM $_{\text{Low EDV}}$ (35)	105-130
	HCM $_{\text{Normal EDV}}$ (35)	130-155

Cast urethane process was used to fabricate molds of the normal LV and HCM geometries. Elastomeric silicone was injected in the molds to produce flexible-walled castings. Silicone was selected for obtaining optical clarity in the castings, necessary for flow visualization. Wall thickness (1.59 mm) and silicone shore hardness (40A) were maintained approximately the same between the normal LV and HCM physical models. The HCM model had to be anchored at its apex using a strip of additional material (**Figure 4-1B**), as otherwise the HCM model moved upward-downward unlike the normal LV model (due to asymmetric stiffness from the

hypertrophied portion). Anchoring of the HCM model resulted in identical wall motion as the normal LV model that was unanchored at its apex.

Though the shore hardness of the silicone used in casting the normal LV and HCM models was identical (40A), the finished physical models were expected to be non-identical in stiffness. The passive stiffness of each physical model was determined from experimental pressure and volume recordings. Each model was fitted inside an acrylic box that was filled with water and open to the atmosphere. The model was internally filled with a known volume of water. An absolute pressure transducer (Utah Medical Products Inc., Midvale, UT, USA) was used to measure pressure inside the model. LV pressure was recorded for successive volume increments of 10 ml. Linear regression of the pressure-volume data was performed and passive wall stiffness was obtained as the slope of the line of best-fit. The HCM model was found to be marginally stiffer than the normal LV model (**Table 4-1**), likely on account of the obstructive portion with thicker wall.

.

4.2.2. **Left heart simulator**

A left heart simulator with a recirculating flow loop was used to prescribe physiologically relevant inflow within each physical model (**Figure 4-1D**). Each physical model was placed in a clear acrylic chamber that was filled with 35% by volume of glycerin solution in water. This solution was used to mimic the kinematic viscosity of blood at 37 °C (3.5 cSt) and closely matched the refractive index of acrylic. A programmable piston pump (ViVitro Systems Inc., Victoria, Canada) was used to generate physical model wall motion by imparting pressure fluctuations in the fluid between interior of the acrylic chamber and the external wall of the model. Deformation of the wall generated flow into and out of the physical model. Two bi-leaflet mechanical heart valves (BMHV), with diameters of 32 mm (inflow) and 25 mm (outflow), were used to ensure unidirectional flow through the model. Systemic compliance and resistance elements were used in the flow loop to obtain physiological mitral inflow profile and mean aortic

pressure of approximately 100 mm Hg between all test conditions (3 EDVs for normal LV and 2 EDVs for HCM). The outflow BMHV was mounted at the aortic annulus. The inflow BMHV was placed upstream of the mitral annulus to not differentially impact leaflet motion between test conditions. Three pressure transducers (Utah Medical Products Inc., Midvale, UT) were used to measure the pressures at multiple points in the flow loop (chamber, aortic, and LV pressures). Two ultrasonic flowmeters (Transonic Systems Inc., Ithaca, NY) were used to measure instantaneous outflow and inflow rates.

4.2.3. **Experimental protocols**

The input voltage versus time waveform to the piston pump, systemic resistance and compliance were tuned with the normal LV model to obtain physiologically relevant: EDV, inflow rate variation in time, and mean aortic pressure. The EDV was indirectly adjusted by changing the initial volume of the physical model before turning the pump on. Hemodynamic measurements (pressure and flow rates) and flow visualization were conducted for normal EDV. The initial volume of the normal LV model was then varied to obtain 2 different EDVs (1 lesser than and 1 greater than normal EDV), and identical set of hemodynamics and flow visualization measurements were conducted. The same sequence of steps was then repeated for the HCM physical model. Systemic compliance and resistance elements were not differentially adjusted across all the test conditions. Physiologically relevant ranges of EDVs for each geometry is provided in **Table 4-1** (EDV range for HCM models were obtained from a published study (35)).

To facilitate comparison of the diastolic vortex across model geometry and EDV, we maintained inflow profile to be nearly identical across all test conditions (**Figure 4-2**). Variation of EDV, achieved by changing initial volume of a physical model, did not alter time-varying inflow rate. In addition to resistance and compliance levels, the reservoir head, piston pump parameters (voltage waveform, stroke amplitude, stroke frequency), and difference between static pressures of fluid within the chamber and within the model ($P_{chamber} - P_{model}$) at rest were unchanged

between all test conditions. To characterize the inflow, the Reynolds number was defined using the relation:

$$Re = \frac{Q_{\text{in,max}}}{\frac{\pi}{4}\nu\, D_{\text{MV}}} \qquad \text{Eq. 4-2}$$

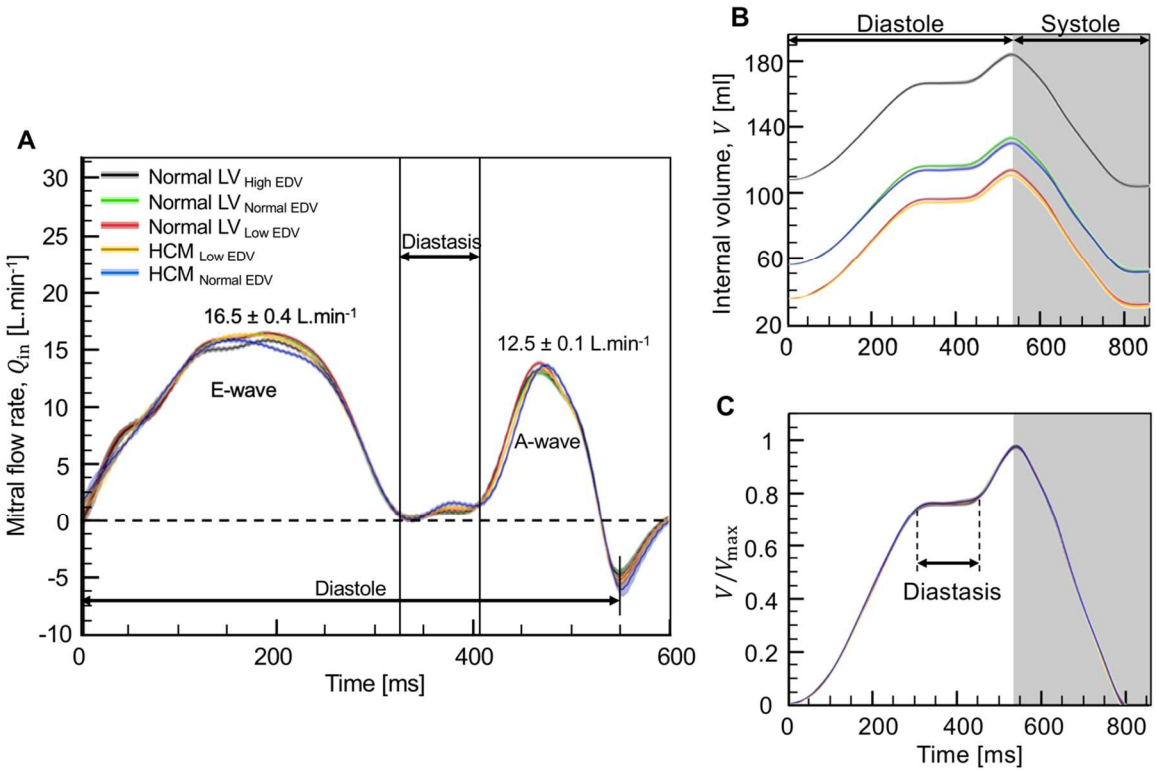

Figure 4-2. Flow rates and internal volumes of normal LV and HCM physical models at different EDVs. (A) Time-variation of mitral inflow rate (Q_{in}) in diastole. Peak flow rates during early filling (E-wave) and late filling (A-wave) were 16.3 ± 0.1 L.min^{-1} and 12.5 ± 0.1 L.min^{-1}, respectively. Time-variation of internal volume of each model (V) calculated from equation **Error! Reference source not found.** is shown in (B), while normalized internal volume (V/V_{max}) is shown in (C). Shaded error bars are shown for each part figure, to indicate ± 1 standard deviation (S.D) of the quantity across 25 consecutive cardiac cycles.

where υ, D_{MV}, and $Q_{\text{in,max,}}$ denote kinematic viscosity of the fluid medium (3.5 cSt), diameter of the mitral annulus (32 mm), and the peak mitral inflow rate, respectively. Reynolds number of approximately 3,000 was maintained across all test conditions.

4.2.1.2D Time-resolved particle image velocimetry (TR-PIV)

2D TR-PIV measurements were acquired for quantitative visualization of the intraventricular flow across varying model geometry and EDV (**Figure 4-1E**). A single-cavity high-speed Nd: YLF laser capable of providing 30 mJ/pulse at 1 kHz repetition rate (Photonics Industries International, Inc., NY, USA), in combination with sheet optics, was used to generate a 3-4 mm thick vertical laser sheet to illuminate two cross-sections of each model along 2 planes located at z=0 mm and z=10 mm (**Figure 4-1E**). The sheet optics consisted of: a diverging lens and converging lens for beam focusing; a 90-degree high-reflectivity mirror to deflect/change direction of the laser beam; and a plano-concave cylindrical lens (effective focal length=-10 mm) to convert the beam into a laser sheet. Polymethyl methacrylate (PMMA) fluorescent particles of diameters ranging between 1-20 µm were used as tracer particles and homogenously mixed before the start of each experiment. These particles were doped with Rhodamine-B dye and suspended in an aqueous solution, with absorption wavelength of approximately 532 nm and emission wavelength near 584 nm. A high-speed 1-megapixel CMOS camera (Phantom Miro 110, Vision Research Inc., Wayne, NJ, USA) was placed perpendicular to the laser sheet plane and used to acquire raw images of particles inside the model. The camera was outfitted with a 60 mm constant focal length lens (Nikon Micro Nikkor, Nikon Corporation, Tokyo, Japan) set to a maximum aperture of 2.8, and used to focus the illuminated particles. A 550 nm long-pass optical filter was attached to the lens. The camera frame rate was maintained constant at 1000 frames per second at full resolution (1024 pixels x 1024 pixels). We used a slightly magnified field of view (FOV) to resolve the flow field inside each model, as a result of which flow adjacent to the wall (and wall movement) was not captured.

For acquisition, both the high-speed camera and laser were simultaneously triggered at the starting time of diastole (start of piston retraction). 20 cardiac cycles of TR-PIV data were recorded for the entire diastole duration. TR-PIV data acquisition was started after running the

flow loop for 200 consecutive cardiac cycles to ensure flow characteristics reached a periodic steady state. For every test condition, TR-PIV measurements were acquired in 2 parallel long-axis planes separated by 10 mm (**Figure 4-1E**). DaVis 8.3.0 software (LaVision GmbH, Göttingen, Germany) was used for cross-correlation based processing of raw TR-PIV images. Multi-pass cross-correlation was used with initial interrogation window size 64×64 pixels (2 passes) and a smaller final interrogation window size of 32×32 pixels (2 passes), each with 50% overlap. For postprocessing, velocity vectors with a peak ratio of less than 1.2 were rejected and empty vectors were replaced by interpolation. Phase-averaging of 2D velocity components was performed across 20 cycles in DaVis software. Out-of-plane vorticity and circulation were calculated using custom scripts written in MATLAB (The Mathworks, Inc., Natick, MA).

4.2.2. Definitions of calculated quantities

4.2.2.1. Hemodynamic characteristics

Time-variation of the internal volume of the model (V) throughout the cardiac cycle was determined from the measured inflow rate (mitral, Q_{in}) and outflow rate (aortic, Q_{out}) using the relation:

$$V(t) = \int_0^t \left(Q_{\mathrm{out}}(t) - Q_{\mathrm{in}}(t)\right) dt \qquad \text{Eq. 4-3}$$

Stroke volume (SV), in units of ml/beat, was calculated as the difference of EDV and end systolic volume (ESV), both obtained from the curve of $V(t)$ versus t:

$$\mathrm{SV} = \mathrm{EDV} - \mathrm{ESV} \qquad \text{Eq. 4-4}$$

Cardiac output (CO), in units of L/min, was calculated from SV using the following equation:

$$\mathrm{CO} = (\mathrm{SV} \times 10^{-3}\,)\,\mathrm{HR} \qquad \text{Eq. 4-5}$$

where HR is the heart rate (beats/min).

4.2.2.2. Vortex formation time (VFT)

VFT is a non-dimensional time scale that has been used to characterize vortex rings formed during intraventricular filling (17,23-25). For the purpose of this study, VFT was calculated using the relation:

$$\mathrm{VFT} = \frac{\overline{U_\mathrm{E}}\,T_\mathrm{E}}{D_\mathrm{MV}} \qquad \text{Eq. 4-6}$$

where $\overline{U_\mathrm{E}}$ and T_E are the time-averaged inflow velocity during early filling (E-wave) and the E-wave time duration, respectively. Using the continuity equation for incompressible flow, we can express time-varying inflow velocity ($U_\mathrm{E}(t)$) in terms of the measured time-varying inflow rate during E-wave ($Q_\mathrm{E}(t)$) as:

$$U_\mathrm{E}(t) = \frac{Q_\mathrm{E}(t)}{\frac{\pi}{4}\,D_\mathrm{MV}^2} \qquad \text{Eq. 4-7}$$

Time-averaging equation **Error! Reference source not found.**4-7 across E-wave duration (t_E), we obtain:

$$\overline{U_\mathrm{E}} = \frac{\frac{1}{T_\mathrm{E}}\int_0^{T_\mathrm{E}} Q_\mathrm{E}\,dt}{\left(\frac{\pi}{4}\,D_\mathrm{MV}^2\right)} = \frac{4\,\overline{V_\mathrm{E}}}{\pi\,D_\mathrm{MV}^2\,T_\mathrm{E}} \qquad \text{Eq. 4-8}$$

where $\overline{V_\mathrm{E}}$ is the time-averaged volume of fluid filled inside the model during E-wave. Substituting equation 4-8 in equation 4-6, we obtain the following equation for VFT:

$$\mathrm{VFT} = \frac{4\,\overline{V_{\mathrm{E}}}}{\pi\, D_{\mathrm{MV}}^{3}} \qquad \text{Eq. 4-9}$$

4.2.2.3. Vorticity

Vorticity ($\vec{\omega}$) is a measure of the angular velocity of fluid rotation and is mathematically defined as the curl of the velocity vector field ($\vec{V}$). The out-of-plane component of vorticity in z-direction (ω_z) was calculated using the following equation:

$$\omega_{\mathrm{z}} = \nabla \times \vec{V} = \frac{\partial v}{\partial \mathrm{x}} - \frac{\partial u}{\partial \mathrm{y}} \qquad \text{Eq. 4-10}$$

where u and v are velocity vector components along the horizontal (x) and vertical (y) directions, respectively, obtained from TR-PIV measurements.

4.2.2.4. Vortex identification and circulation

The intraventricular filling vortex ring is a three-dimensional donut-shaped flow structure. In the case of 2D flow visualization (as in this study), only a cross-section of the 3D flow structure can be observed, appearing in the form of two counter-rotating vortices. Each vortex core was identified from the TR-PIV based velocity vector fields using the swirling strength (λ_{ci}) criterion (36), used in previous 2D PIV studies (29,32). The iso-surfaces of λ_{ci} were normalized by 2.6% of the maximum value for identification of vortex cores, as recommended in previous studies (29,32). Within the TR-PIV FOV, the counter-clockwise (CCW) vortex core was closer to the LVOT and propagated near what would be considered as the septal wall of the LV. The clockwise (CW) vortex core propagated near what would be considered as the lateral wall of the LV.

To quantify the strength of the intraventricular filling vortex, circulation Γ (in units of $cm^2.s^{-1}$) was calculated by integrating the out-of-plane z-vorticity (ω_z) within the surface area enclosed by the vortex (A):

$$\Gamma = \iint_A \omega_z \, dA = \sum_A \omega_z \, dx \, dy \qquad \text{Eq. 4-11}$$

Circulation provides a spatial estimate of the rotational strength of a vortex. Previous studies of intraventricular filling have examined this quantity using 2D PIV in physical models (3,32), and using echocardiographic-PIV (5,17) and phase-contrast cardiac MRI data (7) in human subjects.

We calculated circulation within an initial rectangular window measuring 3 mm x 2 mm (x-distance x y-distance) that was drawn centered around a vortex core, where the latter was identified using λ_{ci} criterion. The window size was iteratively increased along both axes and circulation was calculated. This process continued until the circulation from a window matched that of the immediately previous/smaller window. This iterative window sizing process was automated within a custom MATLAB script. The centroid of the final rectangular window used in calculating vortex core circulation was calculated to examine time variation of vortex core trajectory. We only tracked the diastolic vortex propagation during the E-wave, as breakdown of the vortex into smaller-scale flow structures occurred in diastasis. We did not track secondary vortices formed during A-wave.

We examined how normalized circulation of vortex ring cores (relative to peak values) varied as a function of a non-dimensional *formation time* (T^*), originally defined by Gharib et al. (26) to characterize vortex ring formation in an unconfined domain. T^* is representative of the length to diameter of the ejected jet (aspect ratio), and was calculated from the relation:

$$T^{*} = \frac{\overline{U}\, t}{D_{MV}} \qquad \text{Eq. 4-12}$$

where t is time in diastole, and $\overline{U}$ is time-average of inflow velocity calculated using the equation:

$$\overline{U} = \frac{4}{\pi {D_{MV}}^{2}\, T} \int_{0}^{T} Q_{in}(t)\, dt \qquad \text{Eq. 4-13}$$

where T denotes diastolic duration.

4.3. Results

4.3.1. **Hemodynamics**

Hemodynamic characteristics remained relatively unchanged when changing models and EDVs (**Table 4-2**). SV, CO and mean aortic pressure obtained in each test condition were within normal physiological range at a constant heart rate of 70 beats/minute. The relative standard deviation (ratio of standard deviation/mean) of hemodynamic characteristics of different cases was < 1.3%. VFT was calculated using equation **4-9**.**Error! Reference source not found.** and was found to be 4.4±0.9 across all test conditions, which is within the range for normal cardiac function (2). The low level of variation in hemodynamic characteristics was expected, as the piston pump operating characteristics (input voltage versus time waveform, stroke amplitude and frequency) were not changed when testing different physical models and EDVs.

Table 4-2. Hemodynamic characteristics obtained from experimental measurements of normal LV and HCM models under different EDVs. The following were maintained constant across all tests: 1) heart rate (HR)=70 beats/min; 2) diastole duration=66% of the cardiac cycle; 3) deceleration time (DT)=140 ms; and 4) diastasis duration=65 ms. SV = stroke volume; AP = aortic pressure; $Q_{\text{in,max}}$= peak (mitral) inflow rate; $Q_{\text{out,max}}$= peak (aortic) outflow rate; VFT = vortex formation time. SV and VFT were calculated using equation **4-4** and equation **4-9**, respectively. AP values denote minimum value in diastole/maximum value in systole. CO calculated from equation **4-5** was roughly 5.1 L/min across all test conditions. Mean and standard deviations of SV, AP, $Q_{\text{in,max}}$ and $Q_{\text{out,max}}$ were obtained from measurements across 25 consecutive cardiac cycles. VFT was calculated using equation **4-9**.

Model and test condition	EDV [ml/beat]	SV [ml/beat]	AP [mm Hg]	$Q_{\text{in,max}}$ [L/min]	$Q_{\text{out,max}}$ [L/min]	VFT
Normal LV $_{\text{Low EDV}}$	110	73±0.5	79/121±0.7	16.8±0.1	24.7±0.3	4.49
Normal LV $_{\text{Normal EDV}}$	129	73±0.4	79/121±0.5	16.3±0.1	23.9±0.2	4.45
Normal LV $_{\text{High EDV}}$	178	73±0.5	79/121±0.6	16.8±0.1	24.1±0.2	4.32
HCM $_{\text{Low EDV}}$	107	73±0.4	79/121±0.7	16.7±0.1	24.0±0.2	4.38
HCM $_{\text{Normal EDV}}$	126	73±0.4	79/121±0.7	16.3±0.1	24.0±0.2	4.31

The time-varying inflow (mitral flow) rate profile followed the physiologically observed bi-phasic pattern (**Figure 4-2A**), with 2 distinct peaks during early filling (E-wave) and late filling (A-wave) separated by an intermediate period of low inflow (diastasis). Deceleration time (DT) duration measured from the peak of E-wave to end of A-wave, and the ratio of peak flow rates in E-wave to A-wave (E/A), were both in the range expected for normal diastolic function (37). Internal volume of each model (**Figure 4-2B**), calculated from equation **4-4**, showed the same trend in time variation for both physical models at all EDVs. Normalized internal volume profiles, calculated relative to peak volume of each test condition, collapse on each other with minor deviation (**Figure 4-2C**). For a particular model geometry, changing EDV resulted in an increase or decrease in internal volume throughout the cycle by a fixed offset volume.

4.3.2. **Intraventricular flow field**

Vortex ring formation is observed in the central PIV plane within the normal LV model (**Error! Reference source not found.**A-**Error! Reference source not found.**C), in the form of a counter-rotating vortex pair (with oppositely signed vorticity), during peak E-wave in diastole (**Error! Reference source not found.**A). Vortex ring pinch-off from the inflow jet occurs before the mid-deceleration of E-wave, and both CW and CCW cores are enlarged in size (**Error! Reference source not found.**B). Counter-signed wall vorticity regions are observed adjacent to each vortex core, near the base of the normal LV model. The vortex cores start to converge with increasing filling time, leading to their interaction, followed by break down into secondary flow structures by end of diastasis (**Error! Reference source not found.**C). Overall, the observed filling vortex propagation in the normal LV model compares well with previous studies (3,11,31).

With decreasing initial volume and EDV of the normal LV model (**Figure 4-3D-F**), the following three differences can be observed compared to the normal EDV case (**Figure 4-3A-C**): 1) increased width of inflow jet; 2) increased axial penetration of the inflow jet into the LV; and 3) larger sized vortex cores. Diffuse vorticity regions with weaker magnitude are also observed in the low EDV case at the end of diastasis. Increasing EDV (**Figure 4-3G-H**) reduces the size of the vortex cores when compared to both normal EDV and low EDV. However, the vorticity magnitude is more diffuse in the case of high EDV than the other EDVs. The inflow jet in peak E-wave is widest in high EDV case (**Figure 4-3G**). At the end of diastasis, both vortex cores do not breakdown in high EDV (**Figure 4-3I**) unlike the other two EDVs, albeit with lower vorticity values as compared to normal EDV at the same time point (**Figure 4-3C**). Also, flow close to the apex of the normal LV model is weakest in high EDV case.

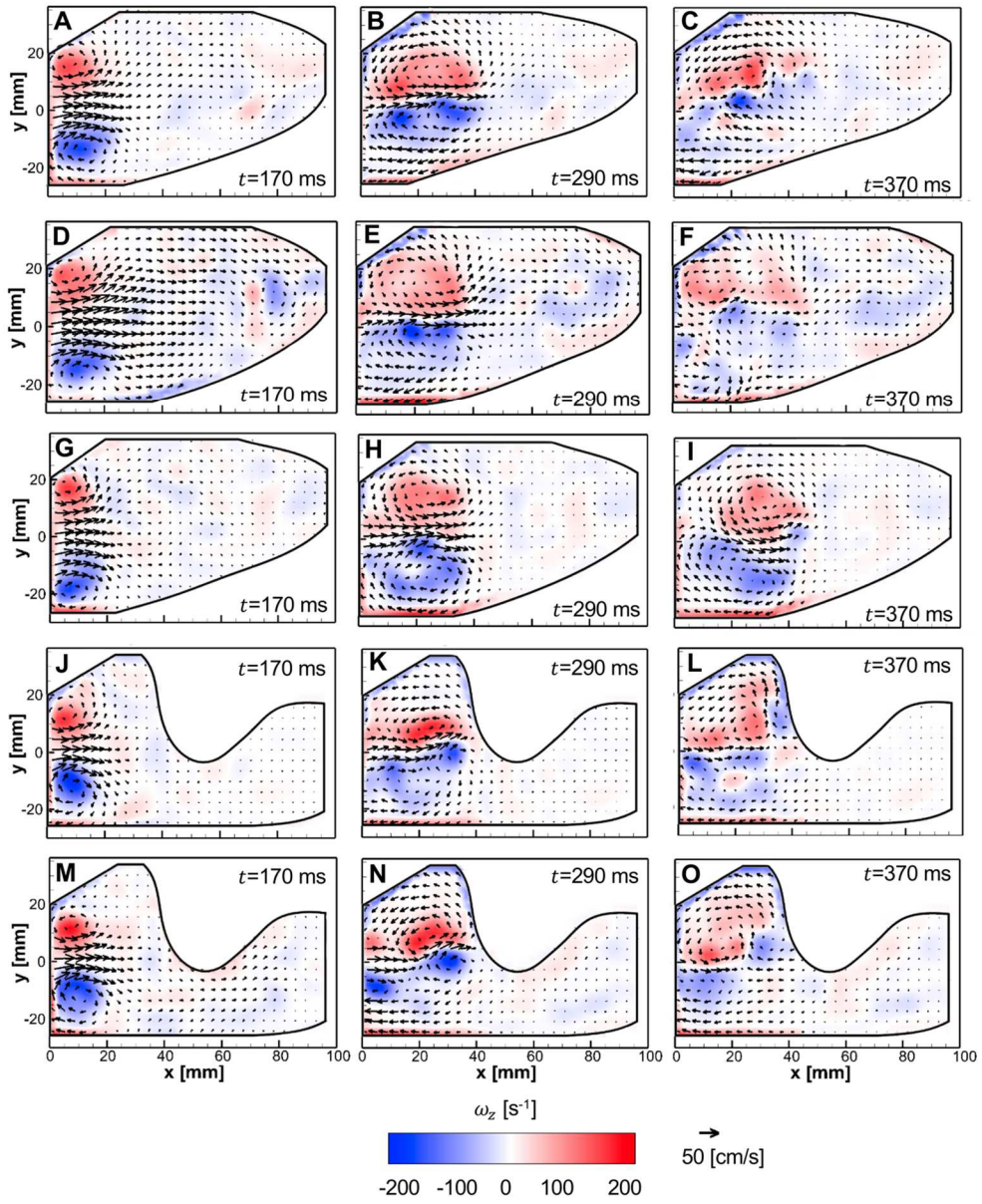

Figure 4-3. Velocity vector fields overlaid with z-vorticity contours (ω_z) at 3 different time instances in diastole, showing intraventricular flow fields of normal LV and HCM models. The following time points are shown along vertical columns from left to right: peak E-wave (t=170 ms), mid deceleration (t=290 ms), and end diastasis (t=370 ms). The first three horizontal rows (top to bottom direction) correspond to the normal LV model, at normal EDV (parts A-C), low EDV (parts D-F), and high EDV (parts G-I). The next two horizontal rows (top to bottom direction) correspond to HCM model with normal EDV (parts J-L) and low EDV (parts M-O). ω_z was calculated from processed TR-PIV velocity vector fields using equation **4-10**. Filling vortex strength and jet propagation are both diminished when changing from normal LV to HCM geometry. Additionally, the vortex ring cores persists longer in time within a larger internal cavity. For example, vortex ring cores at end diastasis in the normal LV model are clearly observed in high EDV (part I), whereas the cores at the same time instance are either mostly dissipated in low EDV (part F) or diminished in intensity for normal EDV (part C).

The HCM model at normal EDV shows smaller sized vortex cores in peak E-wave (**Figure 4-3J-K**) compared to the normal LV model. These vortex cores break down before the end of diastasis (**Figure 4-3L**). The primary vortex cores break down during deceleration phase in the HCM model at low EDV (**Figure 4-3N**), forming a secondary vortex pair that trails the primary pair. The inflow jet during E-wave is not symmetric about the apical-basal centerline axis (as in the normal LV model), and tends to be skewed toward the septal wall with CCW vorticity. Across both normal and low EDVs, both the width and axial penetration of the inflow jet are diminished compared to the normal LV model.

4.3.3. **Diastolic vortex characteristics**

Vortex identification and tracking were performed on the TR-PIV based velocity vector fields to quantify differences in diastolic vortex propagation. In the normal LV model, time-varying locations of the counter-rotating vortex cores (centroid of each vortex core) are nearly identical in both normal EDV and low EDV (**Error! Reference source not found.**A). The radial distance between the cores of the counter-signed pair decreases with increasing longitudinal/axial distance into the LV, suggesting that the core positions are influenced by the gross shape of the normal LV model. The high EDV case departs from this trajectory and shows a nearly centerline symmetric propagation, with nearly constant vortex ring diameter (in the central PIV plane). Lower radial confinement of the vortex ring can be expected in the high EDV case with the largest internal volume (**Figure 4-2B**), which allows for the cores to remain farther apart unlike the lower EDV cases. Both normal and low EDV conditions in the HCM model show decreasing separation between the counter-rotating vortex pair with increasing time (equivalent to increasing x-distance in **Figure 4-4B**), similar to what was observed in the normal LV model for these EDVs. The longitudinal propagation of the CCW core is restricted in the HCM model (either EDV), due to the core being proximal to the hypertrophied portion in the septal wall.

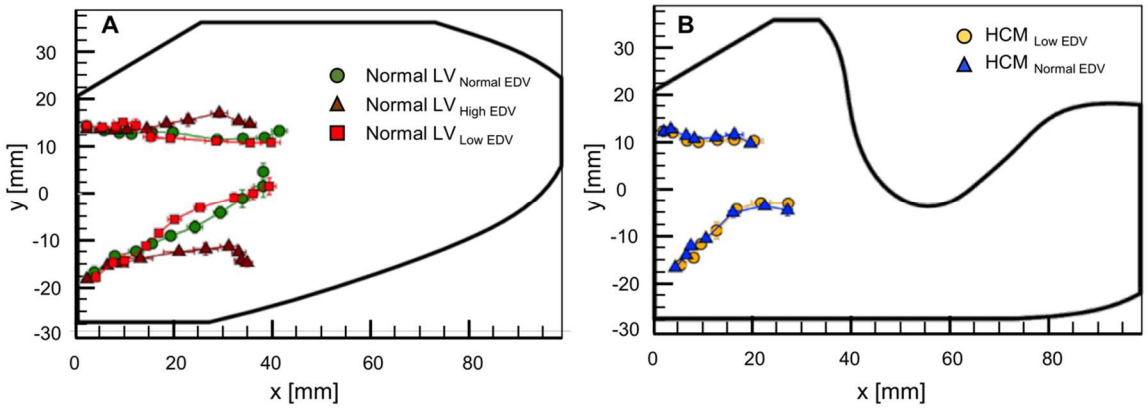

Figure 4-4. Vortex core trajectories for (A) normal LV and (B) HCM physical models. Error bars in x- and y- axes indicate ±1 S.D of core location across 5 cycles.

Across all test conditions, normalized circulation of the diastolic vortex ring (**Figure 4-5A**) reaches its peak value at a non-dimensional time instant (also known as formation time (26)) of approximately 1.6 (CCW core) and 1 (CW core). This instant (also known as pinch-off time) corresponds to the non-dimensional time when the vortex ring pinches off from the inflow jet (26,28). As compared to the CCW core that propagates farther away from the nearest confining wall (septal wall of the LV), earlier pinch-off occurs in the CW core that propagates closely along the lateral wall of the LV. The pinched-off vortex ring maintains peak circulation (i.e., Γ/Γ_0=1) for a short non-dimensional time duration before decaying in strength. Across both HCM and normal LV models, the vortex ring formation process (i.e., time before pinch-off) remains essentially unaffected. The time period between pinch-off to the onset of decay, where peak circulation essentially remains constant, increases with increase in the EDV for either model geometry (**Figure 4-5A**). Increasing EDV from normal to high value in normal LV model results in lowering the slope of the decay region. All of the above observations are unchanged also for normalized circulation in the off-center plane at z=10 mm (**Figure 4-5B**).

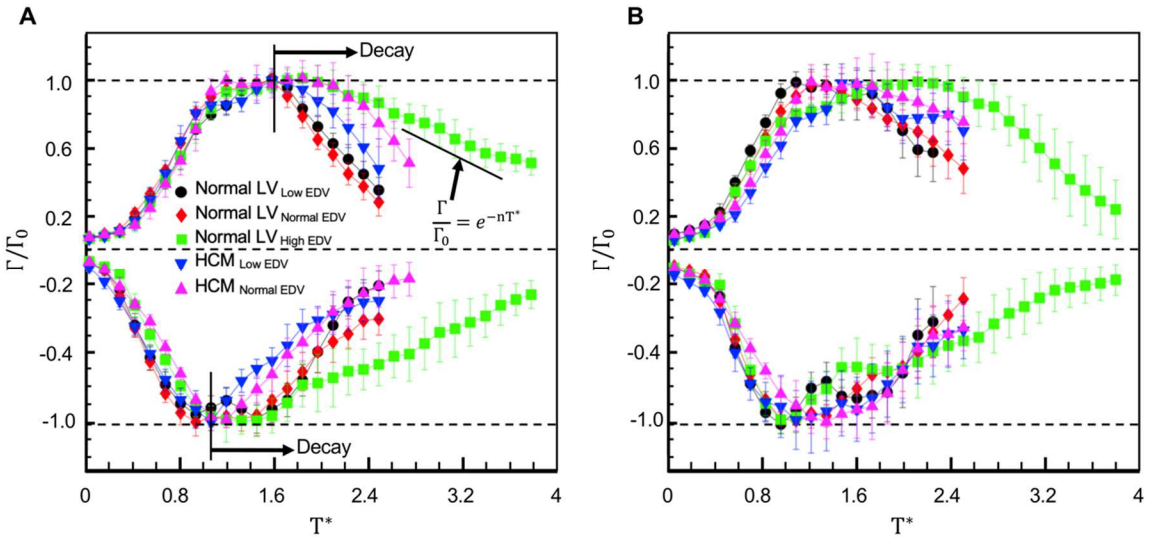

Figure 4-5. Variation of normalized vortex core circulation (Γ/Γ_0), defined relative to peak circulation (Γ_0), as a function of dimensionless formation time (T^*). Circulation (Γ) and T^* were calculated using equation **4-11**Error! Reference source not found. and equation **4-12**, respectively. (A) Central PIV plane (z=0 mm), and (B) off-centered PIV plane (z=10 mm). CCW= counterclockwise; CW=clockwise. Error bars indicate $\pm$1 S.D of circulation across 5 cycles.

Peak circulation (Γ_0) values and ratio of peak circulation relative to the peak circulation value of normal LV under normal EDV ($\Gamma_{0,\text{Normal LV and EDV}}$) are provided in **Table 4-3**, where circulation was determined from TR-PIV data at the central plane (z=0 mm). In both the normal LV and HCM models, increasing EDV decreased peak circulation of the CCW vortex. Across both models, the CW vortex did not show significant difference (over 1 standard deviation) in peak circulation with change in EDV. We did not anticipate major differences in the CW vortex core of the normal LV model when changing EDV, as this core propagates close to the lateral wall of the LV. Dissipative interactions with the lateral wall could lower the vorticity in the CW vortex core and diminish the extent of its propagation. For a given EDV (low or normal), peak circulation of the CCW vortex propagating near the septal wall was lowest for the HCM model as compared to the normal model.

Table 4-3. . Peak circulation (Γ_0) and dimensionless peak circulation defined relative to Γ_0 of normal LV model at normal EDV ($\Gamma_0/\Gamma_{0,\text{Normal LV and EDV}}$). CCW=counter-clockwise; CW=clockwise. Circulation (Γ) of CW and CCW vortex cores were calculated from equation **4-11**, at multiple time points along the E-wave for 5 cardiac cycles of TR-PIV data acquired at the central plane (z=0 mm).

Physical model	Vortex core rotation	Γ_0 [$cm^2.s^{-1}$]			$\Gamma_0/\Gamma_{0,\text{Normal LV and EDV}}$		
		Low EDV	Normal EDV	High EDV	Low EDV	Normal EDV	High EDV
Normal LV	CCW	260 ± 10	242 ± 8	215 ± 18	1.07 ± 0.07	1.00	0.88 ± 0.09
	CW	189 ± 12	196 ± 12	211 ± 15	0.97 ± 0.11	1.00	1.08 ± 0.13
HCM	CCW	193 ± 12	170 ± 13	-	0.79 ± 0.07	0.70 ± 0.07	-
	CW	223 ± 8	214 ± 8	-	1.14 ± 0.10	1.09 ± 0.11	-

In contrast to the CCW vortex, peak circulation of the CW vortex was largest in the HCM model for a given EDV. This is also in contrast with the peak circulation of the CW vortex in the normal LV model, which was lower than that of the CCW vortex. It is important to note that the CW vortex in the HCM model (as visualized in either 2D PIV plane) propagates close to the lateral wall opposite the LVOT. It is possible that the CW vortex in the HCM model entrains some of the kinetic energy of the CCW vortex, due to the latter being restricted in propagation by the region with septal wall thickening. This asymmetry between the strengths of the two vortices in the diastolic vortex pair is visually supported by the vorticity field (compare **Figure 4-3B** and **Figure 4-3K**, both at mid-deceleration).

To examine the potential reason as to why the less confined domain (low EDV) showed a larger value for peak circulation (CCW core), we characterized the shape of the normal LV model from digital planimetry measurements after static pressurization to a pre-determined EDV. The normal LV model was fitted into the enclosing acrylic chamber (**Figure 4-1D**), and both the internal

volume of the model as well as the chamber were filled with water. The chamber was open to atmosphere. The internal volume was filled to match each of the different EDVs examined for normal LV model (**Table 4-2**). The TR-PIV camera was used to acquire images of the static model along the y-z plane (short-axis) at 7 x-y planes along the long-axis (S1-S7 in **Figure 4-6A**). Image of a custom calibration grid with known physical distances was also acquired at each plane. Cross-sectional surfaces were tracked from the short-axis images using SolidWorks software (Dassault Systèmes SE, Vélizy-Villacoublay, France). Dimensions of the major axis (d_1) and minor axis (d_2) were measured from the tracked surfaces following calibration (**Figure 4-6B**). The non-dimensional major axis dimension, defined relative to mitral annulus diameter (D_{MV}), decreased with increasing distance from mitral annulus (moving toward apex) for all EDVs. The low EDV case resulted in the largest d_1, while the normal and high EDVs showed marginal difference relative to each other (**Figure 4-6C**). It is important to note that d_1 was defined in the same plane of observation as the central plane TR-PIV data (z=0 mm). As the low EDV case had the largest d_1, larger spatial region could have been available for CCW vortex core to expand at the central PIV plane (z=0 mm) compared to the normal and high EDVs, particularly at smaller x/c locations near the mitral annulus. The aspect ratio of the static model, defined as the ratio of major to minor axis dimension (d_1/d_2), showed that the high EDV case resulted in a nearly spherical geometry compared to the low and normal EDVs (**Figure 4-6C**). The low EDV case had the highest variation of aspect ratio when moving from base (x/c=0) to apex (x/c=1), suggesting that the larger sphericity of the model could have also played a role in decreasing peak circulation of the CCW vortex core.

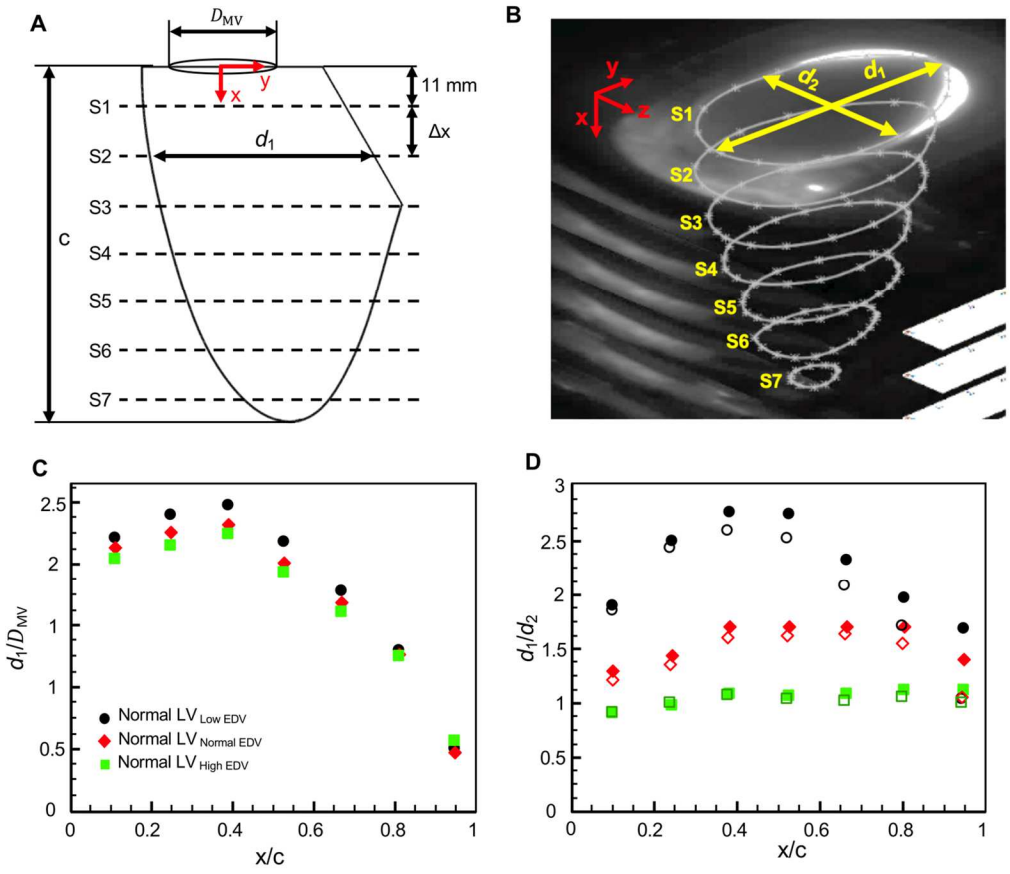

Figure 4-6. Dimensions of the static/non-moving normal LV physical model when filled to low, normal, and high EDV values. (A) 7 parallel x-y planes along the long-axis (S1-S7) were selected for digital planimetry measurements, with equal increments of Δx=12.7 mm. An image of the static, normal LV physical model along the y-z plane was acquired for each x-y plane location indicated in (A). Cross-sectional shape of the static, normal LV model along each y-z plane was tracked using SolidWorks software. Tracked cross-sectional surfaces are shown in (B), overlaid on raw images of S1-S7. Major axis dimensions (d_1) and minor axes dimensions (d_2) of the static, normal LV model were obtained from image tracking at the 7 selected x-y planes (S1-S7). Only planar images (i.e., along y-z plane) were acquired, and isometric projections are shown in (B) for display purposes. (C) Non-dimensional major axis dimension (d_1) at z=0 mm, defined relative to mitral annulus diameter $\boldsymbol{D_{MV}}$, is shown as a function of normalized long-axis distance (x/c) of the x-y planes (S1-S7) where cross-sections were imaged. (D) Ratio of d_1 to d_2 plotted as a function of normalized long-axis distance (x/c). Filled and hollow markers in (D) correspond to the central PIV plane (z=0 mm) and off-center PIV plane (z=10 mm), respectively. The high EDV case results in a nearly circular cross-section (i.e., d_1/d_2 nearly equal to 1).

To examine how EDV impacts the longevity of the propagating diastolic vortex, we fit an exponential curve to the decay portion of normalized circulation (Γ/Γ_0) versus formation time (T^*) at the central PIV plane (**Figure 4-5A**). Linear regression was performed on the decay

portion of the data on a semi-log plot of Γ/Γ_0 (natural logarithm scale) versus T^*. The slope of the line of best fit (n) thus represents the rate of decay of circulation (i.e., $d/dT^*(\Gamma/\Gamma_0)$). The normal LV model at low EDV showed the highest rate of decay, followed by the HCM model at low EDV (**Figure 4-7A**).

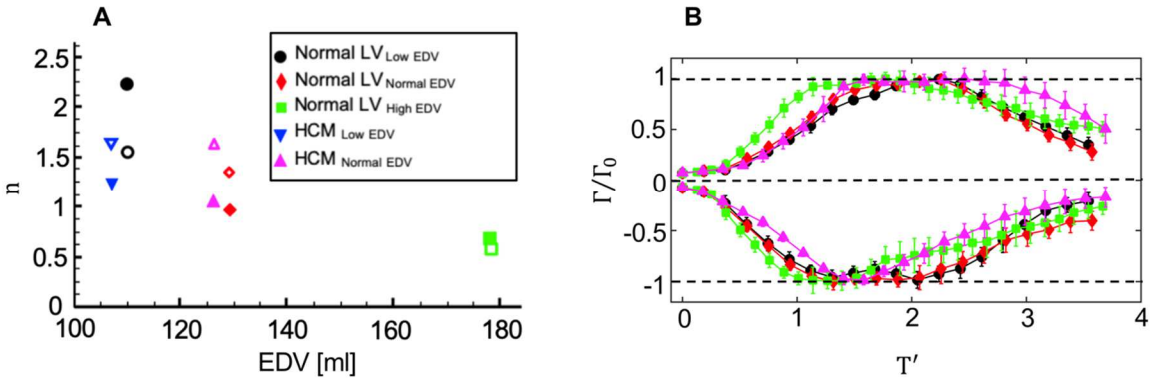

Figure 4-7. Normalized circulation decay and modified dimensionless time at the central PIV plane (z=0 mm). We fitted an exponential curve for the decay portion of normalized vortex core circulation (Γ/Γ_0) versus dimensionless formation time (T^*), as shown in **Figure 4-5**, in the form: $\Gamma/\Gamma_0 = e^{-nT^*}$. Variation of n with EDV for the normal LV and HCM models is shown in (A), where n represents the rate of decay of normalized circulation. Filled and hollow markers in (A) correspond to the CW and CCW vortex cores, respectively. (B) Normalized circulation of the normal LV model (all 3 EDVs) is plotted as a function of modified dimensionless time (T') calculated using equation **4-14**. $\overline{d_1}$ and $\overline{d_2}$ denote the major axis and minor axis dimensions of the static normal LV model when filled to a specific EDV (normal/low/high), respectively, spatially averaged across the long axis of the model (i.e., averages of d_1 and d_2 values obtained in 7 planes defined in **Figure 4-6A**).

As expected, the CW vortex core in the normal LV model at low EDV had the highest decay rate, due to its proximity to the lateral wall of the LV. Increasing EDV in either model resulted in lowering rate of decay of circulation of both vortex cores. The CCW vortex core of the HCM model at low EDV showed higher rate of decay compared to CW vortex core, suggesting that the interaction of CCW vortex core with the hypertrophied region reduced its vorticity at a faster rate. The faster decay of CCW vortex core was also observed at normal EDV in the HCM model. Collectively, these results suggest that increasing EDV results in lowering peak circulation of the CCW vortex core while slowing down its decay.

To examine how normalized circulation scaled across EDVs, we used the major and minor axes dimensions of the normal LV model to define a modified dimensionless time scale:

$$\mathrm{T}' = \frac{4\overline{U}\,(\mathrm{EDV})^{1/3}\,t}{\pi\,\overline{d_1}\,\overline{d_2}} \qquad \text{Eq. 4-14}$$

where $\overline{d_1}$ and $\overline{d_2}$ are major axis and minor axis dimensions of the static normal LV model, respectively, spatially averaged across the long axis of the model (x/c from 0 to 1, see **Figure 4-6A**). The time-averaged inflow velocity $\overline{U}$ is defined by equation **4-8**). The formulation of T' was obtained by using averaged cross-sectional area of the normal LV model in place of D_{MV} in equation **4-14**). The cubic root of EDV was included in the numerator of equation **4-14**) to obtain the correct non-dimensional form T' and also explicitly account for EDV. Normalized circulation of all the 3 EDV cases collapsed closely when plotted against T', within a maximum difference of 10% (**Figure 4-7B**).

4.4. Discussion

Intraventricular filling dynamics has been extensively studied using medical imaging on human subjects, physical and computational modeling (1-17,23,27,30-32). These studies generally posit that alterations to the diastolic vortex can be used for clinical diagnosis of cardiac dysfunction (2). However, there is a gap in our understanding as to how the diastolic vortex is affected when the internal volume of the LV is reduced without changing the LV geometry. Besides subject-specific variability, such an understanding can be valuable in LVDD where concentric LVH results in reduced LV internal volume (20). Further, congenital diseases such as HCM (22) can also lower the LV internal volume in addition to changing LV shape. This study sought to examine alterations to the diastolic vortex when internal volume was reduced within a physical model of an anatomical/normal LV as well as a representative HCM physical model. We hypothesized that increasing confinement via lowering EDV and/or changing the LV geometry would alter peak

circulation and increase the rate of circulation decay following pinch-off. The mechanistic rationale for our hypothesis was based on a study of laminar vortex ring propagation within a tube by Stewart et al. (29), where increasing confinement increased the rate of decay of circulation. Our results showed that increasing confinement (lowering EDV) increases both the peak circulation of the CCW vortex core closer to the LVOT and the rate of decay of circulation. Increasing confinement via asymmetric wall thickening in the HCM model also resulted in the same outcomes.

The vortex formation time (VFT), indicative of the dimensionless time when a vortex ring pinches off from its trailing jet (limit of largest possible circulation), has been widely examined for its capability to discriminate normal subjects from those with cardiac dysfunction (23-25). VFT is appealing from a clinical standpoint, as its computation only requires basic hemodynamic (transmitral flow) and structural information (time-averaged mitral valve diameter) (2). However, VFT formulation is based on vortex ring propagation in an unconfined domain, and this assumption has raised questions with respect to its application in a highly confined LV (28). A recent study by Stewart et al. (27) showed that VFT is not affected by diastolic impairment when considering the actual pinch-off time for VFT calculation (as opposed to E-wave duration as in the definition). Further, cardiac VFT formulation assumes E- and A-waves to be distinct (2), which can be challenged in the face of overlapping E- and A-waves that are observed in exercise conditions (38). To the best of the authors' knowledge, the question of how increasing confinement imposed by the LV cavity impacts the diastolic vortex has not been examined from a fluid dynamic perspective. Though our VFT values were in the normal range of 4-5 (2), pinch-off (formation time where normalized circulation equals unity) occurred well before the end of E-wave in all our test conditions. The occurrence of pinch-off before the end of E-wave was also reported by Stewart et al. (27) from data on human subjects in both normal and LVDD conditions.

In both the normal LV and HCM models, peak circulation of the CCW vortex core was subject to a larger level of change with lowering EDV as compared to CW vortex core. Peak circulation of the CCW vortex core decreased with increasing EDV. Since the stroke volume was maintained nearly constant across all EDVs in both physical models, increased internal pressure can be expected when lowering EDV. Vorticity generation in the fluid domain is known to be controlled by tangential pressure gradients (39), which could potentially be the driving reason behind the increase in peak CCW circulation at lower EDV. The HCM model showed lower peak CCW circulation compared to the normal LV. Interestingly, the CW vortex core was stronger than the CCW vortex core in the HCM model, in contrast to the normal LV where the CCW vortex had a larger peak circulation than the CW vortex. A likely reason for this disparity in CW and CCW vortex circulation of HCM model is due to the asymmetric wall thickening near the CCW vortex, which restricts propagation of CCW vortex. The CW vortex can increase in strength by entraining vorticity from the CCW vortex in the HCM model due to closer spatial proximity (lower EDV in HCM compared to normal LV model). The proximity of the CW vortex to the lateral wall resulted in earlier onset of its decay as compared to the CCW vortex (in both models), as wall-vortex interactions have been previously noted to lower circulation via cross-diffusive annihilation of vorticity (39,29).

Identical to the findings of Stewart et al. (29), we observed that the formation process was nearly unaffected by confinement, as the pinch-off time was nearly the same across all EDVs and models. However, we observed a marked difference in the rate of decay of circulation. Similar to the findings on radially confined vortex rings (29), increasing confinement via decreasing EDV resulted in increasing the rate of decay of circulation. Across all test conditions examined in this study, the high EDV case showed the lowest rate of decay of circulation. The static shape of the normal LV physical model was observed to be more spherical at high EDV, resulting in a lower level of confinement. Previous studies of dilated cardiomyopathy, where the LV is more

spherical, have reported the filling vortex to persist longer in diastole (9). This was also observed in our experimental findings.

The cardiac VFT (equation **4-9**)) does not factor the specific geometry of the LV (other than EDV), as the formation time (equation **4-12Error! Reference source not found.**)) that it was originally obtained from was based on a study of vortex ring propagation in a semi-infinite domain. The formation time provides a reasonably accurate representation of the initial growth and pinch-off process of the vortex ring, and was essentially insensitive to the domain geometry in our study. However, the decay of the vortex ring could not be scaled between EDVs using the formation time. We incorporated the average LV cross-sectional area and EDV into the formation time to arrive at a modified dimensionless time, T' (equation **4-14**)). The decay of normalized circulation across all EDV conditions in the normal LV model were nearly unchanged using T', suggesting that the model shape plays a critical role in controlling decay of the diastolic vortex.

As is the case with most modeling studies of cardiac flows, our findings must be weighed with consideration to the limitations of our approach. Despite the anatomical geometry of our models, the stiffness and material characteristics were not physiological. This is an inherent limitation of the silicones used in casting the physical models. Anatomical complexities within the LV cavity, including trabeculae and papillary muscles (16), were not considered in the physical models. The HCM geometry, though obtained from previous studies (33-34), should be considered only as a representative example as there are well-documented morphological variations of this disease (37). We positioned the mitral valve in a non-physiological location (upstream of the LV), as we did not want to introduce any artifacts in vortex formation due to differential leaflet kinematics. The flow within the LV is highly three-dimensional, but we were only able to resolve 2D velocity components from 2D TR-PIV measurements. This simplification is not expected to impact normalized circulation of the normal LV model at the two PIV planes, as circulation by definition is computed within a closed curve. However, we cannot confidently declare whether the central

plane is the plane of maximum circulation, particularly in the asymmetrically-shaped HCM model. Despite this simplification, we expect that trends of normalized circulation decay across models to be unaffected.

4.5. Conclusion

We experimentally examined diastolic vortex properties in normal LV and HCM physical models within a left heart simulator, across varying EDVs and under identical prescribed mitral inflow rates. Formation and pinch-off of the diastolic vortex ring were nearly unaffected with change in model geometry and EDV. VFT was also found to be nearly unchanged with EDV and model geometry, and was in the reported range of normal cardiac function (~4-5). However, pinch-off occurred before the end of E-wave in all test conditions. Both peak circulation and rate of decay of circulation (after pinch-off) were altered with change in EDV. Increasing confinement of the internal cavity of the LV, by either decreasing EDV or via asymmetric wall thickening (HCM), increased the rate of decay of circulation. These findings can be potentially helpful in improving our understanding of filling vortex dynamics in LVDD.

Funding. This work was supported by the Oklahoma Center for the Advancement of Science and Technology (project number HR14-022 to A.S.).

4.6. References

1. Rodevand, O., Bjornerheim, R., Edvardsen, T., Smiseth, O.A. and Ihlen, H., 1999. Diastolic flow pattern in the normal left ventricle. Journal of the American Society of Echocardiography, 12(6), pp.500-507.

2. Gharib, M., Rambod, E., Kheradvar, A., Sahn, D.J. and Dabiri, J.O., 2006. Optimal vortex formation as an index of cardiac health. Proceedings of the National Academy of Sciences, 103(16), pp.6305-6308.

3. Pierrakos, O. and P.P. Vlachos, The effect of vortex formation on left ventricular filling and mitral valve efficiency. Journal of biomechanical engineering, 2006. 128(4): p. 527-539.

4. Eriksson, J., Dyverfeldt, P., Engvall, J., Bolger, A.F., Ebbers, T. and Carlhäll, C.J., 2011. Quantification of presystolic blood flow organization and energetics in the human left ventricle. American Journal of Physiology-Heart and Circulatory Physiology, 300(6), pp.H2135-H2141.

5. Kheradvar, A., Assadi, R., Falahatpisheh, A. and Sengupta, P.P., 2012. Assessment of transmitral vortex formation in patients with diastolic dysfunction. Journal of the American Society of Echocardiography, 25(2), pp.220-227.

6. Töger, J., Kanski, M., Carlsson, M., Kovács, S.J., Söderlind, G., Arheden, H. and Heiberg, E., 2012. Vortex Ring Formation in the Left Ventricle of the Heart: Analysis by 4D Flow MRI and Lagrangian Coherent Structures. Annals of Biomedical Engineering, pp.1-11.

7. Charonko, J.J., Kumar, R., Stewart, K., Little, W.C. and Vlachos, P.P., 2013. Vortices formed on the mitral valve tips aid normal left ventricular filling. Annals of Biomedical Engineering, 41(5), pp.1049-1061.

8. Prinz, C., Lehmann, R., Brandao da Silva, D., Jurczak, B., Bitter, T., Faber, L. and Horstkotte, D., 2014. Echocardiographic particle image velocimetry for the evaluation of diastolic function in hypertrophic nonobstructive cardiomyopathy. Echocardiography, 31(7), pp.886-894.

9. Bermejo, J., Benito, Y., Alhama, M., Yotti, R., Martínez-Legazpi, P., del Villar, C.P., Pérez-David, E., González-Mansilla, A., Santa-Marta, C., Barrio, A. and Fernández-Avilés, F., 2014. Intraventricular vortex properties in nonischemic dilated cardiomyopathy. American Journal of Physiology-Heart and Circulatory Physiology, 306(5), pp.H718-H729.

10. Elbaz, M.S., Calkoen, E.E., Westenberg, J.J., Lelieveldt, B.P., Roest, A.A. and van der Geest, R.J., 2014. Vortex flow during early and late left ventricular filling in normal subjects: quantitative characterization using retrospectively-gated 4D flow cardiovascular magnetic resonance and three-dimensional vortex core analysis. Journal of Cardiovascular Magnetic Resonance, 16(1), p.1.

11. Seo, J-H., Vedula, V., Abraham, T., Lardo, A. C., Dawoud, F., Luo, H., Mittal, R., 2014. Effect of the mitral valve on diastolic flow patterns. Physics of Fluids 26, 121901-14, doi: 10.1063/1.4904094.

12. Calkoen, E.E., Elbaz, M.S., Westenberg, J.J., Kroft, L.J., Hazekamp, M.G., Roest, A.A. and van der Geest, R.J., 2015. Altered left ventricular vortex ring formation by 4-dimensional flow magnetic resonance imaging after repair of atrioventricular septal defects. The Journal of Thoracic and Cardiovascular Surgery, 150(5), pp.1233-1240.

13. Rossini, L., Martinez-Legazpi, P., Benito, Y., del Villar, C.P., Gonzalez-Mansilla, A., Barrio, A., Borja, M.G., Yotti, R., Kahn, A.M., Shadden, S.C. and Fernández-Avilés, F., 2015. Clinical assessment of intraventricular blood transport in patients undergoing cardiac resynchronization therapy. Meccanica, pp.1-14.

14. Elbaz, M.S., van der Geest, R.J., Calkoen, E.E., de Roos, A., Lelieveldt, B.P., Roest, A.A. and Westenberg, J.J., 2016. Assessment of viscous energy loss and the association with three-dimensional vortex ring formation in left ventricular inflow: In vivo evaluation using four-dimensional flow MRI. Magnetic Resonance in Medicine.

15. Arvidsson, P. M., Kovács, S. J., Töger, J., Borgquist, R., Heiberg, E., Carlsson, M., & Arheden, H. (2016). Vortex ring behavior provides the epigenetic blueprint for the human heart. Scientific reports, 6, 22021.

16. Vedula, V., Seo, J. H., Lardo, A. C., & Mittal, R. (2016). Effect of trabeculae and papillary muscles on the hemodynamics of the left ventricle. Theoretical and Computational Fluid Dynamics, 30(1-2), 3-21.

17. Hong, G.R., Pedrizzetti, G., Tonti, G., Li, P., Wei, Z., Kim, J.K., Baweja, A., Liu, S., Chung, N., Houle, H. and Narula, J., 2008. Characterization and quantification of vortex flow in the human left ventricle by contrast echocardiography using vector particle image velocimetry. JACC: Cardiovascular Imaging, 1(6), pp.705-717.

18. Zile, M.R. and Brutsaert, D.L., 2002. New concepts in diastolic dysfunction and diastolic heart failure: Part I diagnosis, prognosis, and measurements of diastolic function. Circulation, 105(11), pp.1387-1393.

19. Zile, M.R. and Brutsaert, D.L., 2002. New concepts in diastolic dysfunction and diastolic heart failure: part II. Circulation, 105(12), pp.1503-1508.

20. Wood, P., Piran, S. and Liu, P.P., 2011. Diastolic heart failure: progress, treatment challenges, and prevention. Canadian Journal of Cardiology, 27(3), pp.302-310.

21. Gaasch, W.H. and Zile, M.R., 2004. Left ventricular diastolic dysfunction and diastolic heart failure. Annual Review of Medicine, 55, pp.373-394.

22. Maron, B. J., Ommen, S. R., Semsarian, C., Spirito, P., Olivotto, I., & Maron, M. S. (2014). Hypertrophic cardiomyopathy: present and future, with translation into contemporary cardiovascular medicine. Journal of the American College of Cardiology, 64(1), 83-99.

23. Poh, K.K., Lee, L.C., Shen, L., Chong, E., Tan, Y.L., Chai, P., Yeo, T.C. and Wood, M.J., 2011. Left ventricular fluid dynamics in heart failure: echocardiographic measurement and utilities of vortex formation time. European Heart Journal-Cardiovascular Imaging, p.jer288.

24. Ghosh, E., Shmuylovich, L. and Kovács, S.J., 2010. Vortex formation time-to-left ventricular early rapid filling relation: model-based prediction with echocardiographic validation. Journal of Applied Physiology, 109(6), pp.1812-1819.

25. Maragiannis, D., Alvarez, P.A., Schutt, R.C., Chin, K., Buergler, J.M., Little, S.H., Shah, D.J. and Nagueh, S.F., 2015. Vortex Formation Time Index in Patients With Hypertrophic Cardiomyopathy. JACC: Cardiovascular Imaging.

26. Gharib, M., Rambod, E., & Shariff, K. (1998). A universal time scale for vortex ring formation. Journal of Fluid Mechanics, 360, 121-140.

27. Stewart, K.C., Charonko, J.C., Niebel, C.L., Little, W.C. and Vlachos, P.P., 2012. Left ventricular vortex formation is unaffected by diastolic impairment. American Journal of Physiology-Heart and Circulatory Physiology, 303(10), pp.H1255-H1262.

28. Pasipoularides, A., Vlachos, P. P., & Little, W. C. (2015). Vortex formation time is not an index of ventricular function. Journal of cardiovascular translational research, 8(1), 54-58.

29. Stewart, K. C., Niebel, C. L., Jung, S., & Vlachos, P. P. (2012). The decay of confined vortex rings. Experiments in fluids, 53(1), 163-171.

30. Okafor, I. U., Santhanakrishnan, A., Chaffins, B. D., Mirabella, L., Oshinski, J. N., and Yoganathan, A. P., 2015. Cardiovascular magnetic resonance compatible physical model of the left ventricle for multi-modality characterization of wall motion and hemodynamics. Journal of Cardiovascular Magnetic Resonance,17(1), 51. http://doi.org/10.1186/s12968-015-0154-9

31. Okafor, I.U., Santhanakrishnan, A., Raghav, V.S. and Yoganathan, A.P., 2015. Role of mitral annulus diastolic geometry on intraventricular filling dynamics. Journal of Biomechanical Engineering, 137(12), p.121007.

32. Santhanakrishnan, A., Okafor, I., Kumar, G. and Yoganathan, A.P., 2016. Atrial systole enhances intraventricular filling flow propagation during increasing heart rate. Journal of Biomechanics, 49(4), pp.618-623.

33. Sasson, Z., Rakowski, H. and Wigle, E.D., 1988. Hypertrophic cardiomyopathy. Cardiology Clinics, 6(2), pp.233-288.

34. Lefebvre, X.P., He, S., Levine, R.A. and Yoganathan, A.P., 1995. Systolic anterior motion of the mitral valve in hypertrophic cardiomyopathy: an in vitro pulsatile flow study. The Journal of Heart Valve Disease, 4(4), p.422.

35. Motoyasu, M., Kurita, T., Onishi, K., Uemura, S., Tanigawa, T., Okinaka, T., Takeda, K., Nakano, T., Ito, M. and Sakuma, H., 2008. Correlation between late gadolinium enhancement and diastolic function in hypertrophic cardiomyopathy assessed by magnetic resonance imaging. Circulation Journal, 72(3), pp.378-383.

36. Zhou, J., Adrian, R. J., Balachandar, S., Kendall, T. M., 1999. Mechanisms for generating coherent packets of hairpin vortices in channel flow. Journal of Fluid Mechanics 387, 353–396.

37. Leong, D. P., De Pasquale, C. G., & Selvanayagam, J. B. (2010). Heart failure with normal ejection fraction: the complementary roles of echocardiography and CMR imaging. JACC: Cardiovascular Imaging, 3(4), 409-420.

38. Iliceto S, D'Ambrosio G, Marangelli V, Amico A, Di Biase M, Rizzon P. Echo-Doppler evaluation of the effects of heart rate increments on left atrial pump function in normal human subjects. Eur Heart J 12:345-51, 1991.

39. Morton, B. R. (1984). The generation and decay of vorticity. Geophysical & Astrophysical Fluid Dynamics, 28(3-4), 277-308.

CHAPTER V

5. EFFECTS OF VARYING TRANSMITRAL INFLOW PROFILE ON FILLING VORTEX PROPERTIES

Abstract. Diastolic dysfunction (DD) can cause heart failure even under normal ejection fraction, which is called diastolic heart failure. By advancing diastolic dysfunction, the transmitral flow alters and causes an alteration in the flow pattern inside the left ventricle. We hypothesized that blood mixing, blood flow pattern, vortex ring strength, and transport flow characteristics would be optimal in normal transmitral flow compare to the inflow patterns correspond to diastolic dysfunction. We carefully chose six different transmitral flow from echocardiography of DD patients (2 for normal, 2 for Grade I, 1 for grade II, and 1 for Grade III) under three different physiological range of EDVs. A left heart simulator was used to run these six different inflows into the silicon model of the left ventricle. Fluid flow was quantified by two-dimensional time-resolved particle image velocimetry (2D TR-PIV). Horizontal and vertical momentum fluxes, vorticity field, flow transport, and vortex ring circulation were calculated using the velocity vector field. Results showed that compared to the corresponding DD inflows, the normal transmitral inflow had the most robust vortex ring during diastole, the highest value of momentum flux, and also more flow transport by calculation the Finite-Time Lyapunov Exponent (FTLE). Grade I showed that fluid flow during E-wave was not energetic enough to circulate the

blood inside the LV and even a high-flow-rate in A-wave with could not compensate for the role of E-wave in terms of propagation and circulation. Grade II and Grade III had similar flow patterns of the normal transmitral flow, but less impact. Understanding of flow behavior inside the LV under different transmitral inflow can help us to appreciate the properties of a vortex ring in diastolic dysfunction better.

Keywords: Diastolic dysfunction; left ventricle phantom; intraventricular filling vortex; vortex ring; momentum flux; Finite-Time Lyapunov Exponent (FTLE)

5.1. Introduction

Heart failure with diastolic left ventricular (LV) dysfunction with the presence of normal or slightly abnormal systolic function refers to heart failure with normal ejection fraction (HFNEF) (1,2). In HFNEF, the left ventricular ejection fraction (LVEF) is more than 50%, and up to 50% of heart failure patients are diagnosed with HFNEF (3). The pathological characterization of diastolic dysfunction (DD) is LV stiffening (4), which is mostly because of aging, hypertension, obesity, and diabetes. As a result, the LV pressure will be increased to compensate for the inability of the LV functionality in untwisting during early diastole (E-wave). Therefore, the LV stiffening alters the hemodynamic (blood pressure and flow) of the LV. The diastole phase consists of two stages in which the LV relaxes and untwists and sucks the blood flow into the LV from the left atrium (active filling). This stage refers to early filling (E-wave). In normal LV, 70% to 80% of the LV filling occurs in this stage. The rest of blood (20% to 30%) enters the LV by atrial contraction (A-wave). In the early stages of diastolic dysfunction, the LV reduces its ability to untwist in the early filling, and as a result the portion of E-wave diminishes, and the A-wave compensates the blood flow shortage (atrial kick). This stage refers to Grade I diastolic dysfunction or impaired relaxation. By progressing diastolic dysfunction, the high pressure in left atrium (LA) causes the blood flow pushes into the LV by LA rather than suction by negative

pressure in the LV. In this stage, the proportion of E-wave and A-wave becomes normal again; however, the systemic pressure is elevated. This stage of diastolic dysfunction is called Grade II or pseudonormal left ventricular filling. Further increase in LA pressure will result in an abrupt discharge of blood flow into the LV, which refers to a restrictive filling pattern. This stage is reversible (known as Grade III) with the Valsalva maneuver; however, it can become irreversible (Grade IV) by progressing the disease, which is the worsen stage of diastolic dysfunction.

There have been studies that investigated flow patterns inside the LV by *in vivo* approaches such as MRI or echocardiography (5-12), experimental methods as *in vitro* studies (13, 14), and numerical simulations (15-18). The great advantage of *in vitro* studies compare to *in vivo* is the high time and space resolution of experiments, in which the details of fluid mechanics can be investigated. To the best of our knowledge, there has not been an *in vitro* or computational study to investigate the flow pattern inside the LV at different grades of diastolic dysfunction.

This study aims to characterize the vortex ring properties within the left ventricle under different transmitral inflow corresponds to all different grades of diastolic dysfunction and compare to the normal LV inflow. The hemodynamic values of different grades of DD were extracted from echocardiography of real patients (1, 19-24) and simulated in an *in vitro* left heart simulator. Three different LV end-diastolic volume (EDV) was considered to cover the entire range of LV EDV corresponds to diastolic dysfunction. Two-dimensional particle image velocimetry (2D-PIV) was used to quantify the fluid flow in each model. The velocity, vorticity, and finite-time Lyapunov exponent (FTLE) fields, momentum flux, and vortex circulation strength were examined for all different inflows. More knowledge of fluid flow properties within the LV in different grades of diastolic dysfunction can help us to a better understanding of the blood flow pattern and behavior inside the LV in terms of mixing and flow transport during diastole.

5.2. Experimental method

We designed a set of experiments to investigate the effects of changing transmitral inflow on vortex ring properties in a left ventricular simulator under different stages of diastolic dysfunction.

5.2.1. **In vitro left heart simulator and PIV setup**

An in-vitro model of a left heart simulator was developed to investigate fluid flow in a silicon LV model (**Figure 5-1**). The LV model was cast and molded (VenAir, Terrassa-Barcelona, Spain) based on CMR data of healthy volunteers' LVs (25-27) as it is shown in **Figure 5-1**A. The thickness and shore hardness of the silicon model of the LV was 1.59 mm and 40A, respectively. The transparency of silicon lets us see through the LV during PIV. Before using the LV model in the loop, the passive stiffness of the LV was obtained by measuring the LV pressure change causing by increasing LV volume with increments of 10 mL. Three trials were conducted within the volume range of 105 to 150 mL and corresponding pressure range of 0 to 100 mm Hg using a pressure transducer (Utah Medical Products Inc., Midvale, UT; with a resolution of ± 0.1 mm Hg). At LV volume of 105 mL, the pressure difference between inside and outside of the LV was zero, which means LV volume = 105 mL corresponds to the LV dead volume, in which the LV was not under any tension or compression. LV pressure change was plotted versus LV volume change, and linear regression ($R^2 > 0.99$) was fitted to the data points to achieve the LV stiffness. To mimic the blood properties at body temperature ($\upsilon = 3.5$ cSt, and $\rho = 1080$ kg/m^3), we u sed water-glycerin (35% by volume of glycerin). A programmable pulsatile piston pump (PPP; Vivitro Systems Inc., Victoria, Canada) was used to push the flow into a sealed acrylic chamber. The LV silicon model was held in the chamber, and because of the piston movement, the flexible LV walls were moved actively and caused flow running inside the loop. Two bi-leaflet mechanical heart valves were positioned at mitral and aortic annulus to ensure a unidirectional flow during the cardiac cycle. Windkessel elements (compliance element and resistance) were

used in the loop to obtain physiological hemodynamics. The instantaneous inflow (Mitral flow rate) and outflow (Aortic flow rate) of the LV were measures by two ultrasonic flowmeters (Transonic Systems Inc., Ithaca, NY). Also, three pressure transducers were used to measure the chamber pressure, aortic pressure, LV pressure instantaneously.

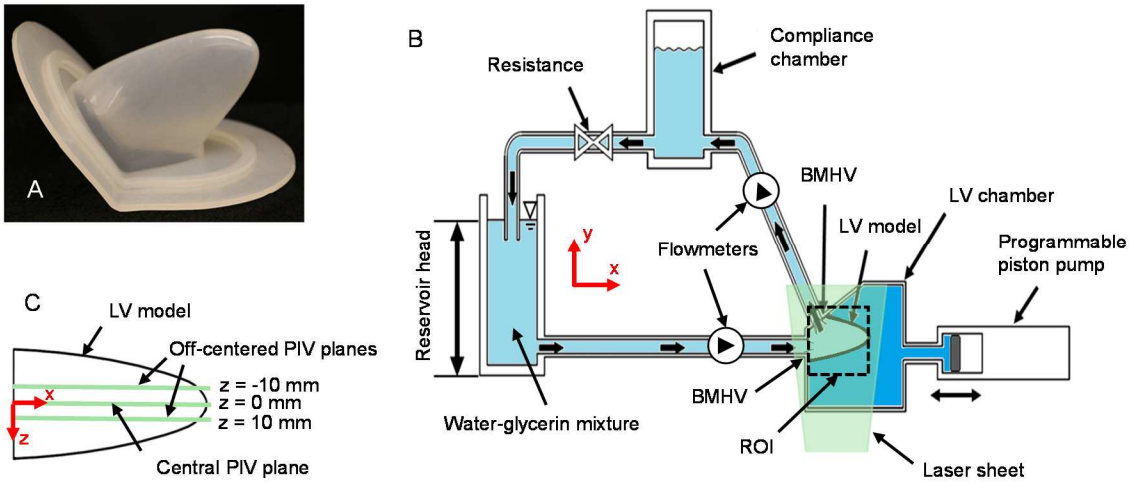

Figure 5-1: Left heart simulator experimental setup: A) left ventricle physical model, which was made from silicon; B) schematic of in vitro flow circuit of left heart simulator, and arrangement of PIV laser plane; the high-speed camera was perpendicular to this view and capturing the ROI; C) flow filed at three parallel PIV planes at z = -10 mm, z = 0 mm, and z = 10 mm were investigated (ROI = region of interest; BMHV = bi-leaflet mechanical heart valve).

5.2.2. **Test conditions**

We examined intraventricular flow corresponds to different grades of diastolic dysfunction (DD) along with a healthy diastolic function in the left heart simulator. Transmitral inflows correspond to healthy, and DD patients were chosen from echocardiogram datasets (1, 19-24, 28-31) and were replicated in the left heart simulator. **Figure 5-2** shows all the flow curves and corresponding LV volumes. In this study, we investigated the flow field in three different initial volume of the bag to cover the possible ranges of EDV in DD patients. We ended up with three different sets of EDVs (EDV = 110 mL, 145 mL, and 180 mL). From now on, we refer EDV = 110 mL as Low EDV, 145 mL as Normal EDV, and 180 mL as High EDV.

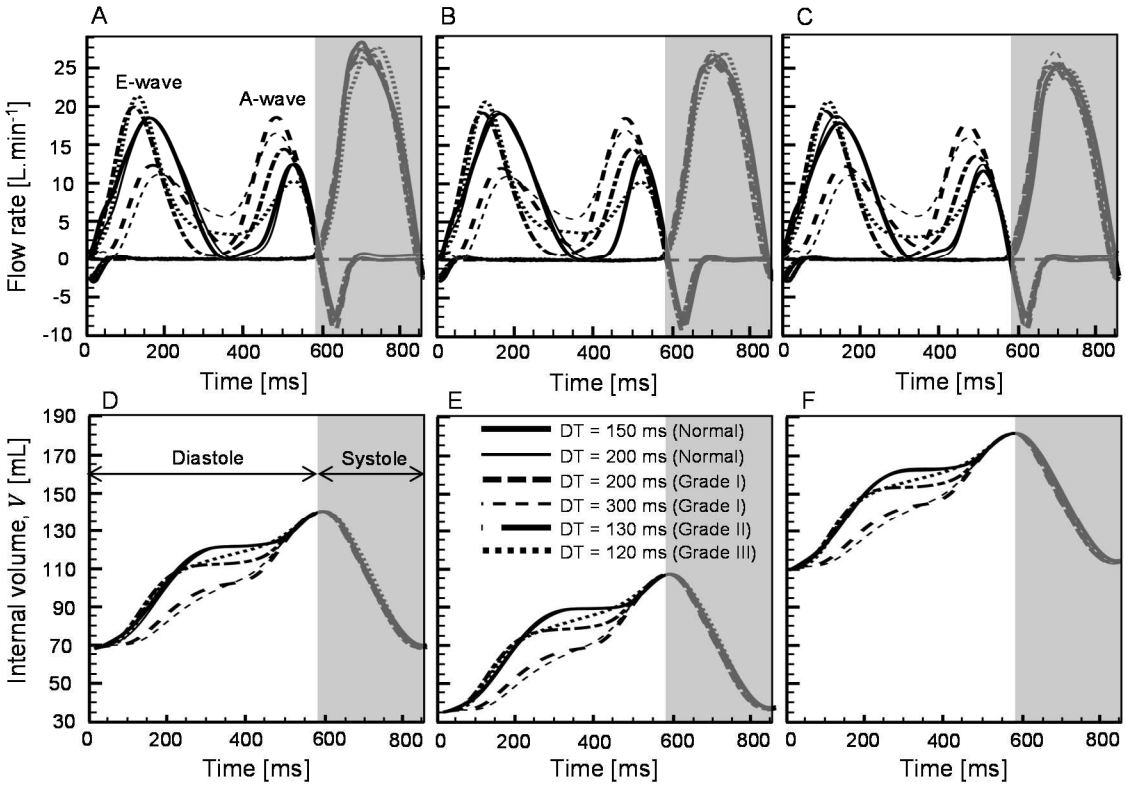

Figure 5-2. Hemodynamic curves for different grades of diastolic dysfunction. A, B, and C) Mitral and Aortic flow in a cardiac cycle for normal, low, and high EDVs, respectively. Each flow rate curve was an average of 15 cycles (SD < 0.2 L/min); D, E, and F) LV volume during a cardiac cycle for normal, low, and high EDVs, respectively. Time is the total cardiac cycle.

The detailed hemodynamic parameters of test conditions are tabulated in **Table 5-1**.

Table 5-1: Recorded hemodynamics for all test conditions (DT = deceleration time and AT = acceleration time). For all cases: heart rate = 70 bpm, cardiac output = 4.68±0.05 L/min, stroke volume = 67±0.5 mL/stroke, aortic pressure = 80/121± 3 mm Hg, peak aortic flow = 26.5±1 L/min

Transmitral flow	Peak E-wave [L/min]	DT [ms]	AT/DT	E/A ratio	VFT
Normal	17.8 ± 0.1	150 ± 3	1.03	1.41	4.32
Normal	17.8 ± 0.1	200 ± 4	0.76	1.40	4.24
Grade I	11.9 ± 0.1	220 ± 3	0.45	0.66	2.65
Grade I	10.8 ± 0.1	300 ± 4	0.37	0.67	2.68
Grade II	19.3 ± 0.1	130 ± 3	0.92	1.38	3.50
Grade III	20.7 ± 0.1	120 ± 3	0.98	2.24	3.54

The systolic phase and cardiac output were kept relatively unchanged for all six cases of different transmitral inflow. During experiments, we kept all the loop parameters constant across different sets of experiments, including resistance magnitude, compliance level, reservoir head, PPP amplitude, and frequency. The only parameter we changed across different sets of experiments the transmitral inflow by changing pump input waveform. We conducted our experiments on there different LV EDVs (low, normal, and high EDV). The vortex formation time (VFT) or formation number was also calculated based on Gharibs' study (32) as below to characterize vortex ring flow structures formed during intraventricular filling.

$$\mathrm{VFT} = \frac{4\,V_E}{\pi D_{MV}^3} \qquad \text{Eq. 5-1}$$

Where V_E is fluid volume, which is associated with early LV filling (E-wave) during the diastole phase. We did not consider the diastasis portion of the inflow for calculating the VFT values.

The Reynolds number was calculated based on peak mitral flow as below:

$$\mathrm{Re} = \frac{4\,Q_{max,MV}}{\pi\,\upsilon\,D_{MV}} \qquad \text{Eq. 5-2}$$

where υ, D_{MV}, and $Q_{max,\,MV}$ are the kinematic viscosity of the fluid, the diameter of the mitral annulus, and the peak mitral inflow rate (which could be based on E-wave or A-wave depending on Grade of DD), respectively. The range of Re was 2700 – 3000 across all different types of inflow.

5.2.3. **Two-dimensional particle image velocimetry (2D PIV)**

2D time-resolved particle image velocimetry (2D TR-PIV) was used to study the intraventricular flow (**Figure 5-1**B). A single cavity high-speed Nd: YLF laser (30 mJ/pulse at 1 kHz repetition rate; Photonics Industries International, Inc., NY, USA) was used to illuminate the central plane

of the LV longitudinally. A pair of converging-diverging lenses focused the laser beam, and a 90-degree right-angle mirror was used for having a desirable direction of the laser beam. A cylindrical lens (f = 10 mm) was used to transform the beam into a laser sheet. The nature of the generated vortex ring inside the LV during diastole is three dimensional. Therefore, three parallel planes (one central plane at z = 0 mm and two off-central planes at z = ± 10 mm) were chosen for flow visualization, as it is shown in **Figure 5-1C**. The fluid inside the LV was seeded by polymethyl methacrylate (PMMA) fluorescent particles with a diameter of 1-20 µm and 532 nm excitation, and 584 nm emission. A high-speed 1 MP CMOS camera (Phantom Miro 110, Vision Research Inc., Wayne, NJ, USA) was placed perpendicular to the laser plane. A 60 mm constant focal length lens (Nikon Micro Nikkor, Nikon Corporation, Tokyo, Japan) with a maximum aperture of 2.8 was used to focus on the illuminated particles. A 550 nm long-pass filter was attached to the lens to cut-off the unwanted wavelength of the particle illumination. The camera frame rate was set on 1800 frames per second with a resolution of 896×656 pixels. The pixel size was 134 microns. The camera and laser were triggered precisely at the starting time of diastole, and ten cardiac cycles were recorded for the entire diastole duration. Two hundred cardiac cycles were run before the PIV acquisition. DaVis 8.3.0 software (LaVision GmbH, Göttingen, Germany) was used to process raw PIV data. The fluid inside the LV model was seeded with fluorescent particles, and the number of counts after illumination was in the range of 110-420. The outside fluid was not seeded; however, few particles were visible in the outside of the LV with a number of counts less than 30. An algorithmic mask was used to process the fluid flow inside the LV model and not consider the outside fluid, such that the particles less than 40 counts were ignored. Multi-pass cross-correlation was considered with initial 64×64 pixels (2 passes) interrogation window to a final window size of 32×32 pixels with a 50% overlap. Also, the velocity vectors with a peak ratio of less than 1.2 were rejected in post-processing, and empty vectors were replaced instead. The averaged velocity components of 10 cycles were obtained in DaVis post-processing, and other parameters such as vorticity, circulation, and energy dissipation

were post-processed using custom scripts written in MATLAB (The Mathworks, Inc., Natick, MA).

5.2.4. **Definitions of calculated quantities**

5.2.4.1. Hemodynamic characteristics

Average cardiac output (CO) in units of L/min was calculated using the following equation:

$$\mathrm{CO} = \mathrm{SV} \times \mathrm{HR} \times 10^{-3} \qquad \text{Eq. 5-3}$$

Where SV is the stroke volume (in units of mL/beat), and HR is the heart rate (in units of beats/min).

5.2.4.2. Formation time

Laminar vortex rings have been investigated for a wide range of applications, and Garib et al. (33) introduced formation time as a non-dimensional parameter, which is defined as follows:

$$T^{*} = \frac{\bar{U}\, t}{D_{MV}} \qquad \text{Eq. 5-4}$$

where t is time during diastole, D_{MV} is Mitral annulus diameter, and $\bar{U}$ is averaged velocity during diastole and is calculated as below:

$$\bar{U} = \frac{4}{\pi T {D_{MV}}^{2}} \int_{0}^{T} Q(t)\, dt \qquad \text{Eq. 5-5}$$

where T is the total duration of diastole and Q(t) is instantaneous Mitral flow during diastole.

5.2.4.3. Vorticity

Physical description of vorticity is the tendency of a fluid to rotate and it is mathematically defined as the curl of a velocity field $\vec{V}$.

The out-of-plane z-vorticity field (ω_z) was calculated from PIV-based 2D velocity vector field (u, v) and it was calculated in Tecplot 360 (Tecplot, Inc., Belleview, WA, USA) using the following equation:

$$\omega_z = \nabla \times \vec{V} = \frac{\partial v}{\partial x} - \frac{\partial u}{\partial y} \qquad \text{Eq. 5-6}$$

The x and y components of the velocity field are defined as u and v.

5.2.4.4. Vortex identification and circulation

The intraventricular filling vortex ring is a three-dimensional donut-shaped flow structure. In the case of 2D visualization of the flow (as in the current study), only a cross-section of the 3D flow structure can be observed, and it appears in the form of two counter-rotating vortices. The counterclockwise vortex proximal to the aorta was identified from the processed PIV data using the swirling strength criterion (34), which is defined as the imaginary part of the complex eigenvalue of the velocity gradient tensor:

$$\lambda_{ci} = \mathrm{Im}[\mathrm{eig}(\nabla u)] = \frac{1}{2}\,\mathrm{Im}\left[\sqrt{\left(\frac{du}{dx} - \frac{dv}{dy}\right)^2 + 4\frac{du}{dy}.\frac{dv}{dx}}\right] \qquad \text{Eq. 5-7}$$

The iso-surfaces of λci were normalized by 2.6% of the maximum value, as recommended in previous studies (35).

To quantify the strength of the intraventricular filling vortex, circulation Γ (in units of m2/s) was calculated by integrating the out-of-plane z-vorticity, ωz, over the surface area enclosed by the vortex A, as:

$$\Gamma = \iint_A \omega_z \, dA = \sum_A (\omega_z \, dx \, dy) \qquad \text{Eq. 5-8}$$

Circulation provides a large-scale estimate of the rotational strength of a vortex. Previous studies of intraventricular filling have examined this quantity using 2D PIV in physical models (26, 36), echocardiographic-PIV (37), and phase-contrast CMR imaging (35).

The automated algorithm to calculate circulation strength for a specific case at a specific time point was as follows:

a) identify the center of the maximum vorticity (vortex ring core) based on λci criteria.

b) calculate circulation strength, Γ_1, within a square with a size of a×a (a = 3 mm in this study).

c) calculate circulation strength, Γ_2, within a square with a size of (a+b)×(a+b) (b = 2 mm in this study).

d) compare Γ_1 and Γ_2. If $\Gamma_1 = \Gamma_2$, we store the value. Otherwise, Γ_1 was calculated within a bigger square with a size of (a+b/2)×(a+b/2) and Γ_2 was calculated within a bigger square with a size of (a+3b/2)×(a+3b/2) and compare Γ_1 and Γ_2 again until Γ_2 become equal to Γ_1.

5.2.4.5. Momentum flux

To quantify the momentum flux during diastole within an LV, we calculated cycle-averaged momentum fluxes per unit width. We used the below equations to calculate horizontal (parallel to the inflow jet) and vertical (normal to the flow direction) momentum fluxes as HMF and VMF, respectively.

$$\mathrm{HMF} = \rho \int |\bar{u}(x,y)|(\bar{U}.\hat{n})dy \qquad \text{Eq. 5-9}$$

and

$$VMF = \rho \int |\bar{v}(x,y)|(\bar{U}.\hat{n})dx, \qquad \text{Eq. 5-10}$$

where $\bar{U} = \bar{u}i + \bar{v}j$ and $\hat{n}$ is the unit normal vector. Therefore, $\hat{n}$ = i for HMF and $\hat{n}$ = j for VMF. The HMF demonstrates the horizontal component of time-averaged momentum flux at x-positions across the corresponding vertical lines. Similarly, VMF shows the vertical component of time-averaged momentum flux at y-positions across the corresponding horizontal lines.

5.2.4.6. Finite-Time Lyapunov Exponent (FTLE)

The amount of elongation over a time interval about a trajectory of a point can be characterized as finite-time Lyapunov exponent, FTLE. Therefore, FTLE is a scaler, which is a function of time and space. It is important to note that FTLE is not an instantaneous value and it is calculated by integration over a time interval. The FTLE shows the transport behavior since it is driven by flow particle trajectories and demonstrates the integrated effect of the fluid flow. The outcome of FTLE plots in time and space is similar to dye visualization (38, 39). We used a MATLAB script to calculate and plot the FTLE values in time and space from phase-averaged velocity fields (38).

5.3. Results and Discussions

5.3.1. **Velocity validation**

The measured blood velocity by Doppler echocardiography is based on blood velocity inside the left ventricle. Therefore, it is essential to validate the velocity inside the LV (from PIV) with the measured velocity in the mitral annulus (by flow meter). The maximum value of the horizontal velocity component at x = 4 mm was plotted in **Figure 5-3** for all different grades of diastolic dysfunction (dashed lines), which were extracted from velocity fields from PIV processed data

and compared to the corresponding velocities, which were already measured in mitral annulus by the flow meter (solid lines). The velocity in the mitral annulus, V_m, was calculated based on mitral diameter (D_{MV} = 25.4 mm) and mitral instantaneous flow rate, Q_M, as below:

$$V_m = \frac{4Q_M}{\pi D_{MV}^2} \qquad \text{Eq. 5-11}$$

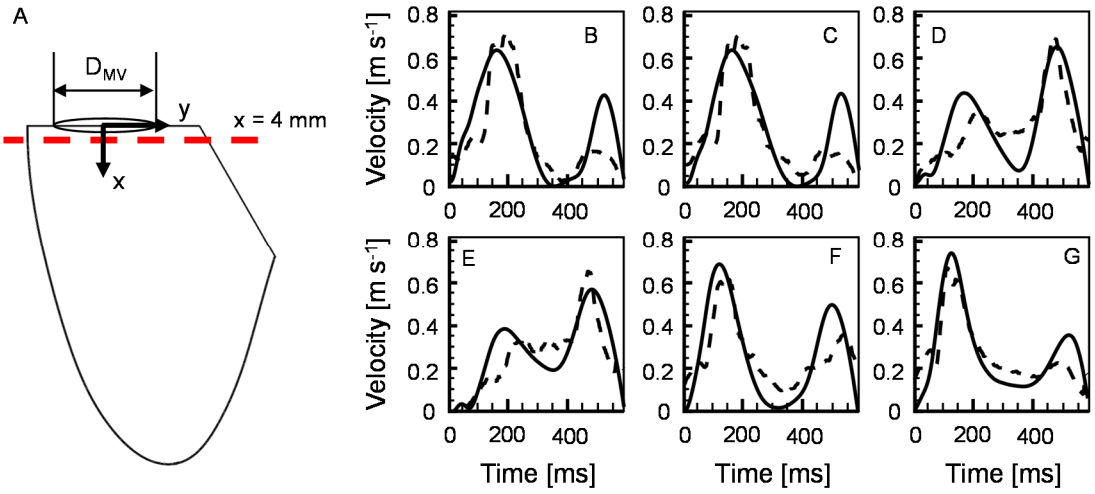

Figure 5-3. The maximum horizontal velocity component at x = 4 mm from PIV processed data. A) the location of extracted velocity profiles. All the extracted transmitral flows (dashed lines) were compared with measured velocity by the flow meter (solid lines). B) DT = 150 ms (Normal); C) DT = 200 ms (Normal); D) DT = 220 ms (Grade I); E) DT = 300 ms (Grade I); F) DT = 130 ms (Grade II); G) DT = 120 ms (Grade III).

The extracted velocities from the PIV were similar to those measured by flow meter. The difference between the two approaches was not unexpected, and the source of error could be the inadequate spatial resolution and PIV uncertainty.

5.3.2. **Velocity vectors and vorticity contours**

Velocity fields (u(x,y,t) and v(x,y,t)) were calculated by processing raw PIV images in DaVis. The vorticity contours were also calculated in Tecplot using velocity fields. Velocity vector fields overlayed on the out-of-plane z-vorticity contours and were plotted in **Figure 5-4** and **Figure 5-5**

for E-wave and A-wave, respectively, for normal-EDV. The boundary of the LV geometry was moving during diastole, and it is shown in **Figure 5-4** and **Figure 5-5**.

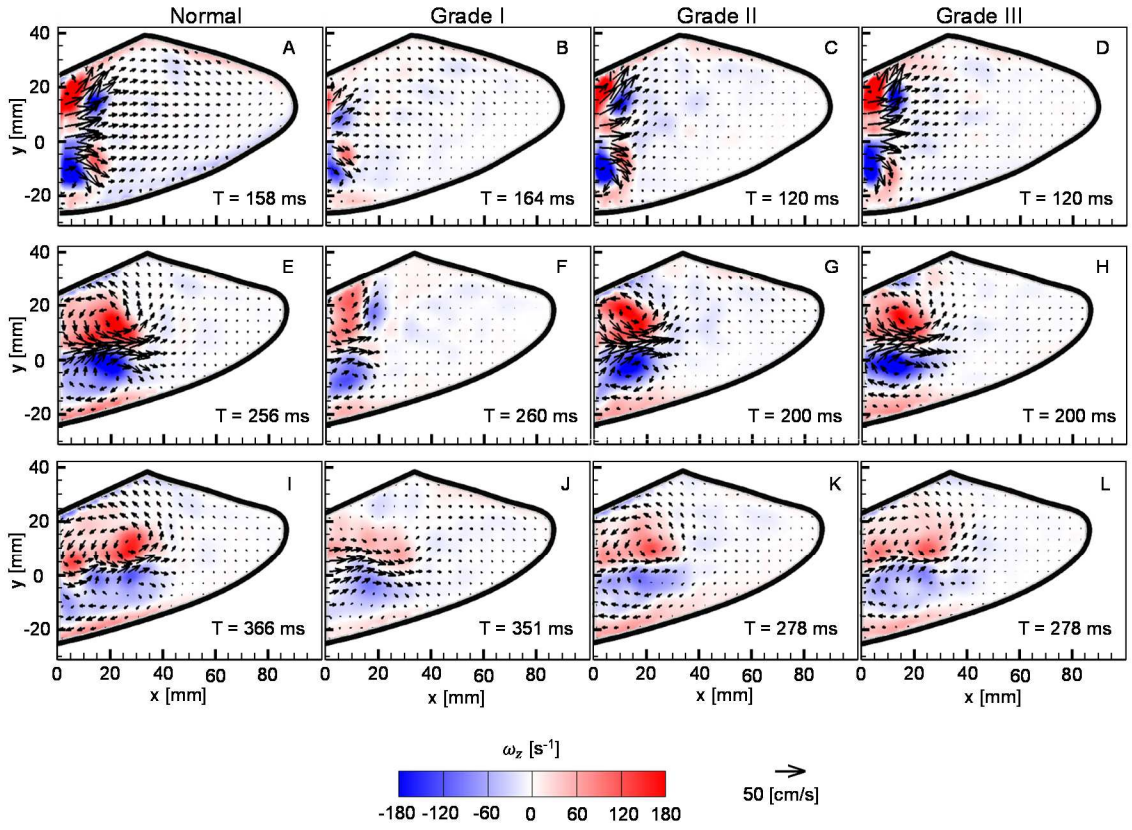

Figure 5-4. Velocity vector fields overlayed on out-of-plane vorticity contours during E-wave for normal-EDV. The first column represents the normal transmitral inflow, whereas the second, third, and fourth columns show different grades of diastolic dysfunction as Grade I, Grade II, and Grade III, respectively. Each row corresponds to a specific time point. A-D) peak E-wave; E-H) halfway of the deceleration time during E-wave; I-L) end of E-wave.

As a general trend, a vortex ring was generated inside the LV during diastole. Depending on the transmitral inflow, this vortex ring was energetic or weak. The normal transmitral flow shows a strong vortex ring, which was created at peak E-wave, and it was elongated through the center of the LV (**Figure 5-4E**). At the end of the E-wave, a relatively stable vortex ring has still existed (**Figure 5-4I**). The first grade of DD (impaired relaxation, Grade I) did not show a sturdy vortex ring during E-wave since the E-wave mitral inflow was less energetic compared to the normal inflow. At the end of the E-wave, there was existed a continuous inflow (**Figure 5-4J**) and a

weak and stretched vortex ring, which was because of long deceleration time (DT) in Grade I diastolic dysfunction. It seems higher DT helps the vortex ring to decay slower; however, it needs to be investigated and quantified by calculating and plotting the circulation strength of vortex rings. Grade II and Grade III show relatively smaller vortex cores compare to the normal case.

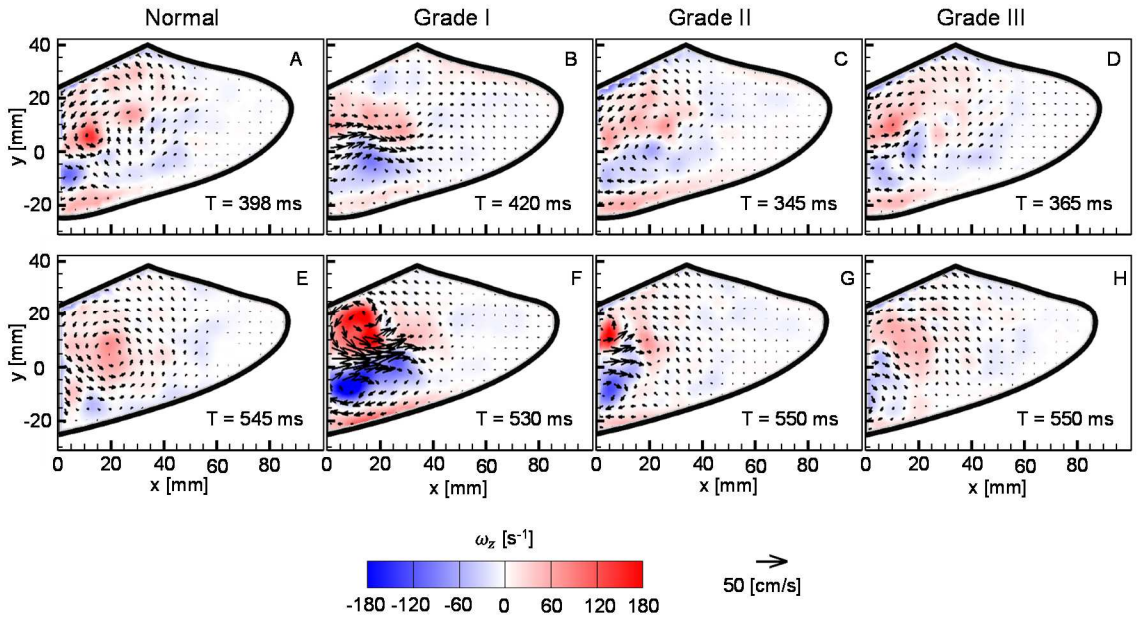

Figure 5-5. Velocity vector fields overlayed on out-of-plane vorticity contours during A-wave. The first column represents the normal transmitral inflow, whereas the second, third, and fourth columns show different grades of diastolic dysfunction as Grade I, Grade II, and Grade III, respectively. Each row corresponds to a specific time point. A) halfway of diastasis; B) halfway of the acceleration time during A-wave; C, D) halfway of diastasis; E-H) peak A-wave.

Normal, Grade II, and Grade III transmitral flows had somewhat similar flow fields during A-wave; however, the normal case shows a dominant rotational flow at peak A-wave (**Figure 5-5E**) compare to Grade II and Grade III. Grade II has a distinguishable vortex ring because of A-wave flow (**Figure 5-5G**) since the diastasis was longer in Grade II mitral flow compare to the normal case. The vortex ring in Grade I was still stable in early A-wave (**Figure 5-5B**), and continuous flow is noticeable; however, the vortex ring was weak. At peak A-wave, a strong vortex ring was entered into the LV in Grade I (**Figure 5-5F**), however, it could not help to circulate fluid inside the LV since it happened almost at the end of the diastole and less than 100 ms after that the fluid

flow was pumped from the LV. The fluid transportation plots (FTLE) can help to better understanding.

5.3.3. **Momentum fluxes**

The direction and location of generated forces in the fluid flow were calculated by horizontal and vertical momentum fluxes and are plotted for different transmitral flows under different EDVs (**Figure 5-6**). Each plot is an average of 10 cycles, and each point is the average of the entire diastole. In most of the data points in HMF values, the standard deviations were smaller than the size of the markers, and they are not visible. The peak value for HMF happens just after the mitral annulus, and it decayed by propagating toward the LV apex. The amount of propagation was slightly higher for the case with normal transmitral inflow. The average values of HMF were 5-10 times higher than the average values of VMF, which is rational and means the fluid flow tendency is mainly through the apex of the LV. Under normal LV EDV, the HMF and VMF values were higher for the normal transmitral flow, and the Grade I had the lowest values (**Figure 5-6A** and **Figure 5-6B**), and Grade II and Grade III were in-between. That means the generated force by the normal inflow was higher than the force corresponds to the diastolic dysfunction. There is a small bump in the HMF values at x ~ 30 mm. Based on the velocity of the inflow jet, we can justify that this little bump in the HMF was because of A-wave in the inflow, which reenergized the fluid flow.

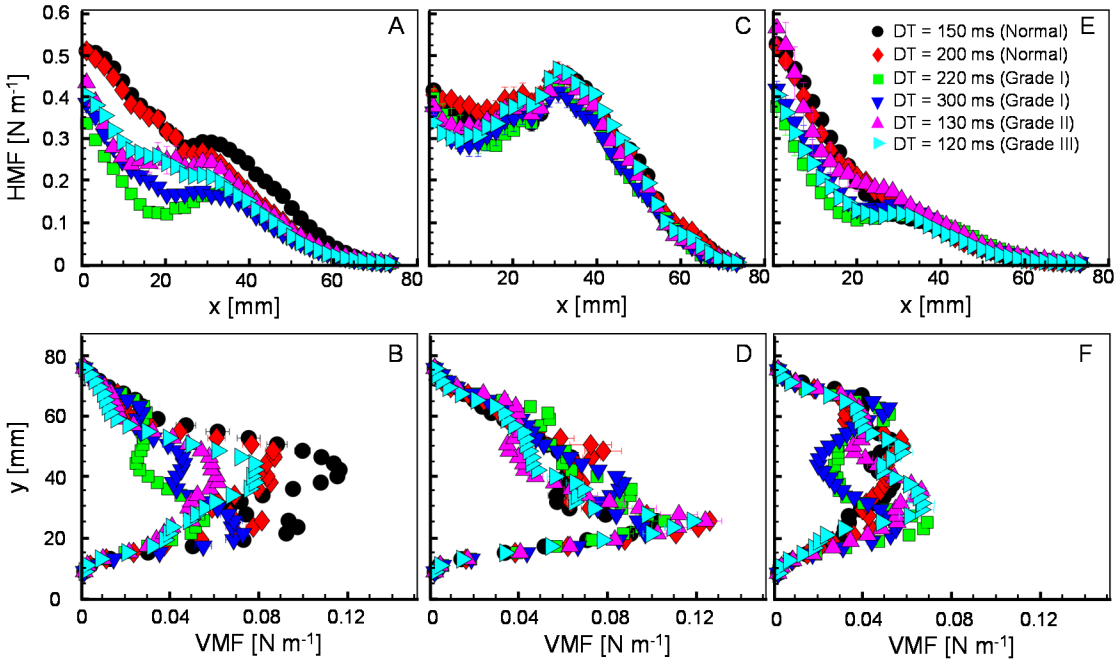

Figure 5-6. Time-averaged momentum fluxes as a function of transmitral inflow. The first and second rows show HMF and VMF, respectively, for different EDVs. A, B) normal-EDV; C, D) low-EDV; E, F) high-EDV.

By lowering the EDV (**Figure 5-6C** and **Figure 5-6D**), the HMF peak value was reduced for all of the cases since the lower EDV of the LV has restricted the flow just in the base of the LV (mitral annulus). In contrast, the VMF was increased in the low-EDV condition of the LV. Unlike the normal-EDV case, the fluid HMF did not drop after entering the into the LV up to x ~ 40 mm. The reason was because of having higher values of velocity (momentum flux is proportional to the square of velocity) inside a smaller and more confined LV cavity compare to the normal-EDV. Similar to the normal-EDV, the normal inflow shows higher values of HMF in low-EDV. Also, it is noticeable that the second bump has higher significance, and it shows that in lower EDVs, the A-wave plays an essential role in giving momentum to the flow.

Overall, at high-EDV, all values of momentum fluxes (**Figure 5-6E** and **Figure 5-6F**) show higher peak values for HMF, and lower peak values for VMF compare to the normal-EDV. The values of HMF for Grade III was similar to the normal transmitral flow. Grade I has lower values

in both HMF and VMF compare to the rest of the transmitral inflows. The values of HMF decelerated faster by propagating into the LV cavity.

As a general trend, by increasing the EDV, the peak value of HMF was elevated, which happens in the entrance (mitral annulus, x = 0 mm). However, the HMF decelerated faster for higher EDVs. Also, the peak VMF was decreased by increasing EDVs. To quantify that how much the flow was energetic inside the LV model, it is necessary to calculate the summation of momentum fluxes of all locations in a specific direction (horizontal at and vertical) and find the total momentum flux. **Figure 5-7** shows the total momentum flux in horizontal and vertical directions for each case of transmitral inflow at different LV EDVs.

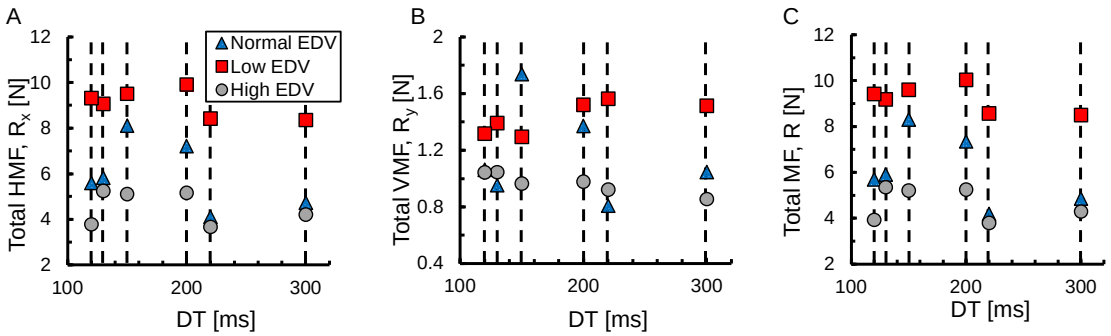

Figure 5-7. Total momentum flux versus deceleration time (DT). The integration of HMF and VMF over x and y, respectively, provided the total momentum flux in horizontal and vertical directions.

The total momentum flux had the highest value for the normal transmitral flow (DT = 150 ms) in the normal LV EDV, and Grade I (DT = 220 ms) had the lowest value of total MF. A similar trend was observed in the other two EDVs (**Figure 5-7C**). By increasing the EDV, the total MF was decreased, unlike the peak HMF, which was increased by increasing the EDV, as shown in **Figure 5-6**. The reason for this observation was because of alterations in fluid flow distribution by changing EDV. The jet was more concentric in high-EDV, and the fluid particle velocities were minimal near the walls since the LV model was inflated more than usual and the cross-section of the LV was more circular-shaped during diastole. Because of that, the total momentum

flux (which is proportional to v^2) was small in high-EDV. Unlike the high-EDV case, the fluid flow was more dispersed in the low-EDV case since the LV model was squeezed because of a low amount of fluid inside that, and the 2D-PIV-shape of the LV was flatter during diastole (more oval-shaped LV cross-section instead of circular-shape). As a result, the total applied force to the LV according to the transmitral inflow was lowering by increasing the LV EDV.

5.3.4. **FTLE fields**

The Finite-time Lyapunov exponent (FTLE) fields were computed (38) from the velocity field at four different time points (peak E-wave, end of the E-wave, peak A-wave, and end of the A-wave) with an integration time of 10 ms. **Figure 5-8** shows the FTLE fields for different diastolic dysfunction under normal-EDV at four selected time points. FTLE shows the maximum trajectories of a particle at a given time over a finite time interval. The physical analogy of FTLE can be represented by dye visualization and can characterize fluid transport into the LV. At peak E-wave, the normal inflow had concentric and robust vortex cores compare to the DD inflows (**Figure 5-8A-D**). Due to the low mitral flow rate in Grade I during E-wave, fluid flow had a minimal penetration into the LV (**Figure 5-8B** and **Figure 5-8F**). At the end of the E-wave, the fluid flow was reached almost 60% of axial direction ($x \sim 60$ mm) in the normal inflow case (**Figure 5-8E**). In contrast, **Figure 5-8G** and **Figure 5-8H** showed Grade II and Grade III did not demonstrate a lot of penetration ($x < 40$ mm). At peak A-wave, Grade I displayed a large amount of fluid flow transported into the LV (**Figure 5-8J**), which was continued up until the end of the A-wave (**Figure 5-8N**). During the A-wave we did not see a noticeable flow transport in normal and Grade III transmitral flow; however, Grade II showed a visible flow transport in A-wave, and it was because of the long duration of diastasis in Grade II transmitral inflow.

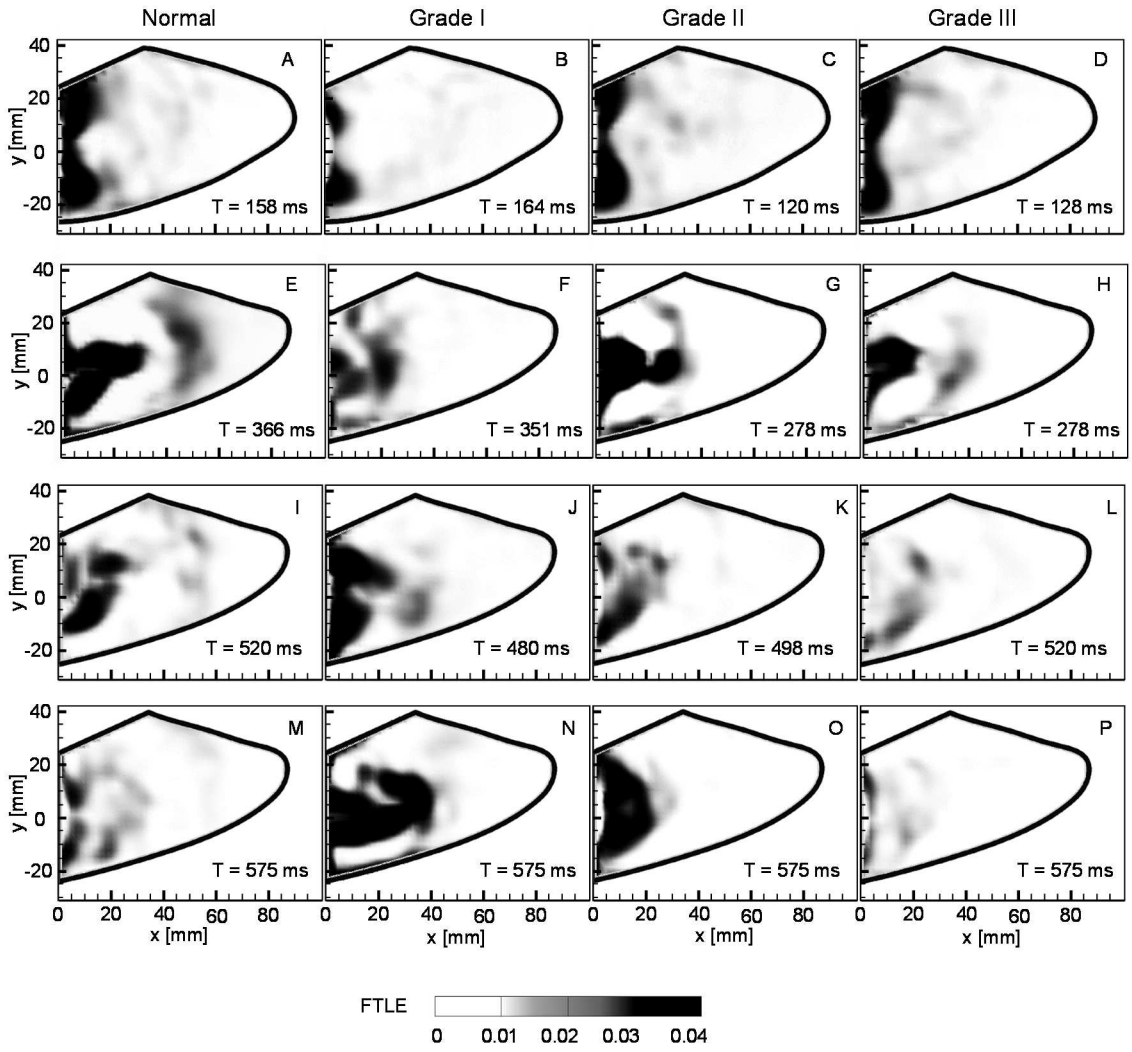

Figure 5-8. FTLE fields for different grades of diastolic dysfunction for normal-EDV. The first column represents the normal transmitral inflow, whereas the second, third, and fourth columns show different Grades of diastolic dysfunction as Grade I, Grade II, and Grade III, respectively. Each row corresponds to a specific time point. A-D) peak E-wave; E-H) end of E-wave; I-L) peak A-wave; M-P) end of A-wave.

Overall, E-wave played an essential role in carrying the fluid flow into the LV in normal, Grade II, and Grade III inflows; in contrast, A-wave was pushing the majority of fluid flow into the LV in Grade I diastolic dysfunction. However, the impact of A-wave in Grade I was not as effective as E-wave in normal inflow for transferring and penetrating flow into the LV. The flow transport associated with Grade III had the lowest efficiency.

5.3.5. **Vortex circulation**

The leading generated vortex cores (the vortex ring corresponding to the E-wave) in the centered PIV plane of the LV were tracked, and the vortex ring circulation strengths for all transmitral inflows in three different EDVs were calculated. The vortex ring circulation strengths in normal EDV was plotted versus time in **Figure 5-9A**. The circulation values were normalized by peak circulation, Γ_0, and plotted versus non-dimensional timescale (formation time), $T^* = \frac{U_{ave}t}{D_0}$, for all EDVs and displays in **Figure 5-9B-D**. Positive and negative values of circulation are corresponded to CCW and CW vortex cores, respectively.

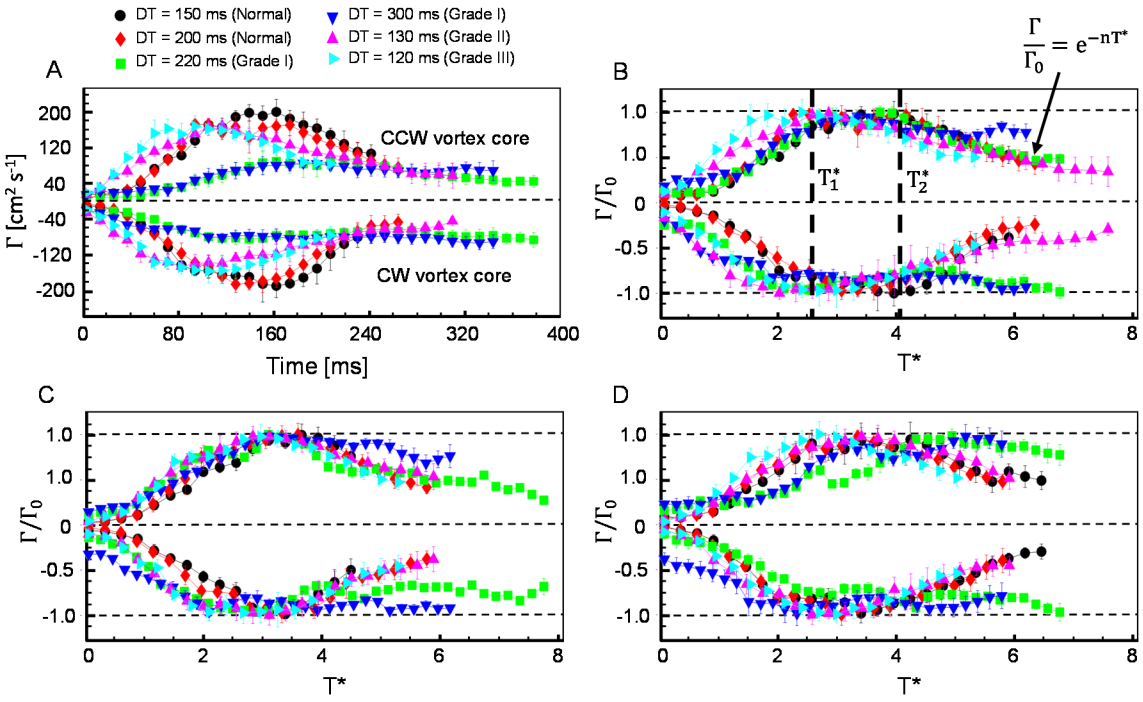

Figure 5-9. Vortex ring circulation for different grades of diastolic dysfunction. A) Dimensional circulation versus time for the normal-EDV case. B-D) Normalized circulation versus non-dimensional time $T^* = \frac{U_{ave}t}{D_0}$ for normal-EDV, low-EDV, and high-EDV, respectively. T_1^* and T_2^* are the corresponding time to onset of vortex ring pinch-off and vortex ring decay, respectively.

The vortex ring circulation gained the highest value for normal transmitral inflow compare to the rest of diastolic dysfunction inflows and was the lowest for Grade I. Detailed values of peak circulations for all transmitral inflow conditions under different EDVs are tabulated in **Table 5-2**.

In normal EDV, all the circulation curves were pinched off at $T_1^* \sim 2.6 \pm 0.3$, and the decay time was $T_2^* \sim 4.1 \pm 0.2$. A similar trend was captured in the other two EDVs. The gained circulation strength of vortex ring in Grade I was deficient compared to the rest of the inflow cases since Grade I had lower peak E-wave and also higher deceleration time.

Table 5-2. Peak circulation, Γ_{max}, and normalized peak circulation relative to the peak circulation corresponds to the normal mitral flow under normal-EDV ($\Gamma_{max}/\Gamma_{max,\text{Normal inflow and normal EDV}}$).

Transmitral flow	Vortex core rotation	Γ_{max} $[cm^2.s^{-1}]$			$\Gamma_{max}/\Gamma_{max,\text{Normal}}$ inflow (DT=150) and normal EDV		
		Normal EDV	Low EDV	High EDV	Normal EDV	Low EDV	High EDV
DT = 150 ms (Normal)	CCW	203±28	191±23	184±13	1.00	0.94±0.02	0.91±0.06
	CW	189±29	188±9	199±20	1.00	1.01±0.08	1.06±0.06
DT = 200 ms (Normal)	CCW	174±12	179±23	167±34	0.86±0.06	0.88±0.01	0.82±0.06
	CW	184±18	174±20	192±22	0.98±0.05	0.93±0.04	1.02±0.04
DT = 220 ms (Grade I)	CCW	91±22	97±7	59±9	0.44±0.05	0.48±0.03	0.29±0.01
	CW	83±11	77±11	85±10	0.44±0.01	0.41±0.01	0.45±0.02
DT = 300 ms (Grade I)	CCW	83±14	81±10	55±8	0.41±0.01	0.39±0.03	0.27±0.01
	CW	83±9	71±17	54±11	0.44±0.02	0.37±0.03	0.28±0.01
DT = 130 ms (Grade II)	CCW	171±12	150±17	153±23	0.85±0.06	0.74±0.02	0.75±0.01
	CW	146±15	147±16	168±18	0.78±0.04	0.78±0.04	0.90±0.04
DT = 120 ms (Grade III)	CCW	171±24	166±22	162±23	0.84±0.01	0.82±0.01	0.80±0.01
	CW	155±26	143±17	167±14	0.82±0.01	0.76±0.03	0.89±0.06

We considered the CCW vortex core for calculating the vortex circulation decay as it is displayed in **Figure 5-10**. The highest rate of decay belonged to the normal transmitral inflow, and by increasing DT (as of Grade I diastolic dysfunction), the decay rate was decreased. All the EDVs showed a similar trend; however, in general, the rate of circulation decay was reduced by increasing the LV EDV.

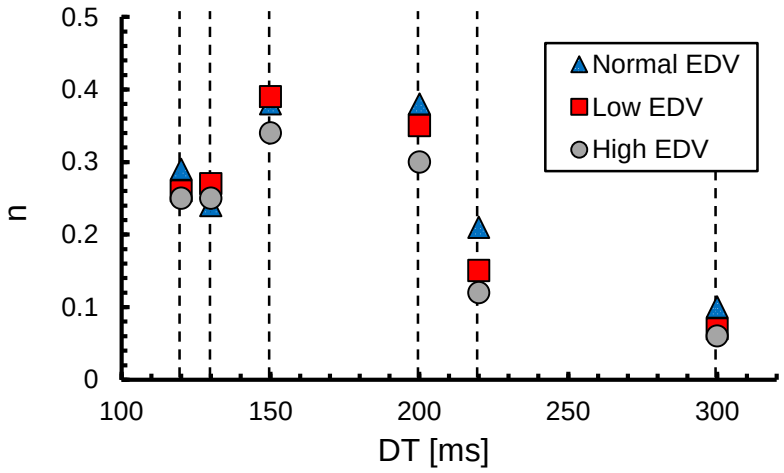

Figure 5-10. CCW circulation decay rate as a function of deceleration time (DT) for different EDVs. The decay rate was obtained from linear regression of plots of $\ln(\Gamma/\Gamma_0)$ versus T^* so that $\Gamma/\Gamma_0 = e^{-nT^*}$, where n is the best-fit linear slope. $\frac{d}{dT^*}(\Gamma/\Gamma_0)$ is the time rate of decay of normalized circulation, and this is proportional to n. For the entire test conditions, $0.921 < R^2 < 0.995$ and $3.2 \times 10^{-12} <$ p-value $< 5.4 \times 10^{-8}$.

The rate of decay was indeed higher for the normal transmitral flow, but to conclude which inflow had the most efficiency, we should also consider the other parameters such as peak circulation, momentum flux, FTLE, and velocity fields.

5.4. References

1. Leong, Darryl P., Carmine G. De Pasquale, and Joseph B. Selvanayagam. "Heart failure with normal ejection fraction: the complementary roles of echocardiography and CMR imaging." *JACC: Cardiovascular Imaging* 3.4 (2010): 409-420..

2. Paulus, W. J., Tschöpe, C., Sanderson, J. E., Rusconi, C., Flachskampf, F. A., Rademakers, F. E., ... & Borbély, A. (2007). How to diagnose diastolic heart failure: a consensus statement on the diagnosis of heart failure with normal left ventricular ejection fraction by the Heart Failure and Echocardiography Associations of the European Society of Cardiology. *European heart journal*, *28*(20), 2539-2550.

3. Owan, T. E., Hodge, D. O., Herges, R. M., Jacobsen, S. J., Roger, V. L., & Redfield, M. M. (2006). Trends in prevalence and outcome of heart failure with preserved ejection fraction. *New England Journal of Medicine*, *355*(3), 251-259.

4. Westermann, D., Kasner, M., Steendijk, P., Spillmann, F., Riad, A., Weitmann, K., ... & Tschope, C. (2008). Role of left ventricular stiffness in heart failure with normal ejection fraction. *Circulation*, *117*(16), 2051.

5. Garcia, M. J., Thomas, J. D., & Klein, A. L. (1998). New Doppler echocardiographic applications for the study of diastolic function. *Journal of the American College of Cardiology*, *32*(4), 865-875.

6. Garcia, D., del Álamo, J. C., Tanné, D., Yotti, R., Cortina, C., Bertrand, É., ... & Bermejo, J. (2010). Two-dimensional intraventricular flow mapping by digital processing conventional color-Doppler echocardiography images. *IEEE transactions on medical imaging*, *29*(10), 1701-1713.

7. Hong, G. R., Pedrizzetti, G., Tonti, G., Li, P., Wei, Z., Kim, J. K., ... & Narula, J. (2008). Characterization and quantification of vortex flow in the human left ventricle by contrast echocardiography using vector particle image velocimetry. *JACC: Cardiovascular Imaging*, *1*(6), 705-717.

8. Kheradvar, A., Rickers, C., Morisawa, D., Kim, M., Hong, G. R., & Pedrizzetti, G. (2019). Diagnostic and prognostic significance of cardiovascular vortex formation. *Journal of cardiology*.

9. Kilner, P. J., Yang, G. Z., Wilkes, A. J., Mohiaddin, R. H., Firmin, D. N., & Yacoub, M. H. (2000). Asymmetric redirection of flow through the heart. *Nature*, *404*(6779), 759.

10. Eriksson, J., Dyverfeldt, P., Engvall, J., Bolger, A. F., Ebbers, T., & Carlhäll, C. J. (2011). Quantification of presystolic blood flow organization and energetics in the human left

ventricle. *American Journal of Physiology-Heart and Circulatory Physiology*, *300*(6), H2135-H2141.

11. Bolger, A. F., Heiberg, E., Karlsson, M., Wigström, L., Engvall, J., Sigfridsson, A., ... & Wranne, B. (2007). Transit of blood flow through the human left ventricle mapped by cardiovascular magnetic resonance. *Journal of Cardiovascular Magnetic Resonance*, *9*(5), 741-747.

12. Carlhäll, C. J., & Bolger, A. (2010). Passing strange: flow in the failing ventricle. *Circulation: Heart Failure*, *3*(2), 326-331.

13. Domenichini, F., Querzoli, G., Cenedese, A., & Pedrizzetti, G. (2007). Combined experimental and numerical analysis of the flow structure into the left ventricle. *Journal of biomechanics*, *40*(9), 1988-1994.

14. Querzoli, G., Fortini, S., & Cenedese, A. (2010). Effect of the prosthetic mitral valve on vortex dynamics and turbulence of the left ventricular flow. *Physics of fluids*, *22*(4), 041901.

15. Seo, J. H., & Mittal, R. (2013). Effect of diastolic flow patterns on the function of the left ventricle. *Physics of Fluids*, *25*(11), 110801.

16. Domenichini, F., Pedrizzetti, G., & Baccani, B. (2005). Three-dimensional filling flow into a model left ventricle. *Journal of Fluid Mechanics*, *539*, 179-198.

17. Sohn, D. W. (2011). Heart failure due to abnormal filling function of the heart. *Journal of cardiology*, *57*(2), 148-159.

18. Saber, N. R., Gosman, A. D., Wood, N. B., Kilner, P. J., Charrier, C. L., & Firmin, D. N. (2001). Computational flow modeling of the left ventricle based on in vivo MRI data: initial experience. *Annals of biomedical engineering*, *29*(4), 275-283.

19. Galderisi, M. (2005). Diastolic dysfunction and diastolic heart failure: diagnostic, prognostic and therapeutic aspects. *Cardiovascular ultrasound*, *3*(1), 9.

20. Tschope, C., & Paulus, W. J. (2009). Echocardiographic evaluation of diastolic function can be used to guide clinical care (response to little and oh).

21. Nagueh, S. F., Appleton, C. P., Gillebert, T. C., Marino, P. N., Oh, J. K., Smiseth, O. A., ... & Evangelisa, A. (2009). Recommendations for the evaluation of left ventricular diastolic function by echocardiography. *European Journal of Echocardiography*, *10*(2), 165-193.

22. Zhang, H., Otsuji, Y., Matsukida, K., Hamasaki, S., Yoshifuku, S., Kumanohoso, T., ... & Tei, C. (2002). Noninvasive differentiation of normal from pseudonormal/restrictive mitral flow using TEI index combining systolic and diastolic function. *Circulation journal*, *66*(9), 831-836.

23. Sohn, D. W. (2011). Heart failure due to abnormal filling function of the heart. *Journal of cardiology*, *57*(2), 148-159.

24. Castelvecchio, S., Menicanti, L., Ranucci, M., & Di Donato, M. (2008). Impact of surgical ventricular restoration on diastolic function: implications of shape and residual ventricular size. *The Annals of thoracic surgery*, *86*(6), 1849-1854.

25. Okafor, I. U., Santhanakrishnan, A., Chaffins, B. D., Mirabella, L., Oshinski, J. N., & Yoganathan, A. P. (2015). Cardiovascular magnetic resonance compatible physical model of the left ventricle for multi-modality characterization of wall motion and hemodynamics. *Journal of Cardiovascular Magnetic Resonance*, *17*(1), 51.

26. Okafor, I. U., Santhanakrishnan, A., Raghav, V. S., & Yoganathan, A. P. (2015). Role of mitral annulus diastolic geometry on intraventricular filling dynamics. *Journal of biomechanical engineering*, *137*(12), 121007.

27. Santhanakrishnan, A., Okafor, I., Kumar, G., & Yoganathan, A. P. (2016). Atrial systole enhances intraventricular filling flow propagation during increasing heart rate. *Journal of biomechanics*, *49*(4), 618-623.

28. Nagueh, S. F., Middleton, K. J., Kopelen, H. A., Zoghbi, W. A., & Quiñones, M. A. (1997). Doppler tissue imaging: a noninvasive technique for evaluation of left ventricular relaxation and estimation of filling pressures. *Journal of the American College of Cardiology*, *30*(6), 1527-1533.

29. Sanderson, J. E. (2007). Heart failure with a normal ejection fraction. *Heart*, *93*(2), 155-158.

30. Poerner, T. C., Goebel, B., Unglaub, P., Sueselbeck, T., Strotmann, J. M., Pfleger, S., ... & Haase, K. K. (2003). Detection of a pseudonormal mitral inflow pattern: an echocardiographic and tissue Doppler study. *Echocardiography*, *20*(4), 345-356.

31. Maurer, M. S., Spevack, D., Burkhoff, D., & Kronzon, I. (2004). Diastolic dysfunction: Can it be diagnosed by Doppler echocardiography?. *Journal of the American College of Cardiology*, *44*(8), 1543-1549.

32. Gharib, M., Rambod, E., Kheradvar, A., Sahn, D. J., & Dabiri, J. O. (2006). Optimal vortex formation as an index of cardiac health. *Proceedings of the National Academy of Sciences*, *103*(16), 6305-6308.

33. Gharib, M., Rambod, E., & Shariff, K. (1998). A universal time scale for vortex ring formation. *Journal of Fluid Mechanics*, *360*, 121-140.

34. Krittian, S., Janoske, U., Oertel, H., & Böhlke, T. (2010). Partitioned fluid–solid coupling for cardiovascular blood flow. *Annals of biomedical engineering*, *38*(4), 1426-1441.

35. Charonko, J. J., Kumar, R., Stewart, K., Little, W. C., & Vlachos, P. P. (2013). Vortices formed on the mitral valve tips aid normal left ventricular filling. *Annals of biomedical engineering*, *41*(5), 1049-1061.

36. Pierrakos, O., & Vlachos, P. P. (2006). The effect of vortex formation on left ventricular filling and mitral valve efficiency. *Journal of biomechanical engineering*, *128*(4), 527-539.

37. Hong, G. R., Pedrizzetti, G., Tonti, G., Li, P., Wei, Z., Kim, J. K., ... & Narula, J. (2008). Characterization and quantification of vortex flow in the human left ventricle by contrast echocardiography using vector particle image velocimetry. *JACC: Cardiovascular Imaging*, *1*(6), 705-717.

38. Shadden, S. C., Dabiri, J. O., & Marsden, J. E. (2006). Lagrangian analysis of fluid transport in empirical vortex ring flows. *Physics of Fluids*, *18*(4), 047105.

39. Lipinski, D., & Mohseni, K. (2010). A ridge tracking algorithm and error estimate for efficient computation of Lagrangian coherent structures. *Chaos: An Interdisciplinary Journal of Nonlinear Science*, *20*(1), 017504.

CHAPTER VI

6. SUMMARY AND CONCLUSION

This work evaluated the vortex ring dynamics within flexible-walled confined domains. In the first section (**Figure 6-1A**), we provided comprehensive research on vortex ring dynamics within semi-spheroidal flexible confinement (which is a simplified geometry of the LV) under different axial confinement and also different inflow profiles. After this fundamental study, we investigated vortex ring properties within the left ventricle by conducting *in vitro* experiments **Figure 6-1B** and **Figure 6-1C**). We hypothesized that vortex ring properties would undergo alteration under left ventricular dysfunction, such as a change in LV cavity geometry or transmitral flow variation. Several studies have been examined vortex ring properties within LV; however, there has not been a fundamental study on vortex ring interaction with flexible-walled confinement. The only recent fundamental study on confined vortex ring was conducted by Stewart et al. (1, 2), which studied the vortex ring dynamics within rigid open-ended radial confinements - the effects of axial confinement and flexibility were overlooked.

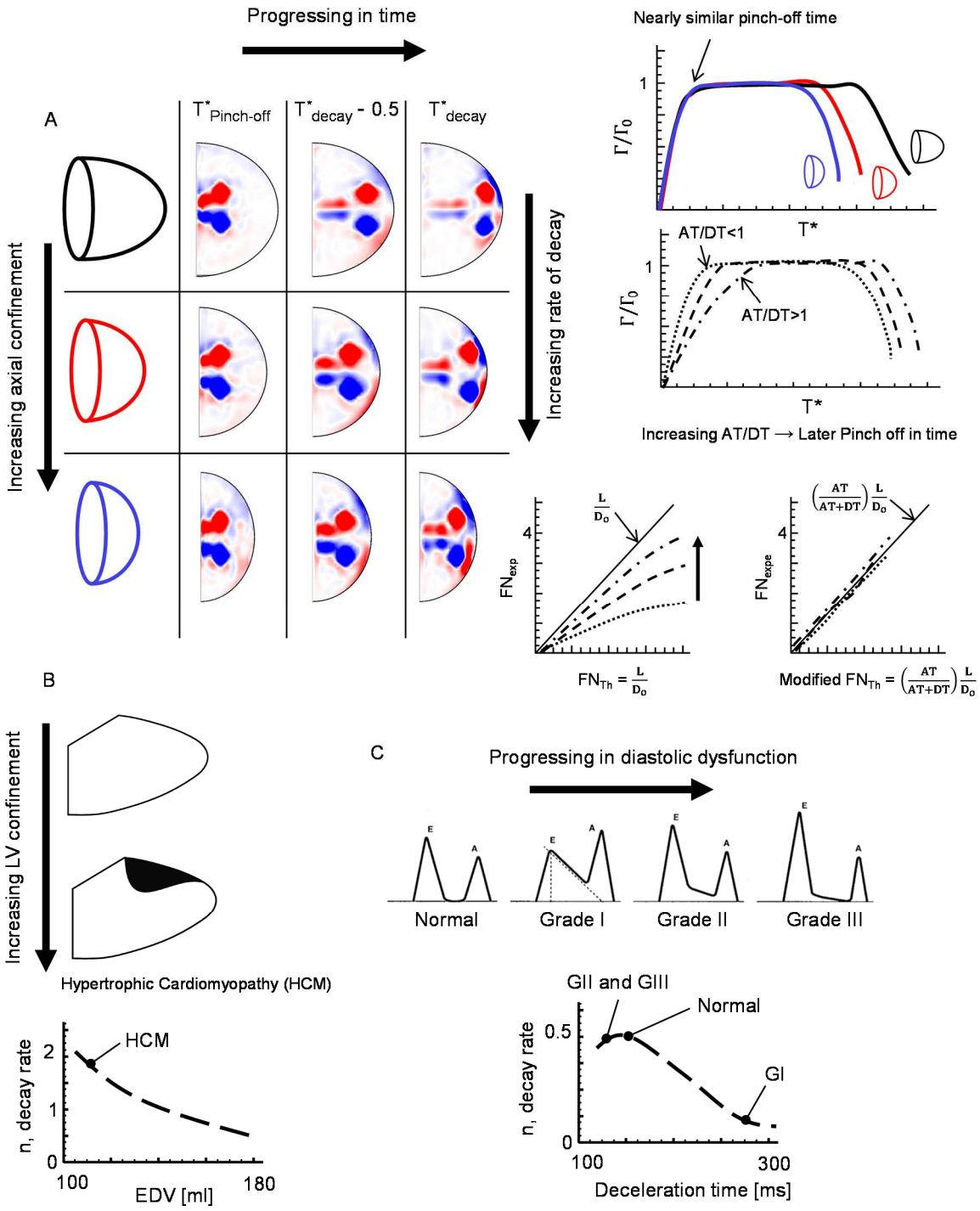

Figure 6-1. Schematic of findings in this study. A) vortex ring dynamics within semi-spheroidal domains. B) Effects of confinement shape on vortex ring behavior. C) Effects of inflow profile in diastolic dysfunction on vortex ring properties

In the first section of this study, we studied vortex ring dynamics within semi-spheroidal flexible-walled confinement, which was the first time to investigate the vortex ring fundamentally within such confinements. Based on the physiological range of E-wave duration, deceleration time, and Reynolds number in the left ventricle, we chose a range of filling time (as an E-wave duration), acceleration to deceleration time ratio (AT/DT), and inflow velocity as an input inflow to the idealized model of the LV (semi-spheroidal). We investigated all inflows in three different aspect ratios of geometries, such that semi-oblate, hemisphere, and semi-prolate. We concluded for a given Re, AT/DT, and filling time, the circulation pinch-off time was unaffected by confinement shape. By increasing axial confinement (i.e., semi-prolate to semi-oblate), we concluded 1) the peak circulation was decreased up to 10%, 2) the circulation decayed earlier, and 3) the circulation rate of decay was faster. By increasing AT/DT (sharper deceleration), the pinch-off vortex ring was delayed. According to Gharib et al. (3), the pinch-off time happens at $T^* = L/D$ (formation number), where L and D are stroke length and piston diameter of the orifice in a cylinder-piston arrangement of vortex generator. Our pinch-off time results for different AT/DT deviated from L/D. Therefore, we introduced a correction factor into the theoretical pinch-off time as $\frac{AT}{AT+DT}$. The modified formation number based on the correction factor, $\left(\frac{AT}{AT+DT}\right)\frac{L}{D}$, was strongly correlated with our results. By increasing Re, the onset of circulation decay was delayed; however, the decay rate was increased. And at the end, by increasing filling time, the peak circulation was increased.

In early diastole (E-wave), the untwisting of the LV muscles results in blood suction into the LV, and the blood flow enters the LV because of active wall movement (active-filling). However, all of the above experiments were conducted under passive-filling, such that the flexible walls were moved because of inflow momentum (passive-filling). Therefore, it was relevant to compare active and passive-filling for at least one of the test conditions. Velocity vector fields, pressure contours, and vortex ring circulation from active-filling showed an insignificant difference

between the two types of filling. The results from this investigation can be used for understanding the vortex ring properties within different shapes of the LV and potentially can lead to diagnostic techniques in cardiology.

Further investigation was conducted on vortex ring dynamics within the left ventricle under diastolic dysfunction conditions. Based on the results from the first part of this study, we designed our tests on *in-vitro* experiments to investigate the role of 1) shape of the LV, and 2) transmitral flow on vortex ring formation and properties within the LV. We examined the fluid flow pattern within a normal LV with three different EDVs and also within an HCM geometry to characterize the effects of LV shape on vortex ring dynamics. Within the high-EDV, the vortex ring broke down later at a time, had a larger diameter, and also had a 20% higher peak circulation value when compared to the low-EDV. The vortex ring onset of decay was earlier in the HCM geometry compared to the normal LV. Also, the pinch-off time remained unaffected by changing the geometry from normal LV to HCM geometry. After understanding the effects of LV geometry on vortex ring properties, we investigated the role of transmitral flow on vortex ring dynamics. Transmitral flows correspond to the normal case along with three grades of diastolic dysfunction were examined in an *in vitro* left heart simulator. Results showed that the normal inflow compared to the diastolic dysfunction inflows generates a more robust vortex ring, which had the highest penetration toward the apex. The results from this study enrich our fluid mechanical understanding of vortex ring dynamics within the LV in diastolic dysfunction and potentially can be helpful for future heart failure diagnostics.

6.1. Potential applications

Studying the vortex ring mechanism will be useful in other communities besides cardiovascular applications. As an example, a diaphragm pump has a membrane to generate pulsatile flow and

correspondingly forms vortex rings. Therefore, studying the behavior of the vortex ring in confined domains will have broader impact and applications.

6.2. Future work

In this study, we examined the entire field of view of confinement to evaluate vortex ring properties when it interacts with flexible walls. However, for a better understanding of the vortex ring breakdown mechanism, we need to investigate the vorticies on the wall. As a result, a zoomed-in PIV very close to the wall will help investigate the formation of secondary vorticies. Also, this would be helpful to determine any difference between active and passive filling since the source of flow in the passive filling is wall movements.

This work looked at the multiple planes of PIV for each experiment; however, the nature of flow in the LV is three dimensional, and the vortex ring geometry is very complex. As a result, we suggest conducting further investigation on vortex ring behavior using a 3D PIV to get a better understanding of vortex ring behavior.

6.3. References

1. Stewart, K. C., Niebel, C. L., Jung, S., & Vlachos, P. P. (2012). The decay of confined vortex rings. *Experiments in Fluids*, *53*(1), 163-171.

2. Stewart, K. C., & Vlachos, P. P. (2012). Vortex rings in radially confined domains. *Experiments in fluids*, *53*(4), 1033-1044.

3. Gharib, M., Rambod, E., & Shariff, K. (1998). A universal time scale for vortex ring formation. *Journal of Fluid Mechanics*, *360*, 121-140.

VITA

MILAD SAMAEE

Candidate for the Degree of

Doctor of philosophy

Dissertation: VORTEX RING PROPAGATION IN CONFINED SPHEROIDAL DOMAINS
AND APPLICATIONS TO CARDIAC FLOWS

Major Field: MECHANICAL AND AEROSPACE ENGINEERING

Biographical:

Education:

Completed the requirements for the Doctor of Philosophy in Mechanical Engineering at Oklahoma State University, Stillwater, Oklahoma in December 2019.

Completed the requirements for the Master of Science in Biomedical Engineering at Amirkabir University of Technology, Tehran/Iran in 2011.

Completed the requirements for the Bachelor of Science in Mechanical Engineering at Khaje Nasir Toosi University of Technology, Tehran/Iran in 2008.

Experience:

Graduate Teaching/Research Assistant in Mechanical andAerospaceEngineering, Oklahoma State University, Stillwater from 2014 to 2019.

Professional Memberships: American Physical Society (APS)